Spectroscopic Studies of Atmospherically- and Biologically-Relevant Interfaces:

Lipids, Ions, and Interfacial Water Structure

DISSERTATION

Presented in Partial Fulfillment of the Requirements for the Degree Doctor of Philosophy
in the Graduate School of The Ohio State University

By

Ellen M. Adams

Graduate Program in Chemistry

The Ohio State University

2016

Dissertation Committee:

Prof. Heather C. Allen, Advisor

Prof. Dennis Bong

Prof. Sherwin Singer

Prof. Hua Wang

Abstract

Sea spray aerosols (SSA) impact Earth's climate directly and indirectly by scattering and absorbing solar radiation and influencing cloud formation, respectively. SSA are formed through the wind-drive wave action at the ocean surface, and their chemical composition is impacted by the biological activity in the sea surface microlayer (SSML), the thin organic layer present at the air-ocean interface. Physical and optical properties of SSA are influenced by the structure and organization of their surfaces. Organic films are known to form at the surface of SSA, and therefore a molecular-level understanding of the organic species that make up these films and their subsequent impact on interfacial properties is necessary to gain insight into climate change.

In this dissertation Langmuir monolayers are utilized as proxies for organic-coated SSA. Phase behavior, rigidity, and stability of monolayers are assessed with surface pressure-area isotherms. Surface morphology of monolayers was imaged with Brewster angle microscopy (BAM). Infrared reflection-absorption spectroscopy (IRRAS) and vibrational sum frequency generation (VSFG) spectroscopy were used to examine the molecular-level structure and intermolecular interactions of the monolayers. VSFG was additionally used to probe the organization and structure of water molecules in the interfacial region. As SSA are chemically complex, several different types of atmospherically-relevant lipid-aqueous interfaces are investigated.

The effect of ion enrichment for marine-relevant cations (Na^+, Mg^{2+}, Ca^{2+}, and K^+) on the interfacial properties of the phospholipid dipalmitoylphosphatidylcholine (DPPC) was investigated. All cations were found to impact monolayer properties, with divalent cations having a greater effect than monovalent ions. Refractive index of the monolayer was found to decrease with increasing cation concentration. In the case of Ca^{2+}, significant dehydration of the phosphate headgroup was observed. Binding affinity followed the trend $Ca^{2+} > Mg^{2+} > Na^+ \approx K^+$.

Investigation of cation enrichment was extended to concentrated solutions of Zn^{2+} and Sr^{2+}. Sr^{2+} was found to have weak interactions with the DPPC monolayer, and impacted properties of the monolayer in a manner similar to a monovalent ion. In contrast, Zn^{2+} interacted strongly with the monolayer, and altered the phase behavior and surface morphology. Increased hydration of the phosphate headgroup was observed with increasing Zn^{2+} concentration. Probing of the interfacial water structure near the monolayer revealed that the hydrogen-bonding network was significantly perturbed by Zn^{2+}. Water molecules preferentially solvate the PC-Zn^{2+} complex, leading to a reduced hydrogen-bonding network. Sr^{2+} also impacted the hydrogen-bonding network through charge screening effects, but to a lesser extent than Zn^{2+}.

The impact of carbohydrates and glycolipids on the organization of interfacial water molecules was also investigated. Glucose was found to have a concentration-dependent influence on the hydrogen-bonding network. The soluble glycolipid lipopolysaccharide

(LPS) was found to impact the hydrogen-bonding network similar to glucose, and had a much greater effect than the insoluble lipids cerebroside and ceramide.

The effect of pH on a palmitic acid (PA) monolayer was studied as well. When PA molecules became deprotonated in the high pH regime, dissolution of lipid molecules into bulk solution occurred. Addition of NaCl to the bulk solution increased the surface propensity of PA molecules, but restoration of a full monolayer did not occur. Probing of interfacial water structure revealed that the hydrogen-bonding network near the monolayer was not perturbed until the majority of the monolayer was deprotonated.

The impact of lipid composition within the monolayer on interfacial properties was probed through the investigation of stratum corneum lipids extracted from four different lark species. Results revealed that phase behavior, surface morphology, and conformation of alkyl chains depended upon the relative abundance of lipid classes in the monolayer. Interfacial water structure was correlated to surface morphology of the monolayer, where a porous morphology lead to an increased population of less coordinated water molecules.

The studies conducted in this dissertation show that interfacial properties of organic-coated SSA are impacted by complexation of lipids with ions, solubility of the lipid, pH, and chemical composition of the organic species. As SSA are complex systems, all of these factors must be considered in attempting to predict their effects on climate change.

Acknowledgments

First and foremost, I would like to acknowledge my advisor Prof. Heather C. Allen for her support and mentorship over the course of my time here. Her passion and excitement for research is evident, and has allowed me to participate in many collaborations in which I have learned a great deal from. I would also like to thank all the Allen group members past and present, particularly Dr. Dana-Marie Telesford, Clayton Casper, Bethany Wellen, and Andrew Vidalis for all their help, support, and stimulating conversations. I would especially like to thank Dr. Dominique Verreault for his assistance in building the BBSFG setups, and for his support and friendship inside and outside of the lab. Lastly, I would like to thank my family for their continued support.

Vita

2010	B. S. Chemistry, Lebanon Valley College
2013	M.S. Chemistry, The Ohio State University
2010-2015	Graduate Teaching Associate, Department of Chemistry & Biochemistry, The Ohio State University
2015-present	Graduate Research Associate, Department of Chemistry & Biochemistry, The Ohio State University

Publications

- E.M. Adams, D. Verreault, T. Jayarathne, R.E. Cochran, E.A. Stone, H.C. Allen; Surface Organization of a DPPC Monolayer on Concentrated $SrCl_2$ and $ZnCl_2$ Solutions, *Phys. Chem. Chem. Phys*. **2016**, 18, 32345-32357
- E.M. Adams, C.B. Casper, H.C. Allen; Effect of Cation Enrichment on Dipalmitoylphosphatidylcholine (DPPC) Monolayers at the Air-Water Interface, *J. Colloid Interface Sci.,* **2016**, 478, 353-364

- C.B. Casper, D. Verreault, E.M. Adams, W. Hua, H.C. Allen; Surface Potential of DPPC Monolayers on Concentrated Aqueous Salt Solutions, *J. Phys. Chem. B*, **2016**, 120(8), 2043-2052
- E.C. Griffith, R.J. Perkins, D.-M. Telesford, E.M. Adams, L. Cwiklik, H.C. Allen, M. Roeselová, V. Vaida; Interaction of L-Phenylalanine with a Phospholipid Monolayer at the Water-Air Interface, *J. Phys. Chem. B*, **2015**, 119(29), 9038-9048
- W. Hua, D. Verreault, Z. Huang, E.M. Adams, H.C. Allen; Cation Effects on Interfacial Water Organization of Aqueous Chloride Solutions. I. Monovalent Cations: Li^+, Na^+, K^+, and NH_4^+, *J. Phys. Chem B*, **2014**, 118(28), 8433-8440
- E.M. Adams, H.C. Allen; Palmitic Acid on Salt Subphases and in Mixed Monolayers of Cerebrosides: Application to Atmospheric Aerosol Chemistry, *Atmosphere*, **2013**, 4(4), 315-336
- W. Hua, D. Verreault, E.M. Adams, Z. Huang, H.C. Allen; Impact of Salt Purity on Interfacial Water Organization Revealed by Conventional and Heterodyne-Detected Vibrational Sum Frequency Generation Spectroscopy, *J. Phys. Chem. C,* **2013**, 117(38), 19577-19585
- E.C. Griffith, E.M. Adams, H.C. Allen, V. Vaida; Hydrophobic Collapse of a Stearic Acid Film by Adsorbed L-Phenylalanine at the Air-Water Interface, *J. Phys. Chem. B*, **2012**, 116(27), 7849-7857

Fields of Study

Major Field: Chemistry

Table of Contents

List of Tables

List of Figures

Chapter 1: Introduction

1.1. Motivation.

This dissertation encompasses studies of atmospherically- and biologically-relevant interfaces. The motivation of these studies is to gain insight into the interfacial structure of lipid films and water at the surface of sea spray aerosols (SSA), and includes investigation of lipid complexation with ions, glycolipids at the air-water interface, the influence of pH on a fatty acid film, and the impact of lipid composition on film properties.

Of all the factors that contribute to climate change, atmospheric aerosols have the largest uncertainty in their radiative forcing.[1] Aerosols influence radiative forcing directly by absorbing and scattering solar radiation and indirectly by altering cloud condensation and ice nucleation processes.[2] Production of aerosols comes from a variety of sources, including biomass burning, volcanic eruptions, and anthropogenic processes.[3] One of the largest sources of naturally produced aerosols is the ocean, which covers approximately 70% of the Earth's surface. SSA are produced from breaking waves and wind shearing at the ocean surface. Ellison was the first to propose that SSA have an inverted micelle structure, in which an aqueous sea salt core is surrounded by a thin organic coating.[4]

Experiments later confirmed this theory, revealing that fatty acids are one of the main components making up the organic layer.[5,6] More recent studies have found that a variety of particle morphologies exist and are correlated to the respective size range of the particle.[7]

Physical and optical properties of aerosols are related to the structure of the particle surface.[8] Growth, hygroscopicity, chemical reactivity, and the ability to scatter light and act as cloud condensation or ice nuclei are all properties and processes influenced by the presence of surface active organic species.[9–15] A molecular-level understanding of the organization of organic species at the surface of aerosols and how they impact interfacial structure is therefore necessary to predict effects on aerosol properties.

Chemical composition of SSA is reflective of the sea surface microlayer (SSML),[16] the chemically distinct layer (~500 μm) at the ocean surface, and depends on its biological activity.[17] Organic species identified in the SSML include amino acids, phospholipids, fatty acids, sterols, carbohydrates, and glycolipids.[8,18–20] Although speciation (organic and inorganic) of seawater and SSML has been investigated extensively, their interfacial structure and properties are still poorly understood.

Several studies have been dedicated to understanding the effect of biological cycles on the chemical composition of SSA.[7,21–25,20] Four distinct particle types were identified from these studies: organic-carbon (OC), sea salt-organic carbon (SSOC), biological (Bio), and sea salt (SS).[7,21,26] The fraction of total organic content (TOC) in these particles was associated with particle size, where TOC decreased with increasing size.[23] Therefore, OC and Bio particles are typically smaller in size (≤ 1μm), while SS and

SSOC particles are larger in size (≥ 1μm). The organization of surface-active organic species is likely different in these size regimes, especially as complexation of lipid species to inorganic ions is known to impact interfacial properties.[27–30]

Of the inorganic ions founds in seawater, sodium (Na^+), magnesium (Mg^{2+}), potassium (K^+), and calcium (Ca^{2+}) are the most abundant.[31] Enrichment (relative to the amount of Na^+) of Mg^{2+}, K^+, and Ca^{2+} has been observed in the SSML and SSA.[20,25] Furthermore, elemental mapping studies have shown that these ions are enriched at the interface of SSA.[7,32]. Enrichment of ions in SSA appears to be dependent on the ability of ions to complex to lipid molecules, as some ions, such as strontium (Sr^{2+}) are depleted in SSA compared to bulk seawater.[33] Transition metals, such as zinc (Zn^{2+}), have also been found to be enriched in SSA, and in some cases are significantly more enriched in SSA compared to alkali or alkaline earth cations.[33–35] An understanding of the binding affinities of these various ions to lipid molecules may provide insight into why selective transfer of ions occurs in SSA. Additionally, as enrichment of ions leads to increased salinity, especially in the case where particle drying has occurred, interfacial properties of lipid molecules are likely altered. Investigation of interfacial properties of lipids as a function of ion concentration could shed light on the surface structure of SSA, especially in the case of aqueous phase particles in the high salinity regime.

Enrichment of carbohydrates (relative to Na^+) has also been observed in SSA.[20] Carbohydrates have been found in both the soluble and insoluble fractions of SSA,[18,36] which suggests that they can exist as free monomers (glucose, for example) or as part of a complex glycolipid such as lipopolysaccharides (LPS). The hygroscopicity of model SSA is impacted by the mixing state of carbohydrates, which implies surface structure may be different depending on the relative amount of carbohydrate.[37] An understanding of interfacial water structure for soluble saccharides and glycolipids, as well as insoluble glycolipids may provide insight on hygroscopicity of aerosols.

In addition to chemical speciation, pH of SSA has been shown to change with particle size. Smaller sized SSA have been found to be more acidic in their nature, while larger ones are basic.[38,39] Chemical reactivity and uptake of gases has been demonstrated to be different for aerosols in these two size regimes,[32,39] which indicates that their surface structure is impacted by pH. Investigation of a lipid common to both size ranges may reveal how the interfacial structure of SSA changes with pH.

Studies in this dissertation are also motivated by biomembranes and biological interfaces. Biomembranes are bilayers of lipid sheets that are mostly composed of phospholipids.[40] In some specialized membranes, such as myelin sheaths, sphingolipids and glycosphingolipids are abundant as well.[41] Binding of metal cations to phospholipids has been shown to promote fusion of lipid vesicles or disrupt lipid packing depending on the identity of the cation.[42,43] Therefore, it is important to understand the impact that metal cations, as well as their relative concentration, have on the interfacial properties of phospholipids.

While not a biomembrane, the stratum corneum, which is the outermost layer of skin, is one of the largest biological interfaces in the body. This layer is composed of dead cells embedded in a lipid matrix.[44] These intercellular lipids control evaporative water loss as well as permeation of pathogens through skin. Furthermore, cutaneous water loss (CWL) in birds has been linked to the chemical composition of lipids in the stratum corneum.[45–47] To understand CWL rates in birds, knowledge of the structure and organization of SC lipids is needed. In addition, the structure of interfacial water molecules near the SC monolayer may provide insight into CWL.

1.2. Dissertation Highlights.

Chapter 2 provides the basic theory necessary for the application of the surface-sensitive imaging and spectroscopic techniques such as Brewster angle microscopy (BAM), infrared reflection-absorption spectroscopy (IRRAS), and vibrational sum frequency generation (VSFG) spectroscopy. Instrumental setups are described as well.

Chapter 3 reports on the impact of concentrated NaCl, KCl, $MgCl_2$, and $CaCl_2$ aqueous solutions on the interfacial properties of a dipalmitoylphosphatidylcholine (DPPC) monolayer. Packing density and phase behavior of DPPC molecules were influenced by cation identity and concentration. Divalent cations were found to have a greater effect than monovalent ions. Surface morphology and refractive index of the monolayer were altered, especially when cations were highly concentrated. Conformation of the lipid alkyl chains and hydration of the PC headgroup were also impacted by cation identity and concentration.

Chapters 4 and 5 discuss the interfacial properties of a DPPC monolayer on concentrated aqueous solutions of $SrCl_2$ and $ZnCl_2$. Properties of the monolayer were not significantly impacted by Sr^{2+}, which weakly interacted with the PC headgroup. Zn^{2+} ions strongly interacted with the lipid molecules, and altered interfacial properties, including phase behavior, surface morphology, and alkyl chain conformation. Interfacial water structure was also significantly impacted by Zn^{2+} ions, where available water molecules preferentially solvated the PC-Zn^{2+} complex instead of hydrogen-bonding with other water molecules. Sr^{2+} ions also impacted water structure, but to a lesser extent.

Chapter 6 details the conformational organization of soluble and insoluble glycolipids as well as the interfacial water organization. Glycolipids were found to form films with significant gauche defects, regardless of solubility. Interfacial water organization was impacted differently by the presence of soluble and insoluble species. Bulk concentration of the glucose was found to have opposite effects (increased disorder vs. order) on water molecules in the low and high concentration regimes.

Chapter 7 details the impact pH has on the surface properties of a palmitic acid (PA) monolayer. Dissolution of PA molecules into bulk solution was found to occur upon deprotonation of the carboxylic acid. Addition of NaCl to the solution increased surface propensity of ionized PA molecules. Probing of interfacial water structure found that pH did not impact water structure until deprotonation of the monolayer occurred.

Chapter 8 discusses and compares the interfacial properties of lipids extracted from the stratum corneum of desert and mesic lark species. Lipid composition was found to impact the phase behavior, surface morphology, and alkyl chain conformation of the film. Interfacial water structure was linked to surface morphology, where porous films lead to water molecules having a more disordered hydrogen-bonding network. Finally, Chapter 9 highlights the implications of these findings on atmospheric and biological interfaces.

Chapter 2: Theoretical Background and Instrumentation

In this chapter an overview of the theory of Brewster angle microscopy (BAM), infrared reflection-adsorption spectroscopy (IRRAS), and vibrational sum frequency generation (VSFG) spectroscopy is presented. Instrumental and experimental details are provided as well. Experimental details pertaining to each experiment are provided in particular chapters.

2.1. Theoretical Background

2.1.1 Brewster angle Microscopy

BAM is a microscopy technique used to determine the surface morphology and optical properties of insoluble Langmuir films at the air-aqueous interface. Principles of BAM have been discussed in detail elsewhere,[48–50] and hence will be briefly reviewed here.

The air-aqueous interface forms a boundary between these two optically distinct bulk media, i.e. with different refractive indices. For an incident light beam, the reflectance (R) from the interface is defined as the fraction of reflected intensity (I_R) relative to the incident intensity (I_0).

$$R = \frac{I_R}{I_0} \tag{2.1}$$

The reflectance can be calculated by multiplying the complex Fresnel reflection coefficient (r) with its complex conjugate.

$$R = |\tilde{r}|^2 = \tilde{r}\tilde{r}^* \tag{2.2}$$

Reflectance is dependent upon the wavelength (λ), incident angle (θ_i) and polarization state (p- or s-polarized) of the incoming beam, as well as the refractive indices of the optical media (n).[51,52] p-polarized and s-polarized refer to light in which the electric field oscillates parallel and perpendicular to the plane of incidence, respectively. The reflectances for p-polarized (R_p) and s-polarized (R_s) light can be determined from the Fresnel equations.

$$R_p = \left(-\frac{\tan(\theta_i - \theta_r)}{\tan(\theta_i + \theta_r)}\right)^2 \tag{2.3}$$

$$R_s = \left(-\frac{\sin(\theta_i - \theta_r)}{\sin(\theta_i + \theta_r)}\right)^2 \tag{2.4}$$

When p-polarized light impinges on the air-aqueous interface at the Brewster angle (θ_B), no light is reflected from the interface. This occurs because the dipole moment induced by the electric field is parallel to the reflected direction, and since dipoles do not radiate energy in the direction of the dipole moment, no reflection is observed. The Brewster angle is determined from the refractive indices of air (n_a) and the aqueous solution (n_s).

$$\theta_B = tan^{-1}\left(\frac{n_s}{n_a}\right) \tag{2.5}$$

For the air-water interface the Brewster angle is ~53.1°. When a Langmuir monolayer is present at the surface of the aqueous solution, the refractive index of the interface is altered (Figure 2.1). Reflectance of p-polarized light from the monolayer occurs as a consequence, and the reflected light can be collected to form an image of the interface. Images produced from BAM are based on the contrast of reflectance from the aqueous solution and the monolayer-covered surface. Regions that are solution-rich or lipid-poor will appear as black, while lipid-rich regions will be bright.

Ideally, R_p from the interface vanishes at the Brewster angle, but for a real interface R_p has a minimal but non-zero value. Properties of the interfacial region, mainly thickness, roughness, and optical anisotropy, are credited as the origin of this discrepancy.[48,50,53] For a real interface, the observed reflectance at the Brewster angle (R_p^0) has contributions from both R_p and R_s, and also depends on as the ellipticity (ρ) of the interface (Eq. 2.6). Ellipticity can be determined from ellipsometry, for which a detailed description can be found elsewhere.[54,55]

$$R_p^0 = R_p + R_s\rho^2 \tag{2.6}$$

In the case of a homogeneously thick interface, i.e. a monolayer-covered surface, the ellipticity is proportional to the monolayer thickness (d) and the refractive index of the monolayer (n_m):

$$\rho = \frac{\pi d}{\lambda}\frac{\sqrt{n_a^2 + n_s^2}}{n_a^2 - n_s^2}\frac{(n_a^2 - n_m^2)(n_s^2 - n_m^2)}{n_m^2} \tag{2.7}$$

As $R_p << R_s$ at the Brewster angle, Eq. (2.6) reduces to Eq. (2.8).

$$R_p^0 = \left[\pi \sin\left(2\theta_B - 90\right)\frac{d}{\lambda}\frac{\sqrt{n_a^2 + n_s^2}}{n_a^2 - n_s^2}\frac{(n_a^2 - n_m^2)(n_s^2 - n_m^2)}{n_m^2}\right]^2 \tag{2.8}$$

BAM can be used to determine quantitative properties of the monolayer film, i.e., thickness or monolayer refractive index, if the relative reflectance from the interface is known.

2.1.2. Infrared Reflection-Absorption Spectroscopy

IRRAS is a spectroscopic technique used to determine the molecular orientation of Langmuir films. Additionally, information about the degree of dissociation of the polar headgroups and binding/interaction of ions or organic molecules in solution to the lipid monolayer can be obtained.

Spectra obtained from IRRAS are presented as reflectance-absorbance (*RA*) spectra. RA is determined from the logarithmic ratio of the reflectance of the monolayer-covered surface (R_m) relative to the reflectance of the bare aqueous solution (R_0).

$$RA = -\log\left(\frac{R_m}{R_0}\right) \tag{2.9}$$

The Fresnel reflection coefficients of a thin, anisotropic monolayer at an interface can be expressed as follows for *s*- and *p*-polarizations[56–58]

$$\tilde{r}_s = -\frac{\left[\sin(\theta_i - \theta_r) - \frac{2i\pi}{\lambda\tilde{n}_s} sin\theta_i \tilde{I}_1\right]}{\left[\sin(\theta_i + \theta_r) - \frac{2i\pi}{\lambda\tilde{n}_s} sin\theta_i \tilde{I}_1\right]} \tag{2.10}$$

$$\tilde{r}_p = \frac{\left[\sin(\theta_i - \theta_r)cos(\theta_i + \theta_r) - \frac{2i\pi}{\lambda\tilde{n}_s} sin\theta_i(\tilde{I}_1 cos\theta_i cos\theta_r - \tilde{I}_2 sin\theta_i sin\theta_r)\right]}{\left[\sin(\theta_i + \theta_r)cos(\theta_i - \theta_r) - \frac{2i\pi}{\lambda\tilde{n}_s} sin\theta_i(\tilde{I}_1 cos\theta_i cos\theta_r + \tilde{I}_2 sin\theta_i sin\theta_r)\right]} \tag{2.11}$$

where

$$\tilde{I}_1 = \left(\tilde{n}_{m,x}{}^2 - \tilde{n}_s{}^2\right)d \tag{2.12}$$

$$\tilde{I}_2 = \frac{\left(\tilde{n}_{m,z}{}^2 - \tilde{n}_s{}^2\right)d}{\tilde{n}_{m,z}{}^2} \tag{2.13}$$

and where $\tilde{n}_s$ refers to the refractive index of the aqueous solution, and $\tilde{n}_{m,x}$ and $\tilde{n}_{m,z}$ are the complex refractive indices of the anisotropic monolayer, with the x- and z-directions defined parallel and perpendicular to the interface plane.

Based on the Fresnel coefficients, absorption bands observed in IRRAS can be positive or negative, depending on the polarization state and incident angle of the incoming beam. For s-polarized light, RA will be negative for all incident angles. In the case of p-polarized light, RA is negative for incident angles below the Brewster angle, but becomes positive at angles larger than the Brewster angle. A more detailed account on the intensity and sign of IRRAS bands, and their angular dependence can be found in literature.[56] In the case of unpolarized light, as was used in this dissertation, only negative absorption features will be considered.

2.1.3. Vibrational Sum Frequency Generation Spectroscopy

VSFG is a second-order nonlinear spectroscopy technique that provides a vibrational spectrum of the interface. Being second-order, sum frequency generation (SFG) is forbidden in media containing centrosymmetry like bulk phases. At an interface, however, symmetry is broken, and SFG can occur. A detailed description of SFG theory can be found elsewhere,[59–62] therefore only a brief review will be given here.

Experimentally VSFG spectroscopy uses two intense pulsed lasers, one of which is fixed at a visible frequency (ω_{VIS}) and the other is tunable over the IR region (ω_{IR}), are overlapped temporally and spatially to produce photons with a frequency that is the sum of those of the two input beams ($\omega_{SFG} = \omega_{VIS} + \omega_{IR}$). VSFG can be described as a coherent anti-Stokes process in which simultaneous anti-Stokes scattering occurs from an infrared excited vibrational state (Figure 2.2).

The intensity of the SFG signal (I_{SFG}), as can be seen in Eq. (2.14), is proportional to the intensity of the incident visible (I_{VIS}) and IR (I_{IR}) beams and the absolute square of the effective second-order nonlinear susceptibility ($\chi_{eff}^{(2)}$).

$$I_{\mathrm{SFG}} \propto \left|\chi_{\mathrm{eff}}^{(2)}\right|^2 I_{\mathrm{VIS}} I_{\mathrm{IR}} \tag{2.14}$$

In general, $\chi_{eff}^{(2)}$ contains both non-resonant ($\chi_{NR}^{(2)}$) (electronic transitions) and resonant ($\chi_{R}^{(2)}$) (vibrations) contributions (Eq. (2.15)). In the case of dielectric materials, $\chi_{NR}^{(2)}$ is typically small and the majority of the SFG intensity comes from the resonant term.

$$\chi_{\mathrm{eff}}^{(2)} = \chi_{NR}^{(2)} + \sum_q \chi_q^{(2)} \tag{2.15}$$

Resonant enhancement of SFG occurs when the IR frequency matches that of the q-th vibrational mode (ω_q). In other words, when $\omega_{IR} - \omega_q \approx 0$, $\chi_q^{(2)}$ becomes large, resulting in an increase in SFG intensity, as can be seen in Eq. (2.16)

$$\sum_q \chi_q^{(2)} = \sum_q \frac{A_q e^{-i\Delta\varphi_q}}{\omega_{\mathrm{IR}} - \omega_q + i\Gamma_q} \tag{2.16}$$

where A_q and Γ_q are the SFG transition moment and line width (half width at half maximum) of the q-th vibrational mode, and $\Delta\varphi_q$ is the phase difference between the resonant and non-resonant terms. As ω_q is off-resonant with the visible frequency, $\Delta\varphi_q$ can be assumed to be equivalent to zero. The SFG transition moment has contributions from the Raman polarizability tensor and the IR transition moment. As a result, the vibrational mode must be Raman- and IR-active to have an SFG response.

As a third-rank tensor, $\chi^{(2)}$ has 27 components in a laboratory coordinate system, which can be expressed as $\chi_{ijk}^{(2)}$ (in which subscripts i, j, and k can take any of the coordinate x, y, or z). $\chi_{ijk}^{(2)}$ (Eq. (2.17)) is a macroscopic property and is related to the microscopic molecular hyperpolarizability ($\beta_{\alpha\beta\gamma}$) by the surface number density of molecular groups (N_s) and the Euler angle transformation ($\langle T_{ijk:\alpha\beta\gamma} \rangle$) between molecular ($\alpha\beta\gamma$) and laboratory coordinates (ijk), where $\langle \ldots \rangle$ denotes the ensemble average over all possible molecular orientations.

$$\chi_{ijk}^{(2)} = N_s \sum_{\alpha\beta\gamma} \langle T_{ijk:\alpha\beta\gamma} \rangle \, \beta_{\alpha\beta\gamma} \tag{2.17}$$

The experimentally measured SFG intensity is dependent upon the polarization combination and experimental geometry. The four most commonly used experimental polarization combinations are *ssp*, *sps*, *pss*, and *ppp*. For a surface that is rotationally isotropic, the number of $\chi_{ijk}^{(2)}$ elements that are non-zero reduces to seven. The $\chi_{eff}^{(2)}$ for each polarization combination in a co-propagating geometry can be written in terms of the non-zero $\chi_{ijk}^{(2)}$ elements[62]

$$\chi_{\mathrm{eff},ssp}^{(2)} = L_{yy}(\omega_{\mathrm{SFG}}) L_{yy}(\omega_{\mathrm{VIS}}) L_{zz}(\omega_{\mathrm{IR}}) \sin\theta_{\mathrm{IR}} \, \chi_{yyz}^{(2)} \tag{2.18}$$

$$\chi_{\mathrm{eff},sps}^{(2)} = L_{yy}(\omega_{\mathrm{SFG}}) L_{yy}(\omega_{\mathrm{VIS}}) L_{yy}(\omega_{\mathrm{IR}}) \sin\theta_{\mathrm{VIS}} \, \chi_{yzy}^{(2)} \tag{2.19}$$

$$\chi_{\mathrm{eff},pss}^{(2)} = L_{zz}(\omega_{\mathrm{SFG}}) L_{yy}(\omega_{\mathrm{VIS}}) L_{yy}(\omega_{\mathrm{IR}}) \sin\theta_{\mathrm{SFG}} \, \chi_{zyy}^{(2)} \tag{2.20}$$

$$\begin{aligned}&\chi^{(2)}_{\mathrm{eff},ppp}\\&= -L_{xx}(\omega_{\mathrm{SFG}})L_{xx}(\omega_{\mathrm{VIS}})L_{zz}(\omega_{\mathrm{IR}})\cos\theta_{\mathrm{SFG}}\cos\theta_{\mathrm{VIS}}\sin\theta_{\mathrm{IR}}\,\chi^{(2)}_{xxz}\\&- L_{xx}(\omega_{\mathrm{SFG}})L_{zz}(\omega_{\mathrm{VIS}})L_{xx}(\omega_{\mathrm{IR}})\cos\theta_{\mathrm{SFG}}\sin\theta_{\mathrm{VIS}}\cos\theta_{\mathrm{IR}}\,\chi^{(2)}_{xzx}\\&+ L_{zz}(\omega_{\mathrm{SFG}})L_{xx}(\omega_{\mathrm{VIS}})L_{xx}(\omega_{\mathrm{IR}})\sin\theta_{\mathrm{SFG}}\cos\theta_{\mathrm{VIS}}\cos\theta_{\mathrm{IR}}\,\chi^{(2)}_{zxx}\\&+ L_{zz}(\omega_{\mathrm{SFG}})L_{zz}(\omega_{\mathrm{VIS}})L_{zz}(\omega_{\mathrm{IR}})\sin\theta_{\mathrm{SFG}}\sin\theta_{\mathrm{VIS}}\sin\theta_{\mathrm{IR}}\,\chi^{(2)}_{zzz}\end{aligned} \tag{2.21}$$

In Eq. (2.18)-(2.21), L_{ii} are the nonlinear Fresnel factors at frequency ω_i, and θ_i is the angle of incoming (θ_{IR}, θ_{VIS}) or outgoing beam (θ_{SFG}) with respect to the surface normal. Expressions for L_{ii} can be found in literature.[61,62]

The measured $\chi_{eff}^{(2)}$ is related to the orientation of the molecular group (θ) through the $\chi_{ijk}^{(2)}$ elements. Molecular symmetry of the group must be considered, as this determines the non-zero $\chi_{ijk}^{(2)}$ elements. In this dissertation, the orientation of methyl (CH_3) groups is investigated, which have a C_{3v} symmetry group. In the case of a C_{3v} symmetry group, there are seven non-vanishing $\chi_{ijk}^{(2)}$ terms, assuming that the surface is rotationally isotropic. For the symmetric stretching vibrational modes, $\chi_{ijk}^{(2)}$ are expressed as

$$\chi^{(2),ss}_{xxz} = \chi^{(2),ss}_{yyz} = \frac{1}{2}N_s\beta_{ccc}[(1+R)\langle\cos\theta\rangle - (1-R)\langle\cos^3\theta\rangle] \tag{2.22}$$

$$\chi^{(2),ss}_{xzx} = \chi^{(2),ss}_{zxx} = \chi^{(2),ss}_{yzy} = \chi^{(2),ss}_{zyy} = \frac{1}{2}N_s\beta_{ccc}(1-R)[\langle\cos\theta\rangle - \langle\cos^3\theta\rangle] \tag{2.23}$$

$$\chi^{(2),ss}_{zzz} = N_s\beta_{ccc}[R\langle\cos\theta\rangle + (1-R)\langle\cos^3\theta\rangle] \tag{2.24}$$

In the case of asymmetric stretching vibrational modes, $\chi_{ijk}^{(2)}$ are given by

$$\chi^{(2),as}_{yyz} = \chi^{(2),as}_{xxz} = -N_s\beta_{aca}(\langle\cos\theta\rangle - \langle\cos^3\theta\rangle) \tag{2.25}$$

$$\chi_{xzx}^{(2),as} = \chi_{zxx}^{(2),as} = \chi_{yzy}^{(2),as} = \chi_{zyy}^{(2),as} = N_s \beta_{aca} \langle \cos^3 \theta \rangle \tag{2.26}$$

$$\chi_{zzz}^{(2),as} = 2N_s \beta_{aca} (\langle \cos \theta \rangle - \langle \cos^3 \theta \rangle) \tag{2.27}$$

where R is the hyperpolarizability ratio, defined as $R = \beta_{aac}/\beta_{ccc}$. R can be determined experimentally from the Raman depolarization ratio.[62–64]

2.2 Instrumentation

2.2.1 BAM Setup

BAM images were collected on a custom-built BAM setup that has been previously described.[65–68] Briefly, a 543 nm *p*-polarized laser (Research Electro-Optics) with 5 mW output irradiates the surface (bare or monolayer-covered) at the corresponding Brewster angle for each respective aqueous solution. The incoming beam is attenuated with a half-wave plate (Eskpla) before passing through a Glan prism (Ekspla) to ensure only *p*-polarized light impinges the sample surface. The reflected light is collected and collimated with a super-long working distance 10× objective and a tube lens (Nikon) before being imaged with an electron-multiplying charge coupled device (EMCCD) camera (Andor, model DV887-BV). The CCD is composed of 512 × 512 pixels with each pixel having dimensions of 16 × 16 μm. Total image size is 800 × 800 μm.

2.2.2. IRRAS Setup

IRRAS spectra were collected with a FTIR spectrometer (Perkin Elmer, Spectrum 100) equipped with a HgCdTe (MCT) detector (Figure 2.3). A breadboard was inserted into the spectrometer chamber, on which two planar gold mirrors, each with a 2 inch diameter, were mounted to direct light to and collect light from the sample surface. The incident angle of the IR beam was set to 46° from the surface normal so that only negative absorption features would be considered, as the incident angle is below the Brewster angle.

2.2.3. IR-VIS Broadband Vibrational Sum Frequency Generation Setup

Two different infrared-visible broadband VSFG (BBSFG) setups were utilized in this dissertation.The two setups are similar; the main difference arises in how the visible picosecond (ps) beam was produced (Figures 2.4 and 2.5). Details of both systems are provided below.

In the first BBSFG (BBSFG-1) setup, the sub-100 femtosecond (fs) pulses generated from a Ti:sapphire oscillator (Spectra-Physics, Tsunami, model 3960-X1S) are used to seed a 1 kHz regenerative Ti:sapphire amplifier (Spectra-Physics, Spitfire Ace) to produce ~90 fs pulses centered at 800 nm. A portion of the ~4 W amplified output is sent to an optical parametric amplifier (Light Conversion, TOPAS-C) connected to a non-collinear difference frequency generator (NDFG, Light Conversion) to generate a tunable broadband IR beam (2.4–11 μm). Bandwidth of the IR pulse depends on the spectral region. The remaining portion of the amplified output is passed through an air-spaced (d = 11 μm) Fabry-Pérot etalon (SLS Optics) to produce an asymmetrical ps visible pulse at 800 nm. The etalon has a free spectral range (FSR) of 449.5 cm^{-1}, determined from the relationship $FSR = c/2d$, where c is the speed of light. The effective finesse (F_{eff}) depends on the reflectivity, R, of the two mirrors in the etalon, $F_{eff} = \pi/(1-R)$, and is 38.6 for this etalon. Bandwidth of the ps output pulse is ~12 cm^{-}1, and can be determined from $\Delta v = FSR/ F_{eff}$. As long as the air-gap of the etalon is smaller than the pulse coherence length,

l_c ($l_c = t_p c$, where $t_p = 90$ fs), a ps output pulse will be produced. The visible and IR beams were temporally and spatially overlapped at the sample surface to produce broadband SFG. A co-propagating geometry was used in this setup, where the visible and IR beams had incident angles of 53° and 68° from the surface normal, respectively. The SFG beam in the reflection direction was re-collimated and focused to the slit of the spectrometer (Princeton Instruments, Spectra Pro-500i) and detected by a LN_2-cooled CCD (Princeton Instruments, Spec-10:400B, 1340×400 pixels).

VSFG spectra presented in the CH region (2800-3000 cm^{-1}) in Chapter 6 were collected with the second BBSFG (BBSFG-2) setup, which has previously been described.[69] Two regenerative amplifiers (Spectra-Physics, Spitfire Ace and Spitfire Pro) were seeded by the same sub-100 fs Ti:sapphire oscillator (Spectra-Physics, Tsunami) to produce ~90 fs (Spitfire Ace) and 2 ps pulses (Spitfire Pro), respectively. The ps beam output, which was directly used as the visible source, was centered at 796 nm and had a 17 cm^{-1} bandwidth. The 3 W fs output was sent to the optical parametric amplifier (TOPAS-C, Light Conversion) and NDFG (Light Conversion) to produce a tunable broadband IR beam (2.4–11 μm). The visible and IR beams had incident angles of 54° and 65°, respectively, and a co-propagating geometry was also utilized. Details of the spectrometer and CCD detector are the same as the BBSFG-1 setup.

Regardless of the system that VSFG spectra were collected on, raw data was analyzed in the same manner. Spectra were filtered of cosmic radiation spikes, background-subtracted, and normalized to the non-resonant SFG profile of a GaAs (110) crystal (II-VI Inc.) to eliminate distortion from the IR beam. Peak positions in the VSFG spectra were calibrated by comparison of the non-resonant absorption spectrum of a polystyrene film to those collected with an FTIR spectrometer.

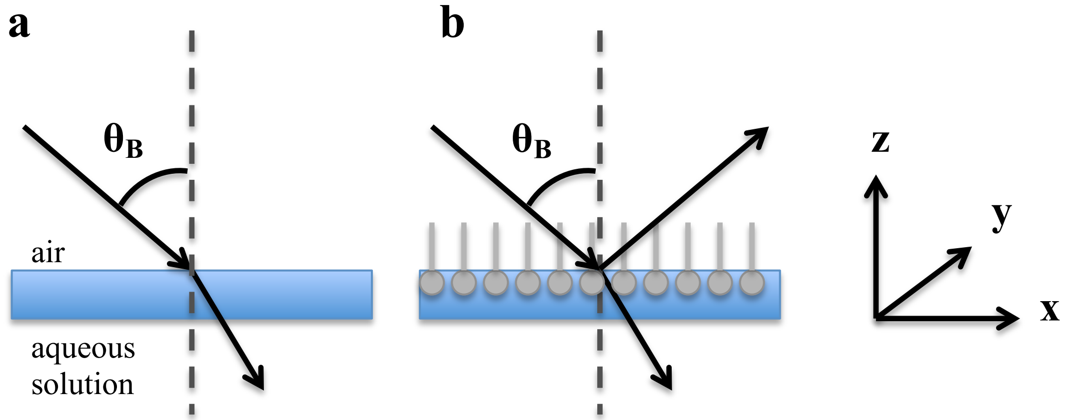

Figure 2.1. Schematic of the principles of BAM. (a) When p-polarized light impinges on the bare air-aqueous interface at the Brewster angle, no light is reflected. (b) The presence of a Langmuir monolayer alters the refractive index of the interface, resulting in reflection of *p*-polarized light. An image of the interface can be obtained from the reflection.

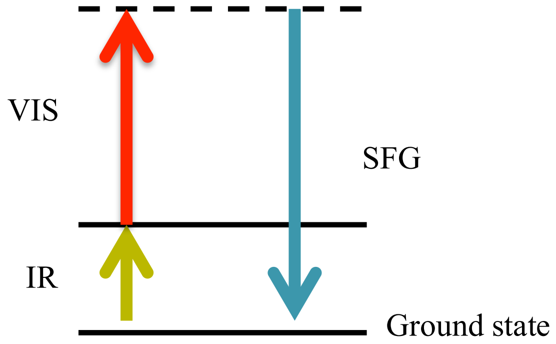

Figure 2.2. Energy level diagram for the SFG process. In a coherent anti-Stokes process an anti-Stokes beam is generated from the interaction of a pump, Stokes, and probe beam. The dashed line indicates a virtual state.

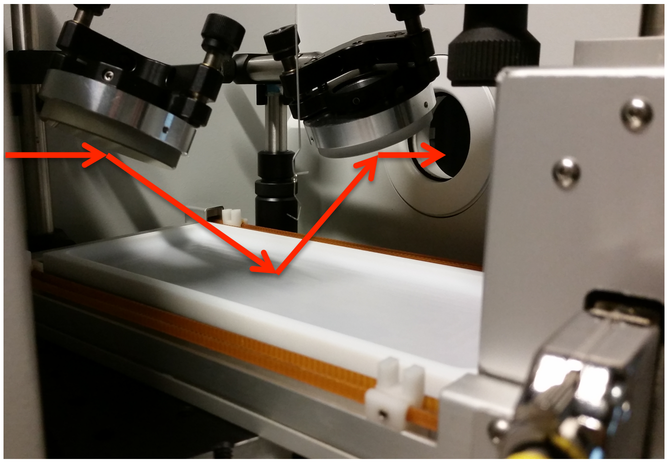

Figure 2.3. IRRAS setup within the chamber of the FTIR spectrometer.

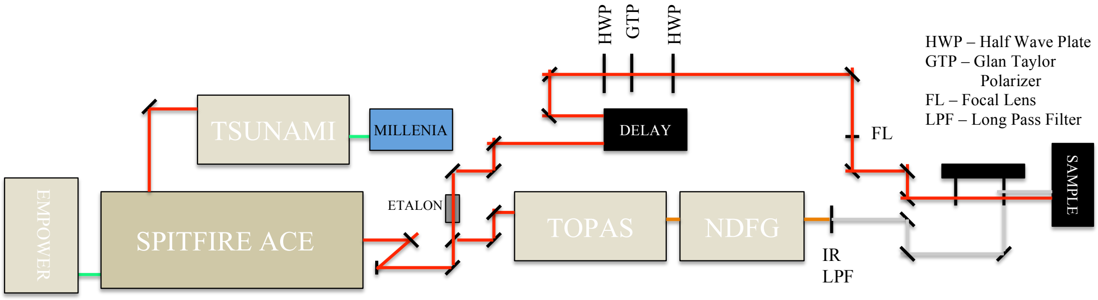

Figure 2.4. Schematic of the BBSFG-1 laser setup. This system utilizes an air-spaced Fabry-Pérot etalon to produce the visible picosecond pulse.

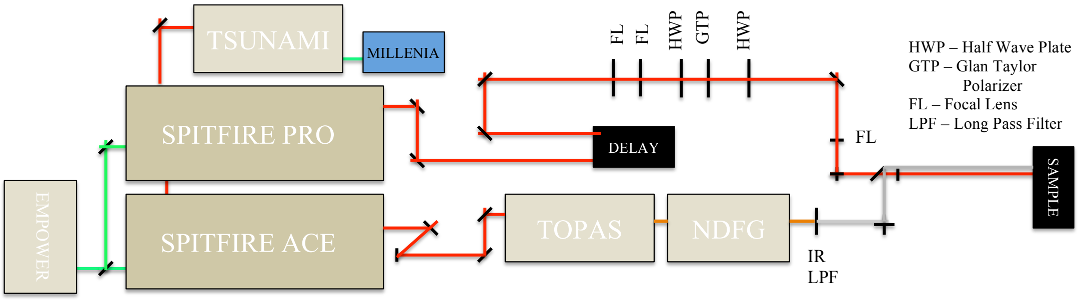

Figure 2.5. Schematic of the BBSFG-2 laser setup. This system uses a regenerative amplifier to generate the visible picosecond pulse.

Chapter 3: Effect of Cation Enrichment on Dipalmitoylphosphatidylcholine (DPPC) Monolayers at the Air-Aqueous Interface

Reproduced in part with permission from Adams, E.M.; Casper, C.B.; Allen, H.C. "Effect of Cation Enrichment on Dipalmitoylphosphatidylcholine (DPPC) Monolayers at the Air-Water Interface" *J. Colloid Interface Sci.*, **2016**, 478, 353-364. Copyright Elsevier

3.1 Introduction.

Sea spray aerosols (SSA) produced from wave breaking are known to impact climate.[2] Yet, their influence on radiative forcing, whether directly through light scattering and absorption[3] or, indirectly, by their ability to act as cloud condensation nuclei[14] and ice nucleating particles[11], remains uncertain. The impact of SSA on climate depends on their chemical composition[2], as this dictates their chemical and physical properties.[14,8,21] SSA are commonly complex mixtures of salts and organic species. Moreover, organic content and composition vary widely as they are driven by biological activity at the ocean surface.[17,70,18,71]

Recent studies of nascent sea spray generated during the course of a phytoplankton bloom found that four distinct particle types are produced.[21,26] Two of these particles types, organic carbon (OC) and sea-salt organic carbon (SSOC), have been characterized in terms of their chemical composition.[7,23] OC particles are composed of insoluble organic species and inorganic ions such as sulfate (SO_4^{2-}), sodium (Na^+), magnesium (Mg^{2+}), calcium (Ca^{2+}), and potassium (K^+). Notably, these particles lack a signature from chlorine (Cl^-).[7] The organic species in OC particles are thought to be aliphatic-rich lipids, likely phospholipids, which constitute a major class of lipids produced by phytoplankton.[23] Dried SSOC particles have a sea-salt core, mostly composed of NaCl, covered by an organic coating. Aerosol time-of-flight mass spectrometry (ATOFMS) and scanning transmission X-ray microscopy with near edge X-ray absorption fine structure (STXM-NEXAFS) measurements suggest that oxidized-rich species, such as fatty acids, make up a large fraction of the organic material in these particles.[7,23] Despite differences in composition, an enrichment of divalent ions occurs in both types of particles. Ca^{2+} is observed in OC particles[26], whereas Mg^{2+} and Ca^{2+} are both enhanced in SSOC particles; however, Mg^{2+} is much more prevalent.[7] Furthermore, in the case of the SSOC particles, the enrichment of these divalent ions as well as K^+ occurs at the interface of the particles[7,32], suggesting that these ions are coordinated to surface-active organics.

Complexation of ions to surface-active species, such as lipids, is known to alter their orientation[29], packing[27,28], and surface morphology.[66] Interfacial properties of organic films impact the chemical and optical properties of aerosols including albedo[12], hygroscopicity[9], and reactivity.[13] For example, it was shown that light scattering of organic-coated NaCl particles decreases as the volume fraction of organics increases.[12] To date, many studies of organic-coated aerosols have relied on dried salt cores selectively coated with an organic surfactant as model systems.[9,12,13] While valuable at providing insight into aerosol chemistry, these models lack some representative properties of aqueous aerosols generated from the ocean surface (although drying of the aerosol will occur in the atmosphere). Furthermore, most of these studies have used NaCl as the main inorganic salt, thus neglecting the importance of other marine-relevant ions such as alkaline earth cations (Ca^{2+}, Mg^{2+}). Therefore, in order to fully grasp the impact that ions have on marine aerosol properties, a fundamental understanding of how ion enrichment in a hydrated environment, especially enrichment of divalent ions, influences the surface properties of the organic coating is needed.

In this work, Langmuir monolayers of lipids spread on marine-relevant salt solutions in various concentration regimes are used as a model system to determine how monovalent and divalent cations alter the interfacial properties of organic-coated marine aerosols as they are entrained in the atmosphere. Dipalmitoylphosphatidylcholine (DPPC) was chosen as a representative lipid as it has been well studied[72–74], and is known to be enriched in the sea surface microlayer (SSML)[75,19], and therefore likely found in marine aerosols. Aqueous solutions consisting of monovalent (Na^+, K^+) and divalent (Mg^{2+}, Ca^{2+}) chloride salts were used to represent the aerosol aqueous salt core. Typical concentrations of these cations in seawater are 0.45 M (Na^+), 0.01 M (K^+), 0.05 M (Mg^{2+}), and 0.01 M (Ca^{2+}), respectively[31]. Here, the salt concentrations were varied from 0.3 to 2.0 M to represent different stages of marine aerosol evaporation and different degrees of ion enrichment at the interface. Similar Cl^- concentrations were used to directly compare effects due to cation identity. To determine the influence of cation identity and concentration on the interfacial phase behavior of the DPPC monolayer surface pressure-area isotherms were measured on the various salt solutions. In addition, Brewster angle microscopy (BAM) images were collected to assess the impact of cation enrichment on the surface morphology and refractive index of the DPPC monolayer. Infrared reflection-absorption spectroscopy (IRRAS) was used to determine potential cation effects on the conformational order of lipid alkyl chains and the extent of cation interaction with the phosphatidylcholine (PC) headgroup. Results reported here indicate that the surface properties of the lipid film are altered in the presence of highly concentrated ions, and that these alterations have impacts on the optical properties of marine aerosols, specifically the refractive index.

3.2. Experimental.

3.2.1. Materials.

1,2-Dipalmitoyl-*sn*-glycero-3-phosphocholine (DPPC) (> 99%, Avanti Polar Lipids) was used as received and dissolved in chloroform (HPLC grade, Fisher Scientific) to make a 1 mM solution. Sodium chloride (NaCl) (≥ 99%, ACS certified, Fisher Scientific), potassium chloride (KCl) (≥ 99%, ACS certified, Fisher Scientific), calcium chloride dihydrate ($CaCl_2 \bullet 2H_2O$) (≥ 99%, FCC grade, Fisher Scientific), and magnesium chloride hexahydrate ($MgCl_2 \bullet 6H_2O$) (≥ 99%, ACS certified, Fisher Scientific) were dissolved in water with a resistivity of 18.2 MΩ·cm and a measured pH of 5.6 (NANOpure Analytical Deionization System, model D4741, Barnstead/Thermolyne Corporation) to prepare stock solutions. These solutions were subsequently purified by a method that has been previously described.[69] Briefly, trace organic and inorganic impurities were removed by several filtrations through activated carbon filters (Whatman Carbon-Cap 75, Fisher Scientific). Cleanliness of the stock salt solutions was confirmed by the absence of spectral features in vibrational sum frequency generation (VSFG) spectra measured in the CH stretching region (2800–3000 cm^{-1}). Concentration of the stock salt solutions was determined by Mohr's chloride titration method.[76] Solutions of desired concentration were then prepared by dilution of the stock salt solutions. All prepared solutions had a final pH in the range of 5-7 and were sealed from the ambient environment. Equilibration to ambient temperature (23 ± 1 °C) for a period of at least 12 h was allowed before measurements were performed.

3.2.2. Methods.

Surface Pressure- Area Isotherms.

Surface pressure-molecular area (Π–A) compression isotherms were measured on a computer-controlled Langmuir trough (Minitrough, KSV Instruments, Finland; A_{total} = 144 cm^2) made of Teflon and equipped with two compression barriers. Surface pressure of the monolayer was monitored with a Wilhelmy plate made of filter paper (Ashland grade, Whatman). Prior to measurements the trough and barriers were thoroughly rinsed with ethanol and nanopure water. Cleanliness of the aqueous surface was ensured by sweeping the barriers across the surface, where an aqueous surface was considered clean when $\Pi \leq 0.2$ mN/m. Monolayers were formed by spreading dropwise an appropriate volume of the lipid solution on the aqueous surface using a microsyringe (Hamilton). Ten minutes were allowed to pass for evaporation of the spreading solvent before compression. Monolayers were compressed at a constant rate of 5 mm/min/barrier up to the compression limit of 55 mN/m, prior to collapse. Film leakage tends to occur at high surface pressures due to meniscus inversion of the solution surface,[77] which makes reaching the collapse pressure of the DPPC monolayer (72 mN/m) difficult. Experiments were stopped at 55 mN/m to avoid film leakage. Isotherms were repeated at least three times to ensure reproducibility. Standard deviations of the molecular area and surface pressure were ± 1 $Å^2$/molecule and ± 0.5 mN/m, respectively.

Brewster Angle Microscopy

Surface morphology of the DPPC monolayers was assessed using a custom-built BAM setup that has been previously described.[65,66] The BAM setup was detailed in Chapter 2. A blue background was selected to enhance image contrast. Images were collected simultaneously with the compression isotherms in which an image was recorded every 4.85 s to make a movie. Still frames were then extracted from the movie at appropriate surface pressures or mean molecular areas. Because the inclined position of the collection optics causes images to be focused only over a narrow region of the visual field, all images were cropped from the full 800 μm × 800 μm size to the most resolved region. Differences in the reflectance of each solution were accounted for by adjusting the Brewster angle (see Eq. (2.5)) such that each solution had a background gray level of 30 or less. The measured Brewster angle of each aqueous solution and the corresponding refractive index determined from the Brewster angle equation are listed in Table 3.1. Calculated refractive indices are in good agreement with literature.[78]

Refractive index of the monolayer (n_m) on various solutions was calculated from BAM images using the following relation:[50]

$$d = \frac{\lambda\sqrt{R_p}}{\pi \sin\,(2\theta_B - 90)} \frac{n_m^2(n_a^2 - n_s^2)}{\sqrt{n_a^2 + n_s^2}(n_a^2 - n_m^2)(n_s^2 - n_m^2)} \tag{3.1}$$

where d is the monolayer thickness, λ is the laser wavelength, and R_p is the measured reflectivity of p-polarized light from the surface. As d and n_m change concurrently, they cannot both be solved for using Eq. (3.1). For simplicity, it was assumed that d remains constant in the monolayer liquid condensed phase with a value of 2.48 nm, as determined from previous BAM experiments.[67] Reflectance values were related to the gray levels of the camera with calibrations curves as has been previously described.[79,80] Gray levels were averaged for horizontal lines at three separate pixels to determine an overall average gray level for each cropped BAM image. The gray level was then transformed to a reflectance value based on the calibration curves.

Infrared reflection-absorption spectroscopy (IRRAS)

IRRAS spectra were collected using a custom-built setup placed in the chamber of a FTIR spectrometer (Spectrum 100, Perkin Elmer). The IRRAS setup was described in Chapter 2. The incident mirror was positioned before the J-Stop Image distance (i.e., the set focus point of the incoming IR beam in the FTIR chamber) so that the incident beam was most focused at the aqueous surface. An incident angle of 46° from the surface normal was used here. The barriers of the trough were either held at a constant mean molecular area (MMA) or allowed to oscillate to maintain a fixed surface pressure during measurements. All spectra were obtained with a HgCdTe (MCT) detector as a single beam measurement, with a single beam measurement of the respective bare aqueous surface used as the background spectrum. Spectra covered a range from 450 to 4000 cm^{-1} and were averaged over 300 scans with a resolution of 4 cm^{-1}. Measurements were repeated at least three times to ensure reproducibility. Post-processing of spectra was done in OriginPro 9.0 (OriginLab), where baseline correction was done by fitting a third-order polynomial in the region of interest. Final spectra shown here are an average of at least three baseline-corrected spectra.

3.3 Results and Discussion

3.3.1. Cation identity and salt concentration effects on the phase behavior and stability of DPPC monolayers

Π–A compression isotherms of DPPC monolayers on different chloride salt solutions (NaCl, KCl, $MgCl_2$, and $CaCl_2$) with varying concentrations are shown in Figure 3.1. An isotherm of DPPC on water is also given for reference. The phase behavior of DPPC on water has been well documented.[81] With decreasing MMA (and at ambient temperature), the DPPC isotherm typically exhibits the following phases: gaseous (G), liquid-expanded (LE), LE-liquid-condensed (LC) coexistence phase seen in the form of a plateau region, and LC.

All phases described above are also present for DPPC monolayers on NaCl solutions (Figure 3.1a). Relative to water, an increase in MMA occurs in the low surface pressure regime for 0.6 M NaCl. As the monolayer is compressed to higher surface pressures (> 35 mN/m), DPPC molecules occupy the same MMA as on water, suggesting that excess

Na^+ ions are squeezed out of the monolayer. A total expansion of the monolayer occurs on the 2.0 M NaCl solution, where a larger MMA relative to water occurs at all surface pressures. The phase behavior of DPPC on NaCl solutions has been studied extensively, and a shift to higher MMAs in the LE and LE-LC coexistence phases has also been previously observed for moderately concentrated (≥ 0.1 M) solutions[29,82–87] The extent of the MMA shift seems concentration-dependent, as it increases by 3-6 $Å^2$/molecule for concentrated solutions (≥ 0.5 M),[29,84,85] and is shifted 1-2 $Å^2$/molecule for 0.1 M solutions.[82,83]

Similar to the NaCl series, 0.6 and 2.0 M KCl solutions cause the DPPC monolayer to occupy a larger MMA compared to water (Figure 3.1b). Also like Na^+, K^+ ions are squeezed out of the monolayer at high surface pressures (> 25 mN/m) for 0.6 M KCl, but cause an expansion at all surface pressures on 2.0 M KCl. The impact of K^+ on the phase behavior of DPPC, or any other saturated PCs in general, has been less studied than Na^+,[88,89] but previous reports are consistent with results presented here, where expansion of the monolayer occurs in the presence of K^+.

In the case of 0.6 M solutions, K^+ has a smaller change in area (ΔA) relative to water than Na^+ in the LC phase (Figure 3.2a), which may indicate that K^+ ions do not interact as strongly with the DPPC headgroup as Na^+ ions. MD simulations support this, with many suggesting that at low concentrations (~0.2 M) K^+ only weakly interacts, if at all, with PC headgroups, while Na^+ strongly interacts.[90,91] Equilibria calculations, however, find that PC-K^+ complexes are more stable than PC-Na^+ complexes.[92] No definitive conclusion on relative binding affinity of Na^+ vs. K^+ to DPPC can be made from Π-A isotherms presented here as contrary ΔA values are observed between 0.6 and 2.0 M solutions. K^+ has a larger ΔA than Na^+ for 2.0 M solutions and is likely not indicative of increased PC-K^+ interactions, but rather the presence of excess unbound K^+ ions in the interfacial region which cause increased electrostatic repulsions, and force DPPC molecules to be further apart. Comparison of ΔA for 2.0 M NaCl and KCl solutions at several different surface pressures (Figure 3.2b) shows similar ΔA values for the two cations. Results shown here indicate that at high concentrations monovalent cations Na^+ and K^+ interact similarly with DPPC molecules, where expansion of the monolayer is likely due to increased electrostatic repulsions in the interfacial region.

The impact of divalent cations on the phase behavior of the DPPC monolayer depends on the identity of the cation. For instance, Mg^{2+} has a similar effect to monovalent ions, in which $MgCl_2$ solutions result in DPPC molecules occupying a larger MMA relative to water. Expansion becomes more evident with increasing concentration (Figure 3.1c), also similar to monovalent ions. In the case of 0.3 M $MgCl_2$, the isotherm largely overlaps with that of water with deviations occurring in the LC phase, in which a smaller MMA is observed (Figure 3.2a). For 1.0 M $MgCl_2$ a larger MMA occurs in all phases except LC (> 40 mN/m), which overlaps with the DPPC isotherm on water. This indicates that for 0.3 and 1.0 M solutions Mg^{2+} ions are likely being squeezed out of the monolayer at high surface pressures. The isotherm of DPPC on 2.0 M $MgCl_2$ is expanded at all MMAs. In contrast, previous studies have found that expansion of PC monolayers also occur at all MMAs in the presence of Mg^{2+}.[93,94] These studies, however, used significantly lower concentrations (< 50 mM) of $MgCl_2$ or PCs with different chain lengths and degree of saturation, which makes direct comparison to results here difficult. In any case, the similarity in DPPC phase behavior on $MgCl_2$ compared to NaCl and KCl solutions suggests that Mg^{2+} (most likely Mg^{2+} hexahydrate)[95] interacts with DPPC in a manner similar to monovalent ions, i.e., with one cation binding per lipid headgroup (1:1 binding). This is likely due to the preference of Mg^{2+} to strongly retain its solvation shell.[95] Density functional theory calculations have determined that the net charge of a solvated Mg^{2+} ion is +1.29, which could account for the similar behavior to monovalent ions.[96]

$CaCl_2$ solutions have the opposite effect on DPPC compared to $MgCl_2$, resulting in a condensation of the monolayer (Figure 3.1d). Isotherms at all concentrations occupy a smaller MMA relative to DPPC on water (Figure 3.2a). The only exception is the LE phase, which is expanded relative to water (Figure 3.2b). The condensation effect becomes more enhanced with increasing concentration, as observed by the decrease in the surface pressure of the LE-LC phase as the Ca^{2+} concentration increases. Results presented here contradict previously published studies including work from our group and others, in which an expansion of the PC monolayer occurred on $CaCl_2$ solutions.[29,84,97–99] However, large discrepancies exist between reported results. For example Lee et al. reported a large expansion (~15 Å^2/molecule) in the LE phase for a 0.2 mM $CaCl_2$ solution,[98] while other studies showed only small MMA increases ($\leq$ 1 Å^2/molecule) for 5 mM and 0.1 M solutions.[97,100] More recent studies done in our group have demonstrated the impact of salt purity and purification method on interfacial measurements,[69] especially when investigating ion binding to lipids.[101] Furthermore, studies done by Kewalramani et al. on dimyristoylphosphatidylcholine (DMPC) monolayers found that aqueous solutions made from unbaked salts impacted the surface pressure at which the DMPC LE-LC coexistence phase occurred.[30] They further showed that Ca^{2+} lowered the LE-LC transition pressure relative to water by 4.3 mN/m; Mg^{2+} also lowered the transition pressure, but to a much lesser extent (0.7 mN/m). Results presented here for the lowest concentration (0.3 M) are consistent with that study as the LE-LC transition pressure was lowered by 0.8 mN/m for Ca^{2+}, but was not significantly changed for Mg^{2+}. While showing similar trends, direct comparisons to the study by Kewalramani et al. are difficult to make as the lipid of interest (DMPC), temperature (15°C), and ion concentration (150 mM) were significantly different than those used here. Yet, Kewalramani et al. noted that the purity of salts influenced the phase behavior of the phospholipid, which demonstrates the importance of removing organic contaminants when investigating lipid-ion systems. This factor could explain, at least in part, some of the differences observed between in isotherms presented here and those reported previously in the literature.

The opposing trends observed in DPPC isotherms on $MgCl_2$ and $CaCl_2$ solutions suggest that these divalent cations interact differently with the PC headgroup. In the presence of Ca^{2+}, DPPC molecules are able to pack more tightly as evidenced by the 2 $Å^2$/molecule decrease in molecular area in the LC phase (Figure 3.2a). In order to explain this decrease, two possible scenarios can be put forward: (1) Ca^{2+} acts as a bridge between two neighboring lipids, forming a 2:1 DPPC:Ca^{2+} complex; (2) Ca^{2+} causes the reorientation of the PC headgroup. Binding constant calculations and MD simulations have both found that formation of 2:1 complexes are more probable than 1:1 complexes.[90,99] Yet, recent surface potential measurements suggest that reorientation of the PC headgroup occurs in highly concentrated Ca^{2+} solutions (2 M).[67] Both scenarios likely occur to some degree, but more sensitive techniques such as nuclear magnetic resonance (NMR) or vibrational sum frequency generation (VSFG) spectroscopy are needed to clarify this. In the case of Mg^{2+}, its behavior is similar to that of a monovalent ion.

To determine the influence of cation enrichment on the rigidity of the monolayer the isothermal compressibility modulus ($C_s^{-1} = -A_\Pi(\partial\Pi/\partial A_\Pi)_T$, where A_Π is the molecular area at the corresponding Π) was obtained from the slope of each compression isotherm shown in Figure 3.1. The compressibility modulus of the DPPC monolayer on water is shown in Figure 3.3a. With increasing surface pressure the compressibility modulus first reaches a maximum value of ~25 mN/m before decreasing back to 0 mN/m at a surface pressure of 8.4 mN/m, which corresponds to the LE-LC coexistence phase. As surface pressure further increases past this point, the compressibility modulus reaches a maximum value of 200 mN/m, indicative of a monolayer in the LC phase.[102] Finally, the compressibility modulus returns to 0 mN/m when the monolayer approaches its collapse pressure. Experimental values of compressibility modulus reported here for each phase of DPPC are in good agreement with those found in literature.[103,104] Surprisingly, no significant change in the compressibility modulus was observed in the LC phase for any cation investigated. This implies that the rigidity of the DPPC monolayers in the LC phase does not depend on the cation identity or concentration. The only salt-induced effect observed in the compressibility modulus is a small change in the surface pressure at which the LE-LC phase occurred (Figure 3.3a-b). Na^+ and K^+ have similar surface pressure values, which are higher than water at all concentrations. An increase in the surface pressure of the LE-LC phase relative to water indicates a stabilization of the monolayer. In contrast, the monolayer becomes less stable with increasing Ca^{2+} concentration, as a decrease in the surface pressure occurs. For Mg^{2+} the surface pressure remains essentially unchanged from that on water for salt concentrations below 2.0 M. However, a significant increase in surface pressure occurs for 4.0 M Cl^-, suggesting that stabilization of DPPC does not occur until there is a significant enrichment of Mg^{2+} ions at the interface.

3.3.2 Cation identity and salt concentration effects on the surface morphology of DPPC monolayers

The surface morphology of DPPC monolayers on water in all phases is consistent with literature,[105] but results presented here focus on the LE-LC phase as the surface morphology in this region is most impacted by the presence of ions. BAM images presented in Figure 3.4 show the surface morphology of DPPC in the LE-LC phase on water, NaCl, and KCl solutions. Darker (or black) and brighter regions in the images represent, respectively, lipid-poor and lipid-rich areas. It can be seen that on water, small (30 μm), multi-lobed lipid domains are present. At low concentrations (0.6 M), both Na^+ and K^+ appear to have little influence on the surface morphology compared to water, as similar small, multi-lobed domains are observed. Yet, the number density of DPPC LC domains has increased relative to water (Table 3.2), with K^+ having a larger number density than Na^+. Concurrently, the average size of domains decreases as number density increases. Based on nucleation theory, the size and number of domains formed in the coexistence region depends on their free energy, which is related to the competing effects of line tension and electrostatic repulsion.[106] Line tension arises from van der Waal interactions of alkyl chains, and favors formation of circular domains. Electrostatic repulsions cause formation of elongated structures that are often branched or dendritic in shape. The higher number of smaller sized domains observed in the presence of monovalent cations stems from increased disorder in the monolayer (i.e. expansion) as ions compete with DPPC molecules to occupy surface sites, which leads to decreased line tension and increased electrostatic repulsions. A lower line tension causes an increased number of domains of smaller size to form.[107]

Alterations to the surface morphology do occur at high concentrations. In the case of 2.0 M NaCl, domains are much smaller (15-20 μm), tightly packed, and darker (less contrast), suggesting that the refractive index or thickness of the monolayer has changed. Similarly, darkening of the image occurs for 2.0 M KCl, but the monolayer forms an inhomogeneous film with no distinct domains apparent. In general, it seems that monovalent ions do not influence the surface morphology of the monolayer until they reach sufficient concentration in the interfacial region.

Divalent cations, however, have a distinct impact on the surface morphology even at low concentrations. BAM images in Figure 3.5 show the surface morphology of the LE-LC phase of DPPC on $CaCl_2$ and $MgCl_2$ solutions at 0.3, 1.0, and 2.0 M. On 0.3 M $CaCl_2$ solutions DPPC forms domains that are on average less than half the size as those on water. The number density of LC domains increases by five-fold relative to water (Table 3.2), and domains are circular in shape instead of multilobed, indicating that an increase in line tension occurs in the presence of Ca^{2+}.[108] The decrease in size and increase in number density is consistent with fluorescence microscopy studies of DPPC on $CaCl_2$ solutions ($\leq$ 1.0 M).[84,97] As the concentration of $CaCl_2$ increases to 1.0 M, an inhomogeneous monolayer develops in which individual domains can no longer be distinguished. At 2.0 M the monolayer inhomogeneity persists, but the image is darker relative to 1.0 M $CaCl_2$. Compared to water, domains on 0.3 M $MgCl_2$ are also smaller and more numerous. This is somewhat surprising considering that the isotherm showed little deviation from that of water Yet, BAM reveals that Mg^{2+} also causes an increased number of domains that are smaller in size. It can be seen that, unlike Ca^{2+}, domains retain their multilobed shape in the presence of Mg^{2+}, which indicates that electrostatic repulsions are the dominant interfacial force. The observed changes in the surface morphology arise from decreased line tension, similar to the monovalent ions. DPPC molecules form an inhomogeneous monolayer on 1.0 M $MgCl_2$, which becomes darker on 2.0 M $MgCl_2$. Comparison of the 1.0 and 2.0 M solutions shows that DPPC monolayers formed on $MgCl_2$ appear to be more compact than on $CaCl_2$. Although Mg^{2+} and Ca^{2+} have opposite effects on DPPC phase behavior (i.e., expansion vs. condensation), imaging of the surface morphology shows that both divalent cations cause a larger number of smaller domains to form, albeit by different mechanisms.

In general, BAM images obtained on highly concentrated solutions, with the exception of K^+, show a significant decrease in the monolayer reflectance. Darkening of the images cannot be attributed to changes in the Brewster angle, as it was set for each aqueous solution to have the same initial reflected gray level for the bare solution surface. Two scenarios could possibly explain this observation: (1) fluidization of the monolayer occurs, where overall ordering of the alkyl chains decreases due to an increase of *gauche* defects in the chain, thus resulting in changes in relative thickness or refractive index; (2) alterations in the alkyl chain orientation, in which highly ordered chains (trans conformation) become more parallel to the aqueous surface, which would also change the relative thickness or refractive index of the monolayer. As a decrease in reflectance was observed for both LE-LC and LC phases (Figure 3.6), it is unlikely that fluidization of the monolayer occurs since DPPC molecules were able to reach surface pressures of 55 mN/m or greater on all solutions, indicating that highly ordered films with strong van der Waals interactions are formed. This is further supported by IRRAS measurements, which is discussed in more detail in the next section.

If it is assumed that the thickness of a homogeneous, highly ordered monolayer remains roughly constant, then calculations reveal that the monolayer refractive index in the LC phase ($\Pi = 45$ mN/m) changes with salt concentration (Figure 3.7.; see Table 3.3 for calculated n_m values). Increasing salt concentration results in a decrease in refractive index, regardless of cation identity. While changes in the refractive index relative to water seem somewhat small ($\sim 10^{-2}$), ellipsometry studies have determined that the refractive index of DPPC on water increases by 0.021 from the LE to LC phase,[54] showing how the alkyl chain conformation dictates the monolayer refractive index. DPPC monolayers on divalent chloride solutions have a smaller refractive index compared to monovalent ones (n_m = 1.457 vs. 1.478) at the highest concentration measured. This indicates that divalent cations have a greater influence on the alkyl chains conformation and is consistent with previous studies.[109] However, comparison of values at the same chloride concentration (2 M Cl^-), shows that the refractive index is smaller for monovalent ions than Mg^{2+}. This finding is in line with Π-A isotherms that suggested Mg^{2+} interacts with DPPC in a manner similar to a monovalent ion (1:1 binding).

3.3.3 Cation identity and salt concentration effects on the intermolecular interactions of DPPC monolayers

IRRAS: CH region

IRRAS spectra were collected in the LE-LC phase (70 Å^2/molecule with respective surface pressures shown in Figure 3.3b) and the LC phase (40 mN/m) to provide additional information on the effect of highly concentrated cations on a DPPC monolayer. Peak positions of the methylene (CH_2) vibrational modes are sensitive to the conformational order of the alkyl chains, and can provide insight into the relative number of *trans* and *gauche* conformations in the monolayer. A shift to lower wavenumbers indicates that the alkyl chains have more *trans* bonds.[57] Such a trend can be observed in Figure 3.8, where the CH_3 asymmetric ($\nu_{as}(CH_3)$),, CH_2 asymmetric ($\nu_{as}(CH_2)$),, and CH_2 symmetric ($\nu_s(CH_2)$), modes at 2963, 2922 and 2853 cm^{-1}, respectively, shift to lower wavenumbers when DPPC is compressed to a higher surface pressure.[83] Spectra of DPPC on 2.0 M NaCl and 2.0 M $CaCl_2$ solutions (Figure 3.8b,c) show a shift to lower wavenumbers relative to water (Figure 3.8a), even in the LE-LC phase. The shift induced by Ca^{2+} is larger than Na^+ in the LE-LC phase, indicating that alkyl chains are more ordered in the presence of Ca^{2+}, but no difference in peak position is observed for the two ions in the LC phase. It is especially interesting that 2.0 M Na^+ increases the order of the alkyl chains in the LE-LC phase as the Π-A isotherms showed an expansion of the monolayer at this concentration. Previous experimental studies have found that concentrated NaCl and NaI solutions disrupt chain ordering at low surface pressures,[83,84] but MD simulations report that Na^+ induces a higher ordering of the chains.[90,110]

Figure 3.9 displays the peak position of the $\nu_{as}(CH_2)$ mode as function of [Cl^-] for all ions investigated. In the LE-LC phase (Figure 3.9a), K^+, Na^+, and Ca^{2+} cause the peak position to shift to lower wavenumbers with increasing [Cl^-]. This suggests that alkyl chain conformation is dependent upon the cation concentration. Comparison of the peak position for monovalent ions to Ca^{2+} reveals that monovalent ions induce a higher degree of ordering. Due to their smaller size, monovalent ions may interact with the carbonyl group of the lipid chains,[90] which could cause higher ordering and explain the increased MMA in the Π-A isotherms. The LC phase seems to be less impacted by the cations than the coexistence phase (Figure 3.9b), as shifts in the peak position of the DPPC alkyl chain $\nu_{as}(CH_2)$ mode are less than 1 cm^{-1} from the value measured on water. Generally, it can be seen that with the exception of 0.3 M $MgCl_2$, the alkyl chains are slightly more ordered in the presence of cations. It is likely that at high surface pressures cations are squeezed out of the monolayer and primarily interact with the hydrophilic portion of the lipid.

Unlike the other cations, Mg^{2+} causes the $\nu_{as}(CH_2)$ vibration to shift to higher wavenumbers in the LE-LC phase, independent of salt concentration, and indicates that *gauche* defects exist in the alkyl chain. Figure 3.10 shows spectra of DPPC on $MgCl_2$ solutions in the coexistence region. It can be seen that the intensity of the $\nu_{as}(CH_2)$ and $\nu_s(CH_2)$ peaks decreases on $MgCl_2$ solutions compared to water. For 0.3 M Mg^{2+} a feature appears in the spectrum at 2883 cm^{-1} that can be attributed to the CH_3 symmetric stretch ($\nu_s(CH_3)$). The appearance of this vibrational mode confirms that *gauche* defects exist within the alkyl chain, as the existing IRRAS polarization is sensitive to orientation of the terminal methyl, which indirectly reports on *gauche* vs. *trans* bonds in the alkyl chains. This feature disappears for higher concentrations of Mg^{2+}, but the intensity of the methylene peaks do not change, indicating that the relative number density or orientation of DPPC molecules remains the same for the three different concentrations. Spectra collected here suggest that the interaction of Mg^{2+} with DPPC is unique, but Π-A isotherms indicated that Mg^{2+} behaves similarly to monovalent ions. From ΔA plots (Figure 3.2b), it can be seen the expansion of DPPC is twice that of both Na^+ and K^+ (18 vs. 9 $Å^2$/molecule), which is likely due increased electrostatic repulsions from the +2 charge of magnesium. The increased space between molecules could allow for the formation of *gauche* defects to occur in the presence of Mg^{2+}. A 1:1 binding is still likely for Mg^{2+} ions (which are hydrated, $Mg^{2+}\bullet 6H_2O$) as IRRAS spectra of the phosphate region, discussed in the next section, show that Mg^{2+} has similar interactions with the phosphate moiety as monovalent ions.

IRRAS: Phosphate region

Vibrational modes of phospholipid headgroups have been well characterized and used to determine the degree of interaction that cations have with the negatively charged phosphate group.[109,111,112] Spectra of the phosphate vibrational modes of DPPC on 2.0 M KCl in the LE-LC and LC phases are shown in Figure 3.11. The asymmetric and symmetric PO_2^- stretching ($\nu_{as}(PO_2^-)$ and $\nu_s(PO_2^-)$) modes are observed at 1230 and 1087 cm^{-1}, respectively. Peaks at 1170 and 1070 cm^{-1} can be attributed to the CO-O-C asymmetric and symmetric stretches (ν_{as}(CO-O-C) and ν_s(CO-O-C)) of the carbonyl esters.[111,112] A C-O-P-O-C stretch is known to occur at 1060 cm^{-1}, and is sometimes discernable from the ν_s(CO-O-C). The feature at 975 cm^{-1} is attributed to $N-(CH_3)_3$ asymmetric stretches ($\nu_s(N-(CH_3)_3)$) of the choline group. The shoulder observed on the 975 cm^{-1} band, located at 950 cm^{-1}, is generally thought to be due to C-N asymmetric stretching of the choline as well.[111]

Compression of the DPPC monolayer to a higher surface pressure on 2.0 M KCl leads to an increase in the intensity of all peaks due to increased number density of DPPC molecules. Shifts in the ($\nu_{as}(PO_2^-)$ and ($\nu_s(PO_2^-)$ to higher wavenumbers are likely caused by the ion-induced dehydration of the phosphate group. For all four cations studied here, phosphate group dehydration was observed in the LC phase, consistent with previously reported literature, where dehydration occurs upon monolayer compression regardless of whether ions are present in the solution.[29,73,83]

To reveal this ion-induced dehydration of the phosphate group, the peak position of the ($\nu_{as}(PO_2^-)$ mode in the presence of each cation is plotted as a function of [Cl^-] for both the LE-LC and LC phases (Figure 3.12). For the coexistence phase a shift to lower wavenumbers relative to water is observed for Na^+, K^+, and Mg^{2+}, indicating that the phosphate headgroup is more hydrated in the presence of these particular cations. In the LC phase, however, neither Na^+ nor K^+ influence the peak position of this mode. This is also consistent with studies by Binder et al. and Maltseva et al.,[109,112] which found that monovalent ions did not alter the peak position of this mode in the condensed phase. The difference in behavior between the LE-LC and LC phase observed here suggests that at low lipid coverage monovalent cations have little or no interaction with the phosphate moiety, instead likely interacting with the carbonyl group. As the monolayer is compressed ions are forced away from the carbonyls, where they weakly interact with the phosphate group.

It is apparent from Figure 3.12 that the interaction of Mg^{2+} and Ca^{2+} ions with the phosphate moiety is very different. As previously noted, in the LE-LC phase Mg^{2+} increases hydration of the phosphate group relative to water. The largest decrease in peak frequency occurs for 0.6 M Cl^-. After this point the peak frequency increases until it recovers at 4.0 M Cl^- the same value as DPPC monolayers on water. Mg^{2+} ions are known to retain their first and second solvation shells at low concentrations, but as $[Mg^{2+}]$ increases there are an insufficient number of water molecules to complete the second solvation shell.[113] This could account for the increased headgroup hydration at low concentrations followed by dehydration with increasing concentration. In the LC phase Mg^{2+} causes dehydration of the headgroup with increasing concentration, consistent with previous studies.[109,112]

Ca^{2+}, unlike Mg^{2+}, induces dehydration of the phosphate group in both the LE-LC and LC phases. Dehydration is much more apparent in the LC phase (Figure 3.12), as the increase in peak position to higher wavenumbers is larger for 0.6 and 2.0 M Cl^- in this phase compared to LE-LC phase. Interestingly, a large shift from 1232 to 1242 cm^{-1} is observed from 2.0 to 4.0 M Cl^- in the LE-LC phase. Studies by Casillas-Ituarte et al. reported a 9 cm^{-1} shift of the ($\nu_s(PO_2^-)$) mode in the presence of Ca^{2+} when comparing silica-supported (dehydrated) monolayers and monolayers on aqueous solutions.[29] A significant shift (11 cm^{-1}) of the ($\nu_s(PO_2^-)$) mode was also observed here, as can be seen in Figure 3.13. These spectra show the phosphate region of DPPC in the LE-LC phase on $CaCl_2$ solutions at various salt concentrations. It is notable for the 2.0 M solution that, in addition to shifts in the PO_2^- modes, the asymmetric mode narrows significantly while the symmetric mode broadens. These features were similarly observed in the LC phase, indicating that dehydration is independent of lipid packing density. This finding suggests that the phosphate moiety is substantially dehydrated in the presence of 2.0 M $CaCl_2$, and that there may be a change in the orientation of the PC headgroup as the transition moment strength of the phosphate modes has changed. Femtosecond IR pump-probe experiments suggest that solvent-separated ion pairs with long lifetimes (> 200 ps) form between Ca^{2+} ions and phospholipid headgroups.[114] The formation of strong ion pairs at high concentrations could contribute to the changes observed for the ($\nu_s(PO_2^-)$) mode. Recent surface potential measurements of DPPC monolayers on $CaCl_2$ solutions have indicated that there is a reorientation of the headgroup in the high concentration regime,[67] but more sensitive measurements are needed to accurately determine if this is the case.

3.4 Conclusions

The goal of this study was to determine how the concentration of monovalent and divalent cations, especially in a highly concentrated regime, impacts the interfacial organization and structure of a DPPC monolayer, and to understand the mechanism of such. To the best of the authors' knowledge, this is the first time that lipid monolayers on such highly concentrated solutions have been studied. Surface pressure-area isotherms show that Na^+, K^+, and Mg^{2+} cause a monolayer expansion that increases with salt concentration, consistent with previous literature.[84,93] The phase behavior of Ca^{2+} contradicts previous reports,[29,84,99] demonstrating that purification of salt solutions is necessary as impurities cause contradictory results even for stated salt purities greater than 99%. Imaging of the surface morphology reveals that increasing salt concentration leads to disruption of lipid packing, resulting in a monolayer that resembles an expanded state. IRRAS measurements, however, find that cations, with the exception of Mg^{2+}, cause the alkyl chains to be more ordered on highly concentrated salts. Further analysis of BAM images indicates that the monolayer refractive index decreases with increasing salt concentration, suggesting that orientation of the alkyl chains changes as cations become enriched in the interfacial region. Probing of the headgroup-cation interactions with IRRAS revealed that monovalent cations had weak interactions with the phosphate group, consistent with literature.[109,112] The interaction of Mg^{2+} with the headgroup depended upon cation concentration and lipid packing density. Dehydration of the phosphate group occurred in the presence of Ca^{2+}, in agreement with previous studies,[29,109,112] but substantial dehydration of the headgroup was observed for the first time in an aqueous environment when the lipid/aqueous interface was saturated with Ca^{2+} ions.

These results have implications for organic-coated aerosols, as several of the ions studied here have been found to be enriched in these aerosols,[23,26,32] especially Mg^{2+}.[7] Since the refractive index of a lipid monolayer is dependent on the concentration of ions in solution, results found here have the potential to aid climate modelers,[115] as it is likely that the refractive index of organic-coated aerosols will change as the particle experiences loss or uptake of water from the environment. Furthermore, the ion concentration impacts the surface morphology (i.e., packing density) of lipid films, which will influence the rate of water exchange with the atmosphere, resulting in alterations to the size, reactivity, and ability of aerosol particles to scatter light and act as a cloud condensation nuclei.[14] In general, results found here indicate that properties of organic-coated aerosols will depend on the concentration of ions present.

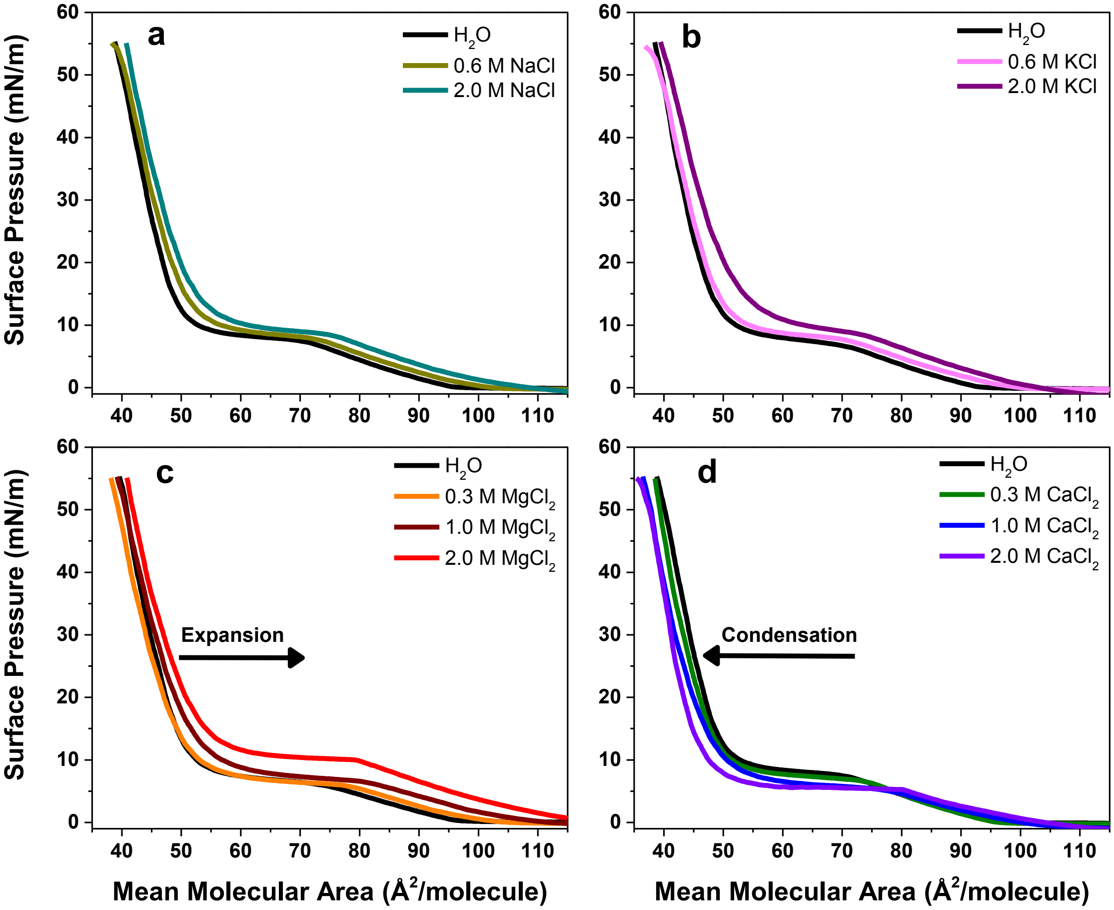

Figure 3.1. Π-*A* isotherms of DPPC monolayer on (a) NaCl (b) KCl (c) $MgCl_2$ and (d) $CaCl_2$ solutions with varying salt concentrations. The collapse phase is not shown. NaCl and KCl salts expand the DPPC monolayers, while $MgCl_2$ condenses or expands the monolayer depending upon the phase and concentration. $CaCl_2$ condenses the monolayer.

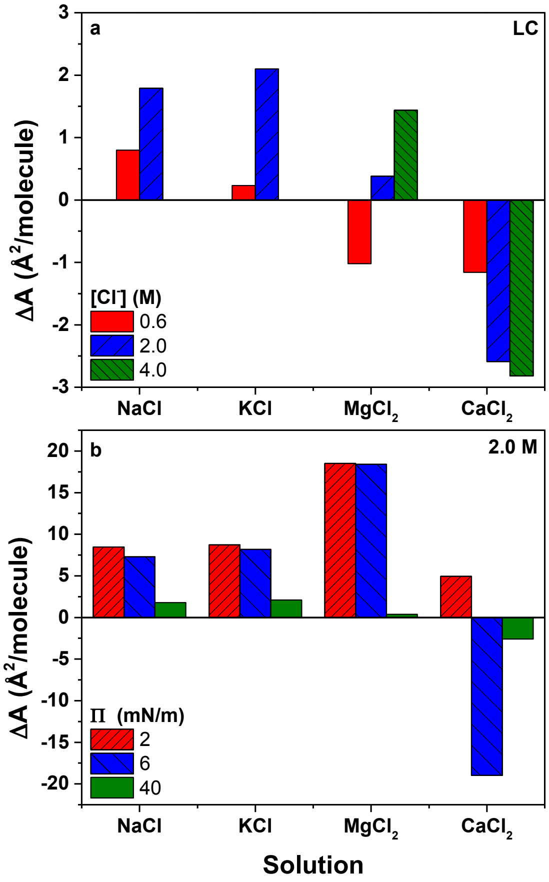

Figure 3.2. Change in MMA for salt solutions relative to water for DPPC monolayers (a) in the LC phase (40 mN/m) and (b) on 2.0 M salt solutions.

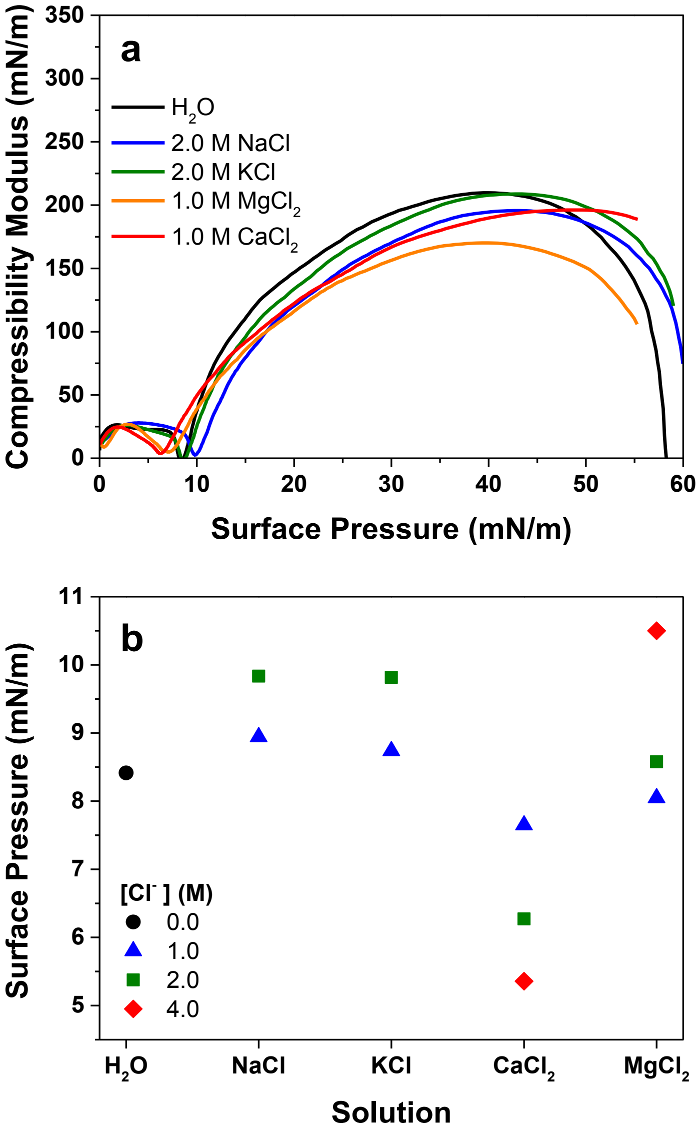

Figure 3.3. (a) Compressibility modulus of DPPC monolayer on water and 2.0 M Cl^- salt solutions as a function of surface pressure. (b) Salt-induced effect on the surface pressure at which the LE-LC phase occurs. Stabilization of the monolayer occurs in the presence of Na^+, K^+, and Mg^{2+}, but not Ca^{2+}.

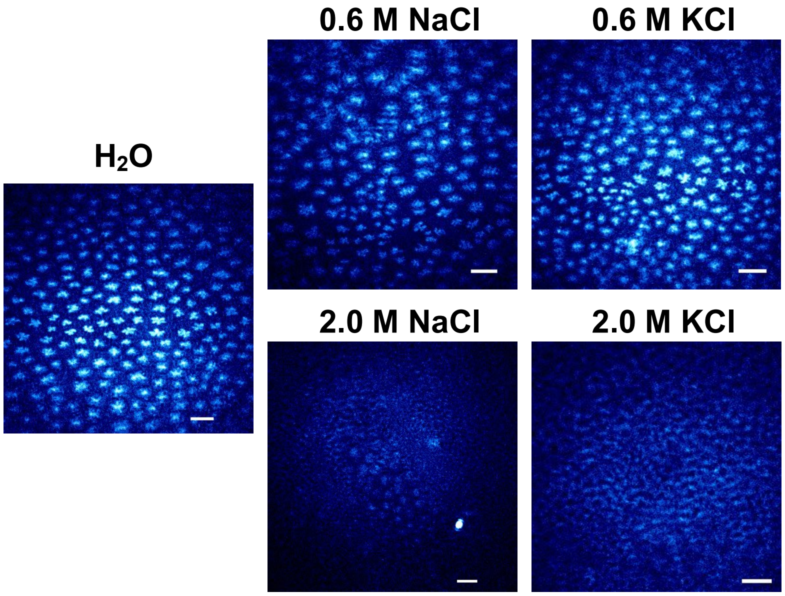

Figure 3.4. BAM images of DPPC monolayers in the LE-LC phase on water, NaCl, and KCl solutions. All images were taken at 70 Å^2/molecule. Note the increased number density of DPPC LC domains and the presence of a population of smaller LC domains with the 2 M solutions. The scale bar is 50 μm.

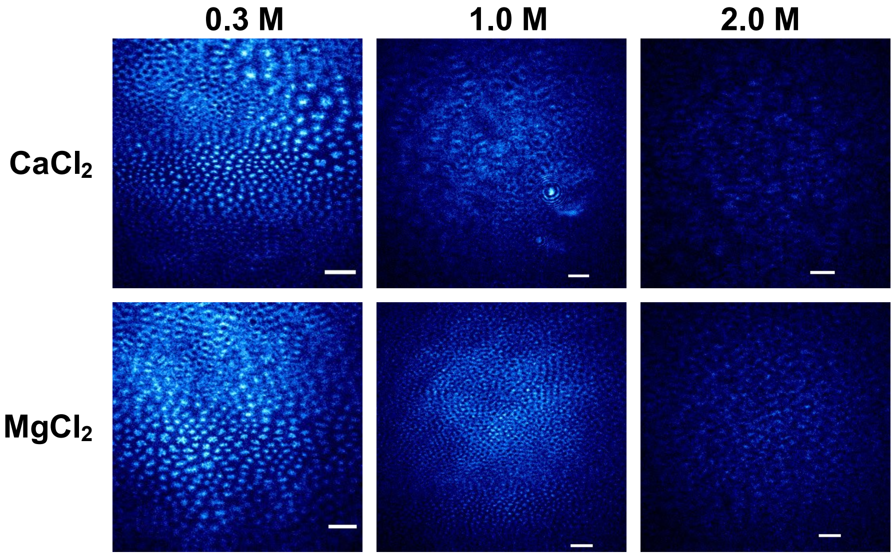

Figure 3.5. BAM images of DPPC monolayers in the LE-LC phase on $CaCl_2$ and $MgCl_2$ solutions with increasing concentration. All images were taken at 70 Å^2/molecule. Note the increasing diffuseness of the domain structure as divalent salt concentrations are increased, and the variation of DPPC domain morphology, e.g., for 1 M $CaCl_2$ vs. $MgCl_2$ solutions. The scale bar is 50 μm.

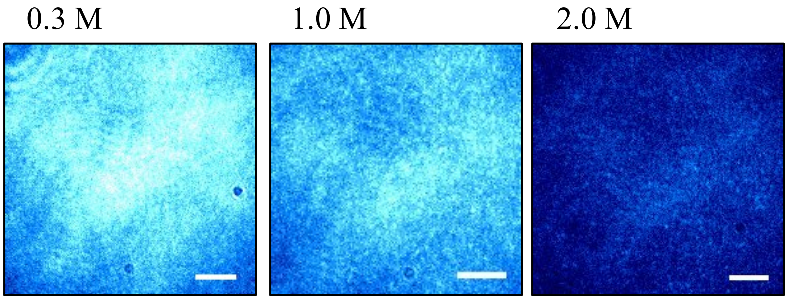

Figure 3.6. BAM images of DPPC monolayers in the LC phase (Π = 45 mN/m) on $MgCl_2$ solutions for different salt concentrations. The intensity of light reflected from the monolayer decreases with increasing $MgCl_2$ concentration. The scale bar is 50 μm.

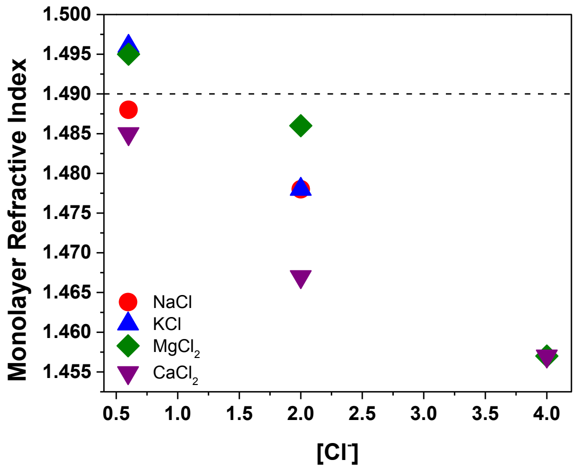

Figure 3.7. Monolayer refractive index (n_m) of DPPC on solutions of NaCl, KCl, $MgCl_2$, and $CaCl_2$ as a function of [Cl^-]. The horizontal dashed line indicates the monolayer refractive index of DPPC on water. Refractive index decreases with increasing salt concentration.

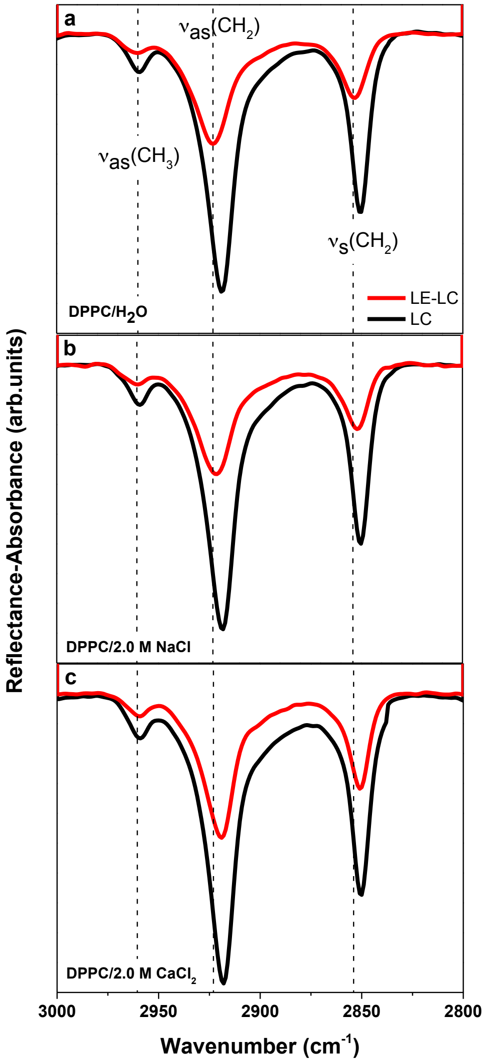

Figure 3.8. IRRAS spectra of DPPC monolayers in the LE-LC and LC phases on (a) water, (b) 2.0 M NaCl, and (c) 2.0 M $CaCl_2$ solutions. Vertical lines indicate the peak positions of CH vibrational modes of DPPC on water in the LE-LC phase. Shifts to lower wavenumbers relative to water indicate that DPPC alkyl chains are more ordered on NaCl and $CaCl_2$ solutions.

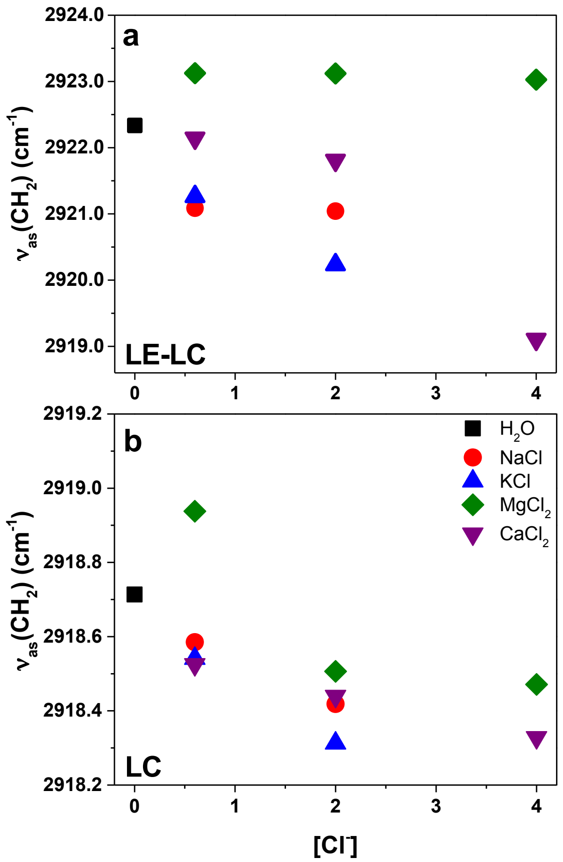

Figure 3.9. Peak position of the $\nu_{as}(CH_2)$ vibrational mode of DPPC on NaCl, KCl, $MgCl_2$, and $CaCl_2$ solutions as function of [Cl^-] in the (a) LE-LC phase (5-11 mN/m for various solutions) and (b) LC phase (40 mN/m). Wavenumber shifts of this mode correlates with the relative ordering of the alkyl chain.

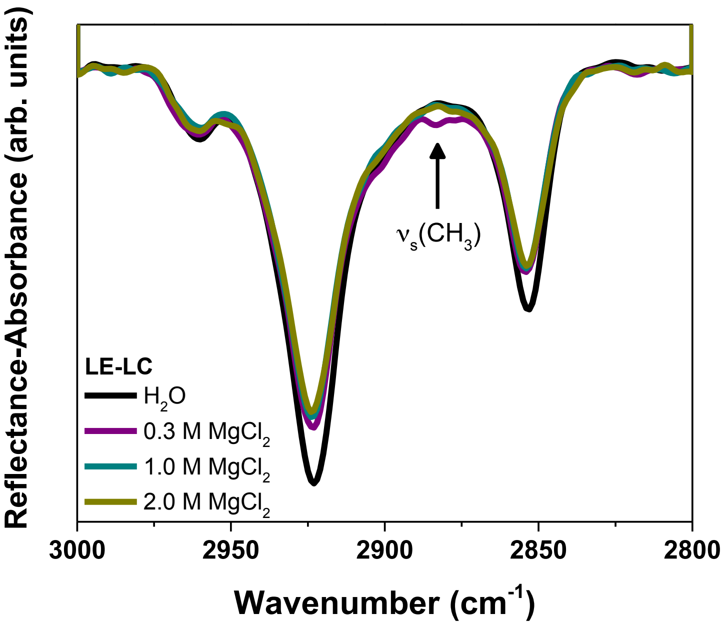

Figure 3.10. IRRAS spectra in the CH region of DPPC monolayers in the LE-LC phase (70 Å^2/molecule) on $MgCl_2$ solutions. A decrease in peak intensity is observed for all major CH modes with increasing $MgCl_2$ concentration.

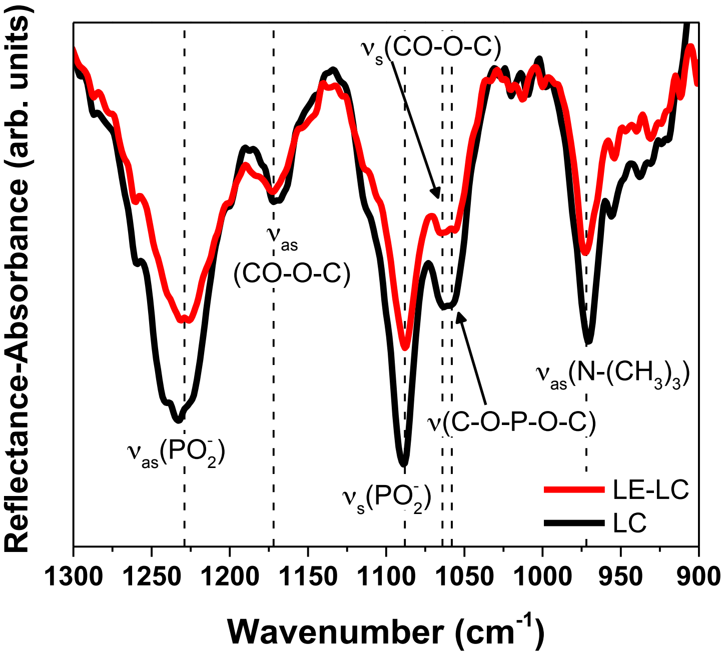

Figure 3.11. IRRAS spectra of the phosphate region of DPPC monolayers in the LE-LC and LC phases on a 2.0 M KCl solution.

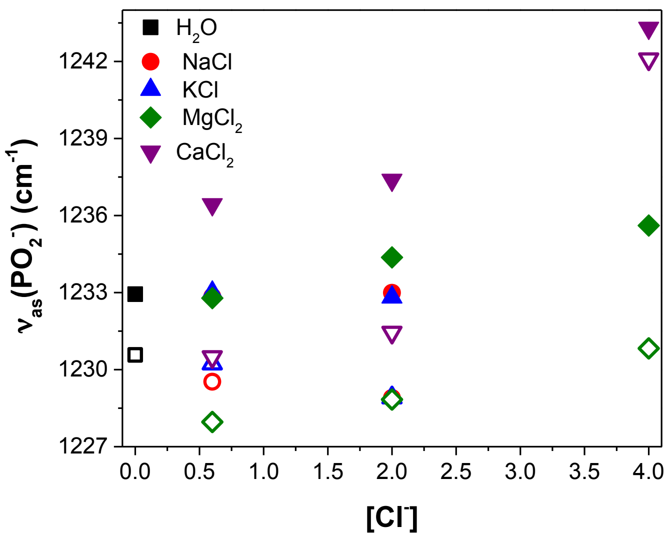

Figure 3.12. Peak position of the $\nu_{as}(PO_2^-)$ vibrational mode of DPPC monolayers on NaCl, KCl, $MgCl_2$, and $CaCl_2$ solutions as a function of [Cl^-] for the LE-LC phase (*open symbols*) and LC phase (*filled symbols*). Wavenumber shifts of this mode relates to the hydration of the phosphate group.

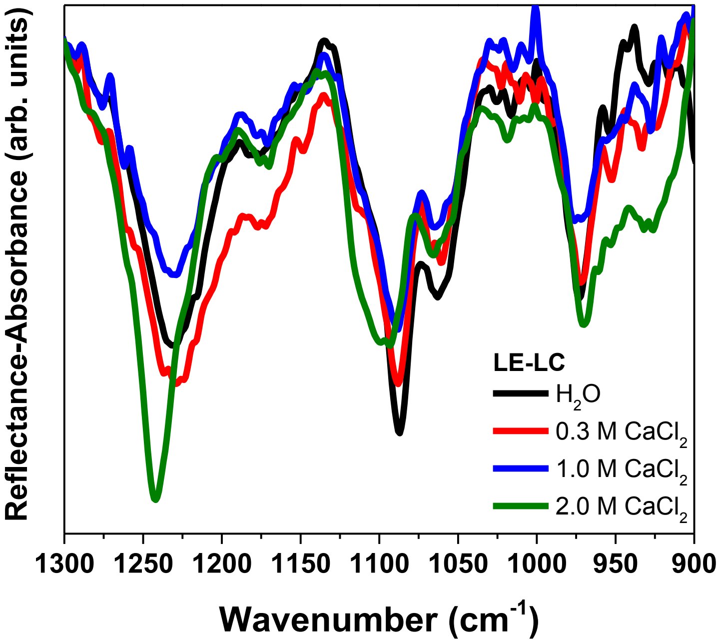

Figure 3.13. IRRAS spectra in the phosphate region of DPPC in the LE-LC phase on water and $CaCl_2$ solutions.

Table 3.1. Measured Brewster angle ($\theta_{B,\text{meas}}$) and calculated refractive index of water and aqueous salt solutions. Literature values of refractive indices obtained at 589 nm (Na D-line) is also given as comparison.

Solution	Concentration (M)	$\theta_{B,\text{meas}}$ (°)	$n_{s,\text{calc}}$	$n_{s,D}$ [78]
H_2O		53.1	1.33	1.3330
NaCl	0.6	53.1	1.33	1.3383
	2.0	53.6	1.36	1.3541
KCl	0.6	53.3	1.34	1.3384
	2.0	53.6	1.36	1.3521
$MgCl_2$	0.3	53.2	1.34	1.3406
	1.0	53.4	1.35	1.3560
	2.0	54.1	1.38	1.3749
$CaCl_2$	0.3	53.1	1.33	1.3402
	1.0	53.4	1.35	1.3575
	2.0	53.9	1.37	1.3784

Table 3.2. Number density and average domain size of DPPC domains in the LE-LC phase as determined from BAM images of DPPC on various salt solutions. Images were only analyzed for 0.6 M Cl^- solution, as distinct domains are not visually discernable at higher concentrations.

Subphase	Number density (domain × 10^{-3} /100 μm^2)	Average domain size (μm)
H_2O	81.0	31.4 ± 2.6
0.6 M NaCl	97.0	28.6 ± 4.3
0.6 M KCl	130	23.8 ± 3.6
0.3 M $MgCl_2$	227	19.2 ± 2.0
0.3 M $CaCl_2$	411	13.7 ± 4.6

Table 3.3. Calculated monolayer refractive index (n_m) of DPPC on aqueous salt solutions at $\Pi = 45$ mN/m.

Solution	Concentration (M)	n_m
H_2O		1.490
NaCl	0.6	1.488
	2.0	1.478
KCl	0.6	1.496
	2.0	1.478
$MgCl_2$	0.3	1.495
	1.0	1.486
	2.0	1.457
$CaCl_2$	0.3	1.485
	1.0	1.467
	2.0	1.457

Chapter 4: Surface Organization of a DPPC Monolayer on Concentrated $SrCl_2$ and $ZnCl_2$ Solutions

Reproduced in part with permission from Adams, E.M.; Verreault, D.; Jayarathne, T.; Cocharn, R.E.; Stone, E.A.; Allen, H.C. "Surface Organization of a DPPC Monolayer on Concentrated $SrCl_2$ and $ZnCl_2$ Solutions" *Phys. Chem. Chem. Phys*., **2016**, 18, 32345-32357. Copyright PCCP Owner Societies.

4.1. Introduction.

The oceans cover 71% of the Earth's surface and constitute a major source of naturally produced aerosols.[24] Sea spray aerosols (SSA) result from wind shearing of breaking waves, in which material at the ocean surface is ejected into the atmosphere.[8] While it is expected that chemical speciation of SSA would be representative of bulk seawater, many studies have shown that selective material transfer from the ocean to aerosols occurs,[116,26] resulting in enrichment or depletion of certain species in aerosol particles.[117,118] Enrichment or transfer of organic species has been extensively investigated,[17,18,24,119] especially during periods of biological activity.[70,21,7,23,20] During a phytoplankton bloom conducted in the laboratory, SSA generated from seawater has shown changes in the relative fractions of organic species and alkali and alkaline earth metals as a function of particle size.[23,25] Although less studied in recent years, enrichment (or depletion) of alkali and alkaline earth metals as well as transition metals relative to sodium has been observed for SSA and the sea surface microlayer (SSML), the chemically distinct thin layer (first 500 μm) at the ocean-air interface, compared to bulk seawater.[120,121,34,122,123] Interestingly, transition metals were found to be more enriched than alkali or alkaline earth metals, with enrichment factors in the range of 10–10^6.[33–35,122] It is believed that transition metals bind strongly with organic molecules, which facilitates their transfer to aerosols.[33] Recent studies of phytoplankton mesocosms support this notion, as aerosols classified as biological (Bio) or sea salt with organic carbon (SS-OC) were found to also contain Ag, Fe, and Cr.[22] Further analysis of all Ag-containing particles revealed that less than one percent of these aerosols were classified as sea salt (SS), meaning they lack signatures from organics. This suggests that transition metals are bound or strongly interact with the organic fraction in SSA.

Organic-containing aerosols are typically thought of as inverted micelles, in which an aqueous salt core is surrounded by a thin surfactant-like film.[4,6,5] Physical and optical properties of these particles, including but not limited to albedo,[12] hygroscopicity,[9] and reactivity,[10] are therefore dependent upon the interfacial properties of the organic film. The presence of ions has been shown to impact the packing density,[83,27] morphology,[66] orientation,[29] and surface potential of lipid films.[67] Transition metals typically have a more pronounced influence on lipid films due to their ability to covalently bond instead of ionically interacting with the polar headgroup region.[112] Interactions of transitions metals with lipids are ion-specific in nature, however, several studies have demonstrated that heavy metals of the same charge impact interfacial properties to different extents.[124–

[127] Yet, few studies have investigated how concentration of the transition metals impact surfactant films.[30] In the context of a marine aerosol the ion concentration becomes an important parameter since the relative concentration of ions will change as the aerosol loses or adsorbs water in the atmosphere. This will ultimately influence the organization and structure of surfactants at the interface, which in turn affects physical and optical properties of the aerosol itself.

One goal of this study is to determine how the concentration of a transition metal influences the interfacial properties of a lipid film. Dipalmitoylphosphatidylcholine (DPPC) was chosen as the lipid of interest in this study as it is abundant in the SSML[19,75] and phosphate groups (PO_3^- and PO_2^-) were identified as a signature in SSA particles containing transition metals.[22] Although zinc (Zn^{2+}) is known to be a trace element (on average 6 nM)[31] in bulk seawater, it has been determined to be highly enriched in aerosols,[33,34] and was therefore chosen as the model transition metal ion here. It's influence on the phase behavior of DPPC is compared to that of strontium (Sr^{2+}), an alkaline earth metal one thousand times more abundant in seawater which has little or no enrichment in aerosols.[33,120] Concentrations used here varied from 0.3-2.0 M. While these concentrations exceed those in oceanic conditions they are meant to represent an aqueous phase aerosol in varying stages of hydration in which ions are enriched. Surface pressure-area isotherms and Brewster angle microscopy (BAM) were conducted to investigate the phase behavior and corresponding surface morphology of DPPC on aqueous salt solutions. Alkyl chain ordering and phosphate headgroup-ion interactions were probed with infrared reflection-absorption spectroscopy (IRRAS) and vibrational sum frequency generation (VSFG) spectroscopy. Results reported here indicate that Zn^{2+} strongly interacts with DPPC molecules and subsequently alter monolayer properties in a concentration-dependent manner. Interaction between DPPC and Sr^{2+} is significantly weaker than Zn^{2+}, but Sr^{2+} also induces changes to the interfacial properties of the DPPC film.

4.2. Experimental.

4.2.1. Materials.

1,2-Dipalmitoyl-*sn*-glycero-3-phosphocholine (DPPC) (> 99%, Avanti Polar Lipids, United States) was used as received. A 1 mM DPPC solution was prepared by dissolution in chloroform (Fisher Scientific, United States). Strontium chloride ($SrCl_2 \cdot 6H_2O$) (> 99%, ACS certified, MP Biomedicals, United States) and zinc chloride ($ZnCl_2$) (> 98%, Acros Organics, United States) were dissolved in ultrapure water with a resistivity 18.2 MΩ·cm (Barnstead Nanopure Filtration System, model D4741, Barnstead/Thermolyne Corporation, United States) and a measured pH of 5.6. Stock salt solutions were purified of trace organic impurities by previously described methods.[69] Vibrational sum frequency spectra were collected in the CH region (2800-3000 cm^{-1}) to verify the lack of organic impurities in the stock solutions. Mohr titration was used to establish concentration of the stock solutions after purification.[76] Solutions of desired concentrations were then prepared by dilution of the stock solutions. For $ZnCl_2$ solutions a few drops of HCl (trace metal grade, Fisher Scientific) was added to prevent formation of $Zn(OH)_2$ species, resulting in a final pH of 4.8. A minimum period of 12 h was allowed for solutions to equilibrate to room temperature before experiments were performed. All experiments were conducted at ambient temperature (298 ± 1 K) and pressure.

4.2.2 Methods.

Surface pressure–area isotherms

Surface pressure–area (Π–A) isotherms were measured on a Teflon Langmuir trough (KSV Minitrough, KSV NIMA, Finland) with an area of 144 cm^2. Prior to each experiment the trough and barriers were thoroughly rinsed with ethanol and ultrapure water several times. The trough was then filled with the desired aqueous solution. The presence of impurities in the subphase was monitored by compressing the barriers to ensure that no significant rise in surface pressure (> 0.2 mN/m) was observed. DPPC monolayers were prepared by dropwise spreading of an appropriate volume of the lipid solution with a microsyringe (Hamilton, United States). Ten minutes were allowed for chloroform evaporation. Monolayers were symmetrically compressed at a constant rate of 5 mm/min/barrier until a surface pressure of 55 mN/m was reached. All isotherms were repeated at least three times to ensure reproducibility. Measured mean molecular areas (MMA) and surface pressures had experimental errors of ± 1 $Å^2$/molecule and ± 0.5 mN/m, respectively.

Brewster angle microscopy

Imaging of the DPPC monolayers was done simultaneously with Π–A isotherms on a custom-built BAM setup that has been previously described.[66] The BAM setup was detailed in Chapter 2. The incident angle was adjusted to the Brewster angle for each aqueous solution (Table 4.1) to obtain a background with a gray level ≤ 30. Images were collected during monolayer compression at a rate of 4.85 s per frame to create a movie. Still frames were then extracted at appropriate mean molecular areas or surface pressures. Final images have been cropped from the original 800 × 800 μm^2 size to show the most resolved region of the image, which may differ from image to image. Scale bars are accurate for each individual image.

Infrared reflection-absorption spectroscopy

Spectra were collected with an FTIR spectrometer (Spectrum 100, Perkin Elmer, United States) equipped with an HgCdTe (MCT) detector. The Langmuir KSV Minitrough was placed in the FTIR chamber on a breadboard, where two planar gold mirrors were mounted to direct light to and collect light from the sample surface. The first gold mirror was placed such that the IR beam was most focused at the sample surface and had an incident angle of 46°. All measurements were obtained in single beam mode, with a single beam spectrum on the respective bare solution used as the background. Reflectance-absorbance was determined from RA = $-\log(R_m/R_0)$, where R_0 and R_m are the reflectances of the bare and monolayer-covered solutions, respectively. Spectra were collected over the range 450–4000 cm^{-1} and averaged for 300 scans at a resolution of 4 cm^{-1}. Baseline correction of spectra was done in OriginPro 9.0 (OriginLab, United States), where a third-order polynomial was fitted in the region of interest. All spectra shown here are averaged from at least two baseline-corrected spectra.

Vibrational sum frequency generation spectroscopy

Measurement of VSFG spectra was done with a visible (VIS)-infrared (IR) broad bandwidth SFG spectrometer system. The BBSFG-1 system was detailed in Chapter 2. A co-propagating geometry was used in this setup, where the VIS and IR beams had incident angles of 53° and 68° from surface normal, respectively. Energy of the VIS and IR pulses in the CH stretching region was 70 and 14 μJ, respectively. The SFG beam in the reflection direction was recollimated and focused to the slit of the spectrometer (Spectra Pro-500i, Princeton Instruments, United States) and detected by a LN_2-cooled CCD (Spec-10:400B, 1340×400 pixels, Princeton Instruments). The full CCD chip was used to collect the SFG signal but a cosmic correct function was selected in the spectrometer software (SpectraSense 5.0) to remove cosmic radiation spikes. Spectra were collected for 2 min in *ssp* (*s*-SFG, *s*-VIS, *p*-IR) and *ppp* polarization combinations. Final spectra shown here were background-subtracted and normalized to the non-resonant SFG profile of a GaAs(110) crystal (Lambda Research Optics, United States). Intensities are directly comparable between spectra. Peak positions in the VSFG spectra were calibrated by comparison of the non-resonant absorption spectrum from a polystyrene film to those collected with an FTIR spectrometer.

VSFG orientational analysis

Orientation of the molecular group correlates to the nonlinear susceptibility elements given in Eq. (2.18)-(2.21) and depends on the point group symmetry and whether the stretching feature is asymmetric or symmetric in nature. For the methyl groups ($-CH_3$) which have C_{3v} symmetry, if one assumes a rotationally isotropic surface, the symmetric stretch in *ssp* and the asymmetric stretch in *ppp* polarizations were used here for orientation analysis. The corresponding $\chi^{(2)}$ elements can be expressed as

$$\chi^{(2)}_{yyz,ss} = \frac{1}{2} N_s\beta_{ccc}\left[(1+R)\langle\cos\theta_{\mathrm{CH_3}}\rangle - (1-R)\langle\cos^3\theta_{\mathrm{CH_3}}\rangle\right] \tag{4.1}$$

$$\chi^{(2)}_{yyz,as} = \chi^{(2)}_{xxz,as} = -N_s\beta_{aca}\left(\langle\cos\theta_{\mathrm{CH_3}}\rangle - \langle\cos^3\theta_{\mathrm{CH_3}}\rangle\right) \tag{4.2}$$

$$\chi^{(2)}_{yzy,as} = \chi^{(2)}_{xzx,as} = \chi^{(2)}_{zxx,as} = \chi^{(2)}_{zyy,as} = N_s\beta_{aca}\langle\cos^3\theta_{\mathrm{CH_3}}\rangle \tag{4.3}$$

$$\chi^{(2)}_{zzz,as} = 2N_s\beta_{aca}\left(\langle\cos\theta_{\mathrm{CH_3}}\rangle - \langle\cos^3\theta_{\mathrm{CH_3}}\rangle\right) \tag{4.4}$$

where R is the hyperpolarizability ratio defined as $R = \beta_{aac}/\beta_{ccc}$, and $\theta_{\mathrm{CH_3}}$ is the average tilt angle of the methyl group from the surface normal. A variety of values for R have been reported in literature with most near $R = 2$.[62] Here it was assumed that $R = 2.3$ and $\beta_{aca}/\beta_{aac} = 4.2$.[63,64] Assuming the orientation distribution is a δ-function, $\theta_{\mathrm{CH_3}}$ can be determined from the ratio $\chi^{(2)}_{ppp,as}/\chi^{(2)}_{ssp,ss}$.

4.3. Results and Discussion

4.3.1. Impact of Sr^{2+} and Zn^{2+}ions on DPPC phase behavior

Π–*A* isotherms of DPPC on $SrCl_2$ solutions are shown in Figure 4.1a. An isotherm of DPPC on water is also given for reference. In the case of water, four DPPC phases are observed with decreasing MMA: gas (G, > 96 Å^2/molecule); liquid-expanded (LE, 75-96 Å^2/molecule); LE–liquid-condensed (LC) coexistence region (LE-LC, 55-75 Å^2/molecule); and LC (< 55 Å^2/molecule). DPPC exhibits similar phase behavior on $SrCl_2$ solutions as on water, regardless of Sr^{2+} concentration, as all respective phases are observed. It can be seen, however, that the monolayer is slightly expanded in the LE and LE-LC phases relative to water. At low surface pressures (< 10 mN/m), the increase in

MMA is concentration-dependent, as the change in area (ΔA) relative to water increases with increasing Sr^{2+} concentration (Figure 4.1b). As the monolayer is compressed to higher surface pressures (> 20 mN/m), the monolayer recovers MMAs similar to that of DPPC on water, indicating that Sr^{2+} ions are squeezed out of the monolayer. Results presented here are consistent with studies of negatively charged dimyristoylphosphatidylglycerol (DMPG) monolayers on $SrCl_2$ aqueous solutions, where an expansion of the monolayer occurred in the LE phase, but no change relative to water was observed in the LC phase.[128]

Squeezing out of Sr^{2+} ions occurs at all concentrations investigated, which indicates that Sr^{2+} ions weakly interact with DPPC molecules. The area increases in the LC phase (40 mN/m) are less than 1 $Å^2$/molecule, i.e., within the error of measurements. Similar behavior was observed for monovalent ions (Na^+ and K^+), where an expansion of 2 $Å^2$/molecule was observed for 2.0 M solutions in the LC phase.[68] The negligible expansion observed for Sr^{2+} suggests that it does not significantly interact with DPPC, and that its binding interaction is similar to that of monovalent ions.

The phase behavior of DPPC on $ZnCl_2$ solutions (Figure 4.2a) is very different from that on $SrCl_2$. These differences are not due to the lower pH of $ZnCl_2$ solutions (4.8 vs. 5.6), as previous studies have demonstrated that the phase behavior of DPPC is not impacted by changes in pH in this range.[129] On 0.3 M $ZnCl_2$ an increase in surface pressure is not observed until 56 $Å^2$/molecule. This can be attributed to a transition from a G-LC coexistence region (as evidenced below by BAM) to an LC phase. The monolayer remains in the LC phase until compression is stopped, where molecules occupy a smaller MMA relative to water. The area decrease (Figure 4.2b) observed at all surface pressures indicates that Zn^{2+} has a condensing effect on the DPPC monolayer. Dimyristoylphosphatidylcholine (DMPC), a shorter chain analog of DPPC, displays similar phase behavior on $ZnCl_2$ solutions at ambient temperature; a significant (~20 Å^2/molecule) decrease in the MMA at the transition to the LC phase relative to water was observed.[30] The condensing effect appears to have some concentration dependency, as larger area decreases are observed for 1.0 M $ZnCl_2$ relative to 0.3 and 2.0 M. It should also be noted that for the 1.0 M solution there is a phase transition just below 10 mN/m, indicated by the change in slope of the isotherm at this point. This is likely due to a change in the orientation of the alkyl chains. Similarly, a phase transition is observed on 2.0 M $ZnCl_2$, but does not occur until 30 mN/m. The phase behavior of DPPC on the 2.0 M solution appears to be unique compared to the other concentrations. While condensed relative to water, the G-LC to LC phase transition occurs at a higher MMA (68 Å^2/molecule) than the other $ZnCl_2$ solutions. Between 10-30 mN/m the monolayer is expanded compared to water, but occupies a smaller MMA at surface pressures higher than 30 mN/m. The expansion of the monolayer on 2.0 M $ZnCl_2$ relative to other concentrations may be due to the positively charged choline group, which causes increased electrostatic repulsions between lipid molecules in the interfacial region.[128]

Π–A isotherms indicate that the phase behavior of DPPC is different in the presence of Sr^{2+} vs. Zn^{2+}, which suggests that the rigidity of the monolayer also differs. The isothermal compressibility modulus ($C_s^{-1} = -A_\Pi(\partial\Pi/\partial A_\Pi)_T$, where A_Π is the molecular area at the corresponding Π), is a measure of a monolayer's rigidity; a higher value of C_s^{-1}

corresponds to a more rigid monolayer. The compressibility modulus of DPPC on $SrCl_2$ and $ZnCl_2$ (Figure 4.3) were obtained from the slopes of isotherms shown in Figures 4.1a and 4.2a. The compressibility modulus of DPPC on water is shown for reference. In the case of $SrCl_2$ solutions, the monolayer has similar compressibility as on water, where an increase to ~25 mN/m is observed at low surface pressures followed by a drop back to 0 mN/m at Π =10 mN/m, signifying the point at which the LE-LC coexistence phase occurs. Upon compression to higher surface pressures, the monolayer has a maximum compressibility modulus near Π = 40 mN/m, where after this point the compressibility modulus decreases as the monolayer approaches collapse. The maximum C_s^{-1} values observed for 0.3 and 1.0 M $SrCl_2$ solutions are ~50 mN/m less than that of water, indicating that the monolayer has become more fluid. For 2.0 M though, the maximum value is similar to water, but the surface pressure at which this occurs has shifted to a higher value ($\Pi \approx$ 55 mN/m). This suggests that the stability of the DPPC monolayer is increased in the presence of 2.0 M $SrCl_2$ relative to water.

The compressibility modulus of DPPC on $ZnCl_2$ solutions is different than that on $SrCl_2$ solutions. For 0.3 M and 1.0 M $ZnCl_2$ solutions the compressibility modulus increases with increasing surface pressure until a maximum is reached near Π = 55 mN/m. In the case of 2.0 M $ZnCl_2$, the compressibility modulus plateaus at 75 mN/m in the range Π = 10–30 mN/m, and then increases until compression was stopped. The lack of a compressibility maximum suggests that the stability of the monolayer is greatly enhanced at this concentration. In general, Zn^{2+} ions increase the stability of the DPPC monolayer, as the surface pressure at which the maximum compressibility occurred increased. However, the rigidity of the monolayer is not significantly impacted (except in the case of 2.0 M) as the same maximum values were reached.

4.3.2. Ion Effects on DPPC domains morphology

Figure 4.4 shows BAM images of DPPC on $SrCl_2$ solutions in the LE-LC coexistence region and LC phase. In all images shown, dark blue is representative of water-rich or lipid-poor regions while bright blue indicate lipid-rich regions. For the 0.3 M solution, round LC domains form in the LE-LC phase. Domains are on average 15 μm in size, which is approximately half the size observed for DPPC on water.[104] A decrease in domain size has also been observed in the presence of other alkaline earth cations.[68,84] It is likely that the decreased size stems from increased van der Waals interactions between the alkyl chains. Round domain shapes, compared to multi-lobed shapes observed on water,[104,105] indicate that line tension (van der Waals forces) is the dominant interaction between lipid molecules in the LC domains.[108] At higher Sr^{2+} ion concentrations LC domains are not observed in the LE-LC phase. An inhomogeneous film with decreased reflectance forms in the case of 1.0 M, while a dark image consistent with a G or LE phase is observed for 2.0 M $SrCl_2$. Similarly, the reflectance from the monolayer decreases with increasing Sr^{2+} concentration in LC phase.

BAM images of DPPC on $ZnCl_2$ solutions, shown in Figure 4.5, reveal that condensed lipid sheets exist at 0 mN/m for all Zn^{2+} concentrations investigated. It should be noted that lipid domain sheets were observed immediately after spreading, prior to any compression of the DPPC monolayer, and indicate that a coexistence of the G and LC phases occurs. The presence of lipid domains at a surface pressure of 0 mN/m indicates that Zn^{2+} ions strongly interact with the PC headgroup, likely through the formation of covalent bonds to the phosphate moiety.[112,130] At higher surface pressures condensed film morphology persists for all $ZnCl_2$ concentrations, as can be seen in the LC phase at 45 mN/m. A decrease in intensity of the reflected light with increasing concentration is also observed for Zn^{2+}, but the effect is less pronounced than that of $SrCl_2$ solutions.

Assuming the monolayer refractive index (n_m = 1.49) does not significantly change in the presence of the divalent cations, the relative monolayer thickness (d) can be determined from the relationship:[50]

$$d = \frac{\lambda\sqrt{R_p}}{\pi \sin\left(2\theta_B - 90\right)} \frac{n_m^2(n_a^2 - n_s^2)}{\sqrt{n_a^2 + n_s^2}(n_a^2 - n_m^2)(n_s^2 - n_m^2)} \tag{4.5}$$

where λ is the laser wavelength, R_p is the p-polarized reflectance, n_a and n_s are the refractive indices of air and of the solution, respectively, and θ_B is the Brewster angle (Table 4.1). DPPC is known to have a thickness of 1.6 nm in the LC phase on water,[131,132] which corresponds to the thickness of the alkyl chains.[133] Results shown in Figure 4.6a indicate that the monolayer thickness is not significantly impacted by Sr^{2+} ions. This is consistent with Π–A isotherms, which showed that Sr^{2+} ions were squeezed out of the monolayer at high surface pressures. Zn^{2+} ions, however, increase the relative thickness (Figure 4.6b) of the DPPC film. For 0.3 M $ZnCl_2$ the monolayer thickness at 0 mN/m is comparable to the LC phase on water. With increasing surface pressure, the thickness increases to a maximum value of 2.4 nm. The thickness of the DPPC monolayer is dependent on the concentration of Zn^{2+} ions in solution, as the monolayer becomes thicker with higher concentrations of Zn^{2+}. If it is assumed that the alkyl chain has a completely *trans* configuration, the length of the chain should be 1.9 nm.[131,134] As the thickness measured in the LC phase for all $ZnCl_2$ solutions is greater than that of a completely *trans* alkyl chain oriented perpendicular to the surface plane, it is possible that a portion of the hydrophilic moieties, likely the carbonyl group, has become dehydrated and thus contributes to the observed thickness. Dehydration of the monolayer may be indicative to direct binding of Zn^{2+} to DPPC molecules, which removes solvating water molecules.

4.3.3. Ion Effects on DPPC Alkyl Chain Packing, Conformation and Orientation

The 2-D lattice packing structure and conformation (*trans* vs. *gauche*) of the DPPC alkyl chains can be determined from IRRAS spectra. Figure 4.7 shows IRRAS spectra of the CH_2 scissoring ($\delta(CH_2)$) mode at 1469 cm^{-1} in the LC phase (40 mN/m) in the presence of Sr^{2+} and Zn^{2+} ions. One peak is observed at all concentrations for both ions, indicative of a hexagonal or triclinic lattice structure.[57] This suggests that Sr^{2+} and Zn^{2+} ions do not alter the 2-D lattice structure of the monolayer relative to a pure water subphase.

IRRAS spectra of DPPC on 0.3 M salt solutions in the LE-LC phase (G-LC phase for Zn^{2+}) are shown in Figure 4.8a for the CH stretching region (2800–3000 cm^{-1}). Four peaks are observed, arising from methylene (CH_2) and methyl (CH_3) vibrational modes, namely the CH_3 asymmetric ($\nu_{as}(CH_3)$), CH_2 asymmetric ($\nu_{as}(CH_2)$), CH_3 symmetric ($\nu_s(CH_3)$), and CH_2 symmetric ($\nu_s(CH_2)$) stretching modes at 2963, 2922, 2883, and 2850 cm^{-1}, respectively. The peak positions of the CH_2 vibrational modes are sensitive to the conformation of the alkyl chains, with *gauche* defects causing the peaks to occur at higher wavenumbers, while *trans* bonds appear at lower wavenumbers. As can be seen in Figure 4.8a, the peak positions of the CH_2 bands are shifted to lower wavenumbers for the Zn^{2+} solution, while Sr^{2+} has a negligible change in the peak position compared to water. This trend was similarly observed for all concentrations investigated, shown in Figure 4.8b, where the peak position of the $\nu_{as}(CH_2)$ vibrational mode is plotted as a function of ion concentration. At low surface pressures (open symbols, Zn^{2+}: 0 mN/m, Sr^{2+}: 6–9 mN/m), Zn^{2+} has a significant shift (~3 cm^{-1}) to lower wavenumbers. Sr^{2+}, however, has negligible shifts (≤ 1 cm^{-1}), except in the case of the 0.3 M solution. In the condensed phase (solid symbols, 40 mN/m), peak shifts relative to DPPC on water are small (≤ 1 cm^{-1}), which indicates that ordering of the chain is not significantly different in the presence of these ions. These results indicate that Zn^{2+} ions cause the alkyl chain to increase conformational order (*trans* bonds) at low surface pressures, and that this ordering is not significantly impacted by increasing surface pressure. FTIR studies of unsaturated palmitoyloleylphosphatidylcholine (POPC) vesicles had similar results, in which alkyl chains did not undergo the phase transition from the more ordered gel state to the disordered liquid-crystalline state, but remained in the gel state upon binding to Zn^{2+} ions.[109,130] Sr^{2+}, however, induces conformational disorder (*gauche* defects) in the chain at low surface pressures for the 0.3 M solution, evidenced by the appearance of the $\nu_s(CH_3)$ mode. For higher surface pressures, Sr^{2+} had no effect on peak position, indicating that it does not interact with the lipid, consistent with Π–A isotherms that showed Sr^{2+} was squeezed out of the monolayer at these pressures. In contrast, Zn^{2+}

causes shifts to lower wavenumbers, which suggests that it increases conformational order in the LC phase as well.

Figure 4.9 shows VSFG spectra in *ssp* and *ppp* polarizations of the CH stretching regions for DPPC monolayers on 2.0 M $SrCl_2$ and $ZnCl_2$ solutions. In *ssp* polarization four peaks are observed corresponding to the $\nu_s(CH_2)$ at 2846 cm^{-1}, $\nu_s(CH_3)$ at 2872 cm^{-1}, $\nu_{as}(CH_2)$ at 2914 cm^{-1}, and a Fermi resonance of the CH_3 group ($\nu_{FR}(CH_3)$) at 2935 cm^{-1}. Although weaker, the $\nu_s(CH_2)$, $\nu_s(CH_3)$, and $\nu_{as}(CH_2)$ modes are also observed in *ppp* polarization, along with the $\nu_{as}(CH_3)$ mode at 2955 cm^{-1}. At low surface pressures (9 mN/m for Sr^{2+} and 0 mN/m for Zn^{2+}) in the *ssp* spectra, the $\nu_s(CH_2)$ mode is more intense than the $\nu_s(CH_3)$. In the LC phase (40 mN/m) the $\nu_s(CH_3)$ peak becomes significantly more intense. Based on the electric dipole approximation, SFG does not occur when the environment is centrosymmetric. A nearly *trans* alkyl chain possesses centrosymmetric CH_2 groups, which should give rise to a weak SFG signal. Relative ordering of the alkyl chain can therefore be determined from the intensity ratio $I(\nu_s(CH_3))/I(\nu_s(CH_2))$, with a higher value corresponding to an alkyl chain with more *trans* bonds. Intensity ratios for DPPC on $SrCl_2$ and $ZnCl_2$ solutions are presented in Table 4.2. It can be seen that at low surface pressures, the ratio value is small, consistent with an alkyl chain having considerable *gauche* defects. For Zn^{2+}, a ratio could only be determined for the 2.0 M solution, as the 0.3 and 1.0 M solutions had no SFG response in the CH region. The ratio is comparable in magnitude to water and $SrCl_2$ solutions, which would suggest the alkyl chains have some *gauche* defects at 0 mN/m. This result contradicts IRRAS data discussed earlier that showed Zn^{2+} ions significantly increase the alkyl chain ordering at 0 mN/m. Observed differences may be due to the high intensity of the SFG input beams or the sampling spot size; in IRRAS measurements the diameter of the focused beam is 10 mm, while in SFG measurements the beam spot size is ~100 μm (assuming a purely Gaussian beam).[135] Intensity ratios in the LC phase are similar between the Sr^{2+} and Zn^{2+} solutions, indicating ordering of the alkyl chains is not significantly different at high surface pressures for the two ions, which is consistent with IRRAS measurements done here.

Orientation of the terminal methyl groups (θ_{CH3}) relative to surface normal can be determined from SFG measurements based on the relationship $\sqrt{I_{ppp}(\nu_{as}(CH_3))/I_{ssp}(\nu_s(CH_3))} = \chi_{ppp}/\chi_{ssp}$. Furthermore, because the DPPC alkyl chain has a nearly *trans* conformation in the LC phase, the chain tilt angle (θ_t) can be determined from the relation $\theta_t = 41.5° - \theta_{CH3}$.[73] Calculated values of θ_{CH3} and θ_t are provided in Table 4.2. The tilt chain angle for DPPC on water was found to be 22.7°, consistent with previous studies.[73,132,133] The average alkyl chain tilt angle did not vary significantly ($\leq 2°$) with either Sr^{2+} or Zn^{2+} ions, revealing that they do not impact DPPC's alkyl chain orientation in the condensed phase. These results suggest that the increased monolayer thickness observed from BAM measurements for $ZnCl_2$ solutions does not stem from changes in the alkyl chain ordering or orientation, but rather comes from dehydration of the carbonyl or phosphatidylcholine moieties as a consequence of direct binding of Zn^{2+} with DPPC molecules.

4.3.4. Interaction of Sr^{2+} and Zn^{2+} ions with carbonyl groups

IRRAS spectra of the carbonyl stretching mode (ν(C=O)) in the presence of Sr^{2+} and Zn^{2+} ions (LC phase, 40 mN/m) are shown in Figure 4.10. The negative feature at ~1735 cm^{-1} corresponds to ν(C=O), while the positive feature below 1700 cm^{-1} arises from anomalous dispersion of water. In the presence of Sr^{2+} the peak remains at 1735 cm^{-1}, but a ~5 cm^{-1} shift to higher wavenumbers is observed for Zn^{2+}. The shift reflects dehydration of the carbonyl groups[136] and is consistent with previous studies that found that transition metals like Cu^{2+} and Zn^{2+} induced dehydration of phospholipid carbonyl groups.[109,130] The shift observed here is independent of the Zn^{2+} concentration, which indicates that the solvation shell of the carbonyl group is already removed at the lowest concentration studied here. Dehydration of the carbonyl groups is likely achieved through direct interaction with Zn^{2+} ions, in which Zn^{2+} achieves its favored tetrahedral coordination[134] through interaction with both the carbonyl and phosphate groups. As discussed earlier, dehydration of the carbonyl group likely contributes to the increased monolayer thickness determined from BAM images.

4.3.5. Binding Interaction of Sr^{2+} and Zn^{2+} to phosphatidylcholine headgroup

Figure 4.11 shows IRRAS spectra of the phosphate region (900–1300 cm^{-1}) for DPPC monolayers on 2.0 M $SrCl_2$ and $ZnCl_2$ solutions. Several peaks are observed in the region, with the asymmetric and symmetric PO_2^- stretching($\nu_{as}(PO_2^-)$ and $\nu_s(PO_2^-)$) modes occurring at 1230 cm^{-1} and 1088 cm^{-1}, respectively. The asymmetric and symmetric CO-O-C stretching (ν_{as}(CO-O-C) and ν_s(CO-O-C)) modes are observed at 1168 cm^{-1} and 1065 cm^{-1}, respectively, whereas while the shoulder at 1057 cm^{-1}

corresponds the C-O-P-O-C stretching (ν(C-O-P-O-C)) mode.[112] The peak at 971 cm^{-1} is attributed to the asymmetric C-N stretch ($\nu_{as}(N\text{-}(CH_3)_3)$) of the choline group.[111]

For both the 2.0 M $SrCl_2$ and $ZnCl_2$ solutions it can be seen that the $\nu_{as}(PO_2^-)$ mode shifts to a higher wavenumber going from the LE-LC or G-LC phase to the LC phase, consistent with the partial removal of the phosphate solvation shell as DPPC molecules are packed closer together. The peak position of the $\nu_{as}(PO_2^-)$ mode, shown in Figure 4.11c, can therefore be used to assess the hydration state of the PC headgroup. In the case of $SrCl_2$, the peak shifts to lower wavenumbers in the LE-LC phase with increasing concentration, indicative of increased hydration. In the LC phase however, the mode has a similar value to water, suggesting that the Sr^{2+} ions have little or no interaction with the phosphate moiety, even when ions are highly concentrated. Sr^{2+} has a smaller surface charge density compared to Ca^{2+} (ionic radii Sr^{2+}: 113 pm; Ca^{2+}: 100 pm),[137] but MD simulations have determined that the binding affinity of Sr^{2+} to a DPPC bilayer is similar to Ca^{2+}.[90] Results here, however, indicate that Sr^{2+} acts like a monovalent ion, as Na^+ and K^+ displayed similar behavior in other IRRAS studies.[68,112] This behavior cannot be explained by surface charge density, as the surface charge density of Sr^{2+} is approximately two times that of Na^+ (ionic radius 102 pm).[137]

For $ZnCl_2$ solutions the peak position of the $\nu_{as}(PO_2^-)$ mode significantly shifts (> 10 cm^{-1} relative to water) to lower wavenumbers. There is little difference in the peak position between the G-LC and LC phases, which points to formation of Zn^{2+}-PC complexes rather than increased hydration of the phosphate group. Furthermore, the peak continues to redshift with increasing Zn^{2+} concentration; increased hydration when less water molecules are available seems unlikely. X-ray reflectivity and FTIR studies have found dehydration of PC films and vesicles to occur upon binding of Zn^{2+} ions.[130,134] IRRAS spectra of dipalmitoylphosphatidylglycerol (DPPG) have also shown a ~10 cm^{-1} red shift in the presence of Zn^{2+} and Cu^{2+} ions,[112] which suggests that the *d*-orbitals of transition metals play a role in the observed change in peak position.

It should also be noted that the red shift of the $\nu_{as}(PO_2^-)$ mode in the presence of Zn^{2+} is accompanied by a blue shift of the $\nu_s(PO_2^-)$ mode (Figure 4.12). This was similarly observed in spectroscopic studies by Binder and co-workers.[109,130] Studies of carboxylic acids have shown that the wavenumber difference ($\Delta\bar{\nu}$) between the asymmetric and symmetric stretching modes of the COO^- group decreases when the cation interacts with lipids in a bridging or bidentate manner.[138] As DPPC molecules occupy a smaller MMA on $ZnCl_2$ solutions in the LC phase and dehydration of the carbonyl groups was observed, it is likely that Zn^{2+} ions form a 2:1 bridging complex, where Zn^{2+} interacts with free oxygens of the phosphate and the oxygen of the carbonyl group of two neighboring lipids. The $\Delta\bar{\nu}$ between the $\nu_{as}(PO_2^-)$ and $\nu_{as}(PO_2^-)$ modes decreases with increasing concentration (134 cm^{-1} for 0.3 M vs. 120 cm^{-1} for 2.0 M). As $\Delta\bar{\nu}$ is smaller for higher concentrations, this suggests that the interaction of Zn^{2+} with DPPC is stronger when less water is available. Furthermore, since $\Delta\bar{\nu}$ changes with concentration, this indicates that solvation of this complex influences the strength of the interaction.

4.4. Conclusions

Studies of marine aerosols have indicated that Sr^{2+} ions are not enriched in aerosols while Zn^{2+} ions are significantly enriched,[34,122,33] despite both ions having the same charge. Investigation into the binding affinity of these ions to the naturally occurring phospholipid DPPC suggests that enrichment of Sr^{2+} ions does not occur because Sr^{2+} has little or no interaction with the lipid molecules, even when ions are highly concentrated. Monolayer properties are only impacted by Sr^{2+} ions at low lipid coverage. Sr^{2+} behaves similarly to monovalent ions despite having twice the surface charge density. Zn^{2+}, on the other hand, strongly interacts with DPPC, and stabilizes the monolayer by inducing conformational order at low lipid coverage. BAM images and IRRAS spectra demonstrate that the DPPC monolayer is more hydrophobic in the presence of Zn^{2+}. IRRAS spectra also reveal that the binding of Zn^{2+} is concentration-dependent even in this highly concentrated regime. Such behavior may indicate that changes in the PC headgroup solvation or orientation occur. Probing of the interfacial water hydrogen-bonding network near DPPC monolayers on $SrCl_2$ and $ZnCl_2$ salt solutions by VSFG spectroscopy as well as MD simulations of the Zn^{2+}-PC complex could give some insight into the solvation structure and binding mechanism of Zn^{2+} to the DPPC molecule. Furthermore, experimental systems generating aerosols via bubble bursting using simple solutions (e.g., DPPC with Zn^{2+} or Sr^{2+}) are crucial in evaluating the interplay between selective lipid-ion binding and enrichment in aerosols. Combining such studies with the findings in this work and theoretical simulation will help explain the selective enrichment observed in SSA during phytoplankton blooms. Regardless, results obtained here show Zn^{2+} strongly interacts with the PC headgroup, which could explain why this ion is enriched in marine aerosols.

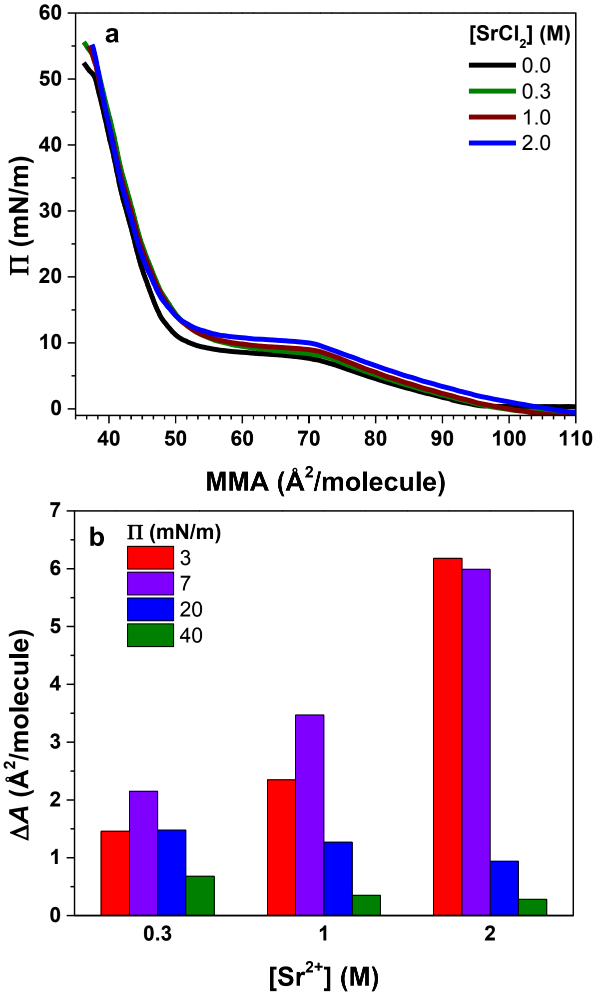

Figure 4.1. (a) Π–*A* isotherms of DPPC monolayers on $SrCl_2$ solutions. An isotherm of DPPC on water is shown for reference. (b) Variation of DPPC mean molecular area (MMA) on $SrCl_2$ solutions relative to water for different surface pressures.

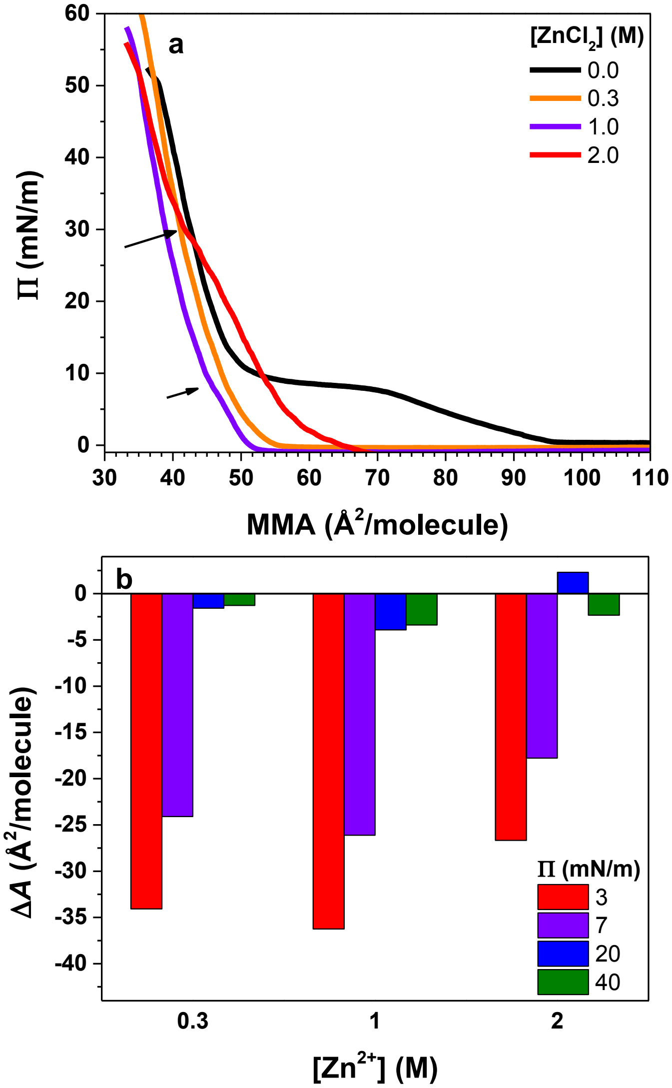

Figure 4.2. (a) Π–*A* isotherms of DPPC monolayers on $ZnCl_2$ solutions. An isotherm of DPPC on water is shown for reference. Arrows indicate phase transitions. (b) Variation of DPPC MMA on $ZnCl_2$ solutions relative to water at different surface pressures.

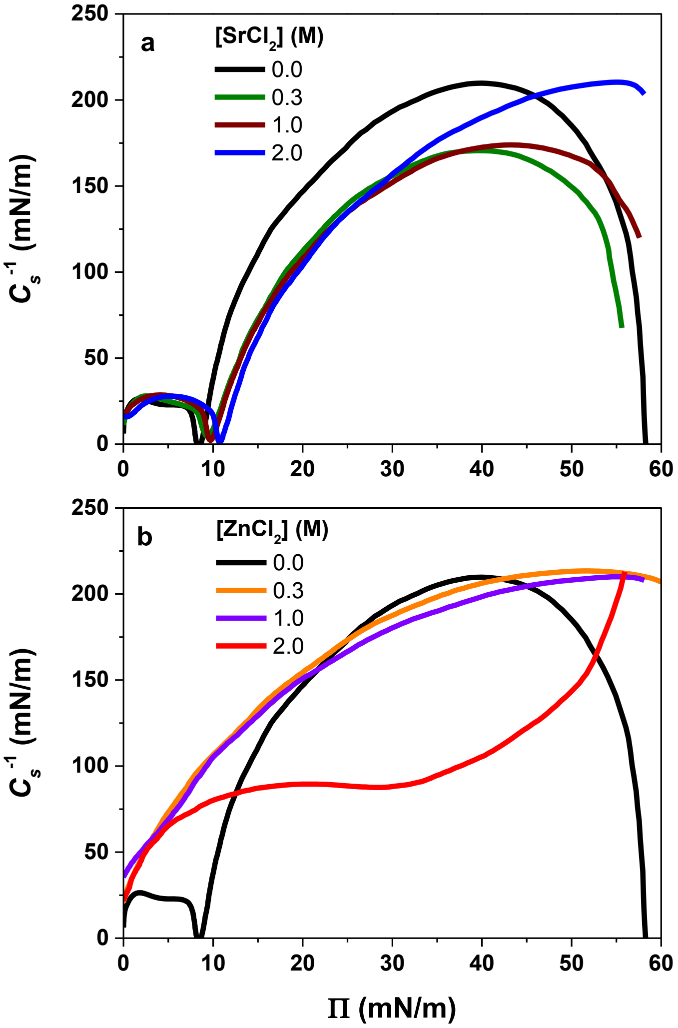

Figure 4.3. Compressibility modulus of DPPC on (a) $SrCl_2$ and (b) $ZnCl_2$ solutions at different salt concentrations.

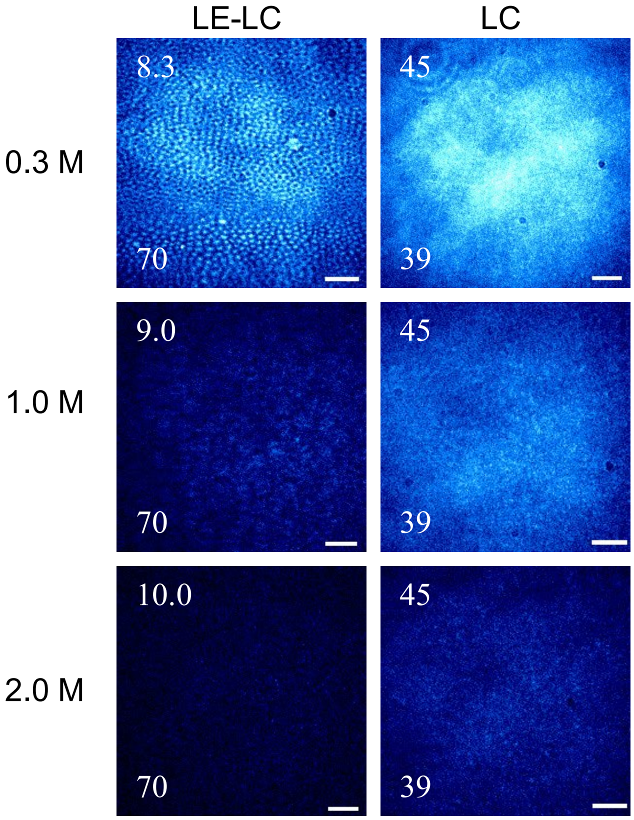

Figure 4.4. BAM images of DPPC on $SrCl_2$ solutions in the LE-LC and LC phases. The respective surface pressure is indicated in the top left corner, while MMA is displayed in the bottom left corner. Scale bar is 50 µm for all images.

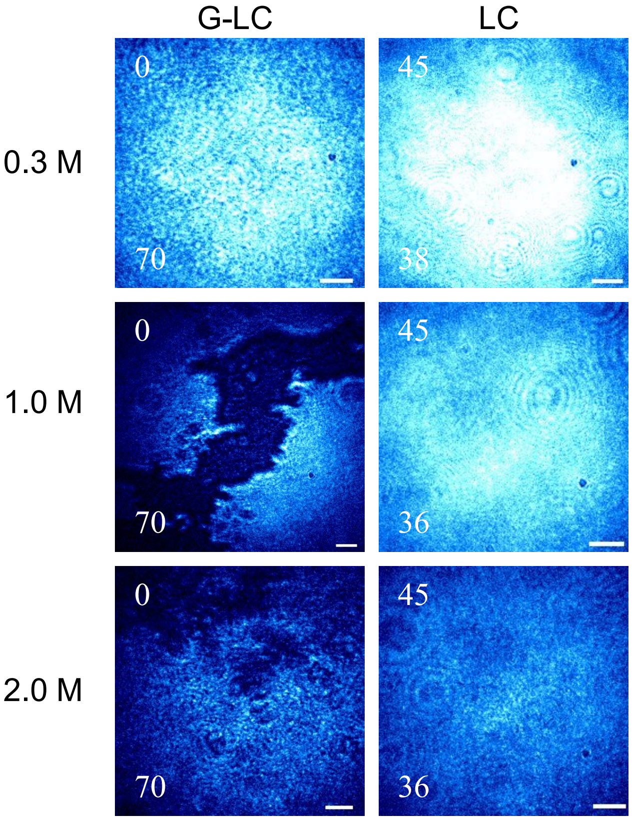

Figure 4.5. BAM images of DPPC on $ZnCl_2$ solutions in the G-LC and LC phases. The respective surface pressure is indicated in the top left corner, while MMA is displayed in the bottom left corner. Scale bar is 50 µm for all images.

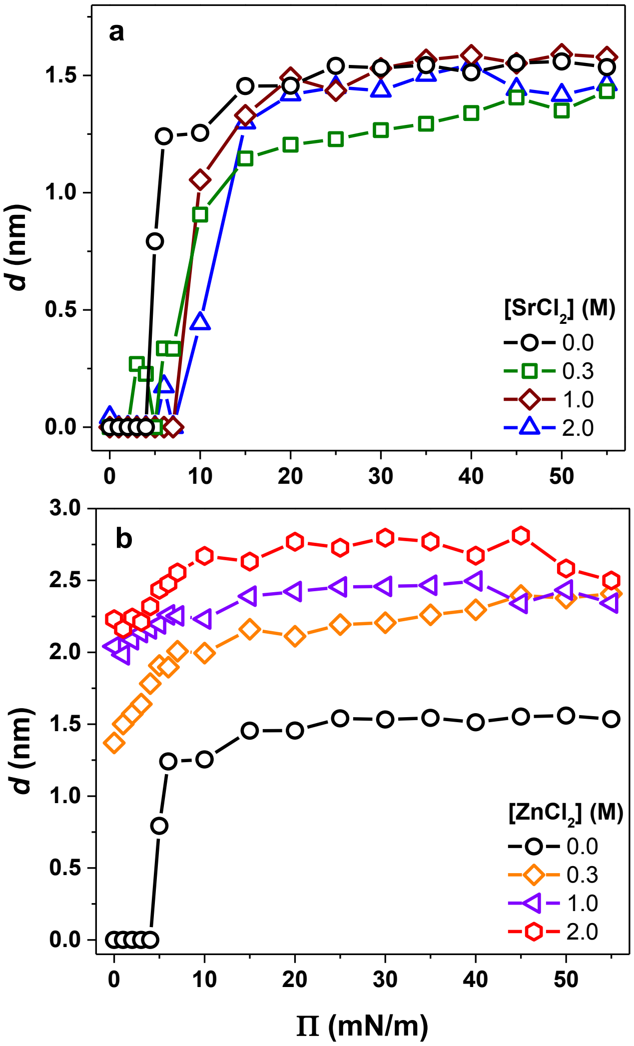

Figure 4.6. Change in monolayer thickness with surface pressure of DPPC monolayers on (a) $SrCl_2$ and (b) $ZnCl_2$ solutions.

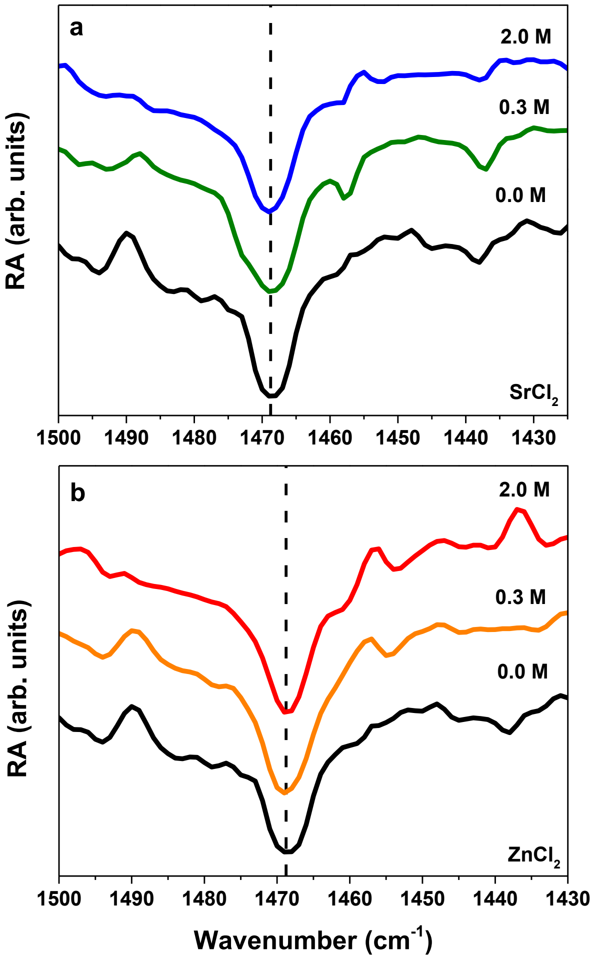

Figure 4.7. IRRAS spectra of CH_2 scissoring ($\delta(CH_2)$) mode of DPPC monolayers in the LC phase (40 mN/m) on (a) $SrCl_2$ and (b) $ZnCl_2$ solutions. A single peak is observed at 1469 cm^{-1} for all solutions, indicating DPPC molecules have a hexagonal 2-D lattice structure.

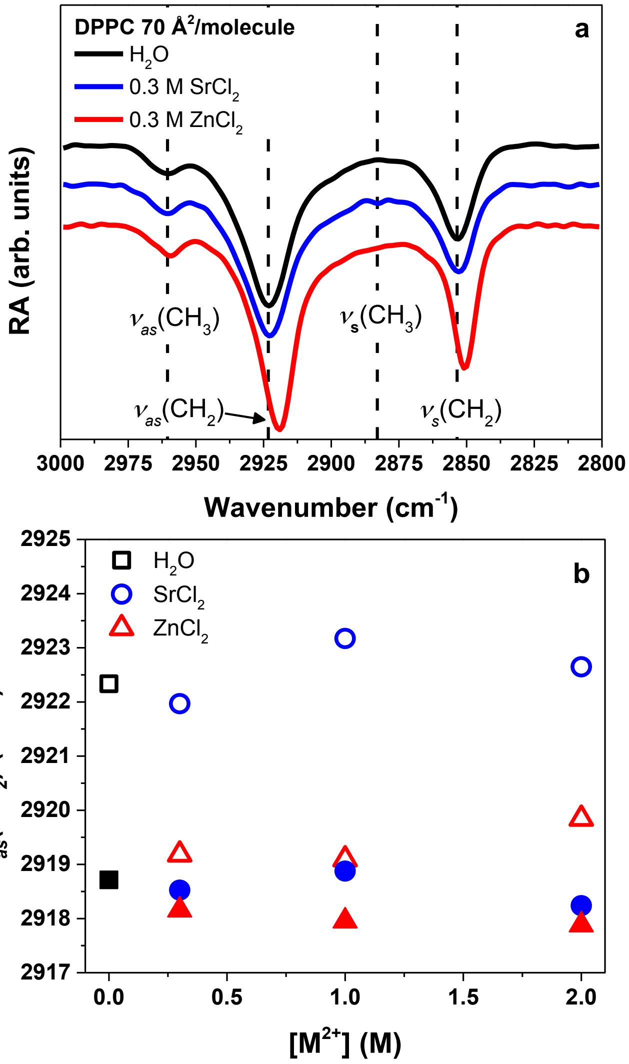

Figure 4.8. (a) IRRAS spectra of DPPC monolayers on 0.3 M solutions of $SrCl_2$ and $ZnCl_2$. The spectrum of DPPC on water is shown as reference. (b) Peak position of the DPPC $\nu_{as}(CH_2)$ vibrational mode as a function of salt concentration for DPPC monolayers in the coexistence region (LE-LC for $SrCl_2$ and G-LC phase for $ZnCl_2$ solutions; *open symbols*) and LC phase (*solid symbols*).

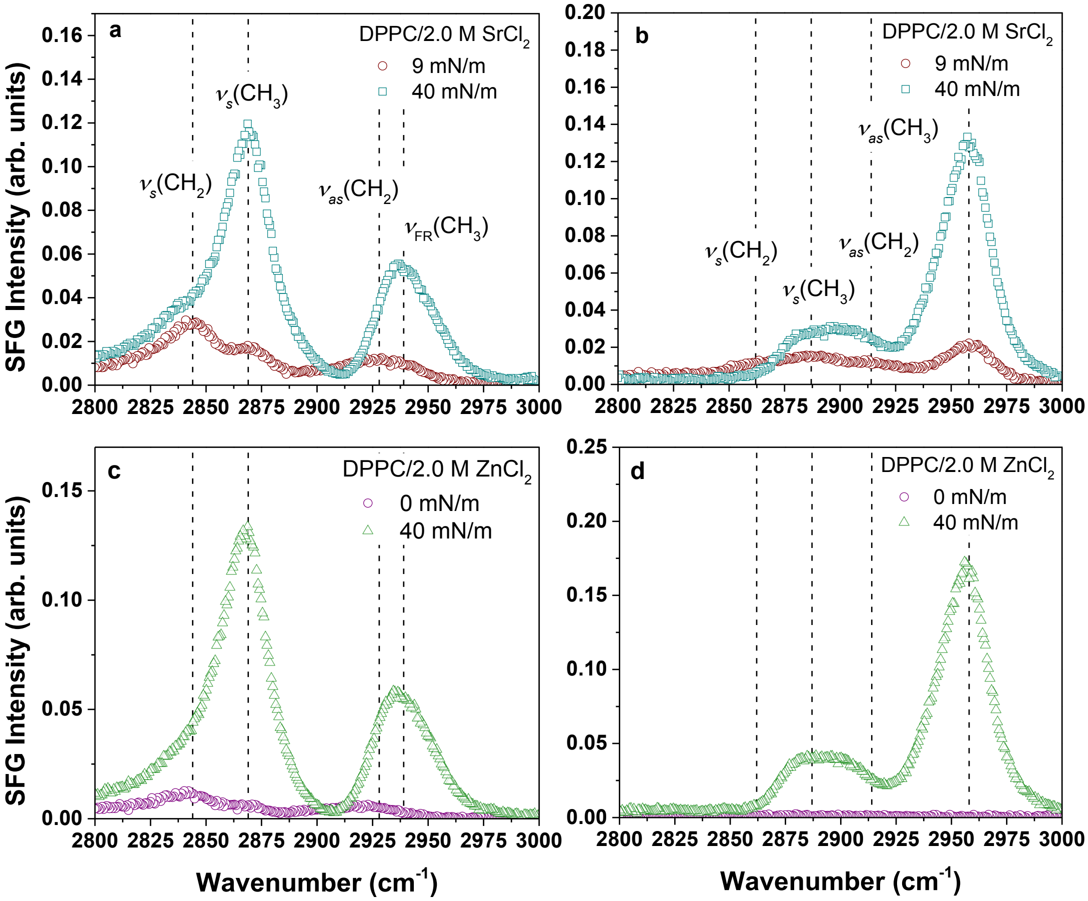

Figure 4.9. VSFG spectra of CH stretching region for DPPC monolayers on 2.0 M $SrCl_2$ and $ZnCl_2$ solution in (a, c) *ssp* and (b, d) *ppp* polarizations.

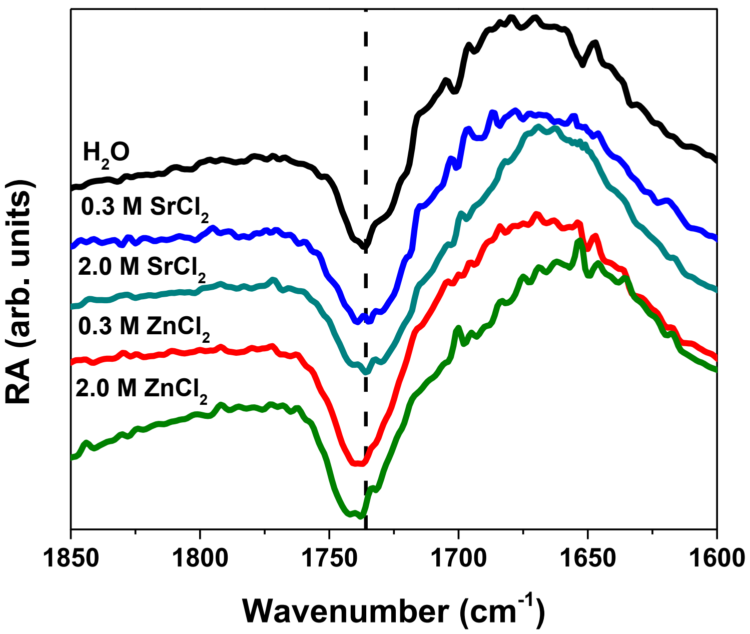

Figure 4.10. IRRAS spectra of the ν(C=O) vibrational mode for DPPC on SrCl$_2$ and ZnCl$_2$ solutions. A spectrum of DPPC on water is shown for reference.

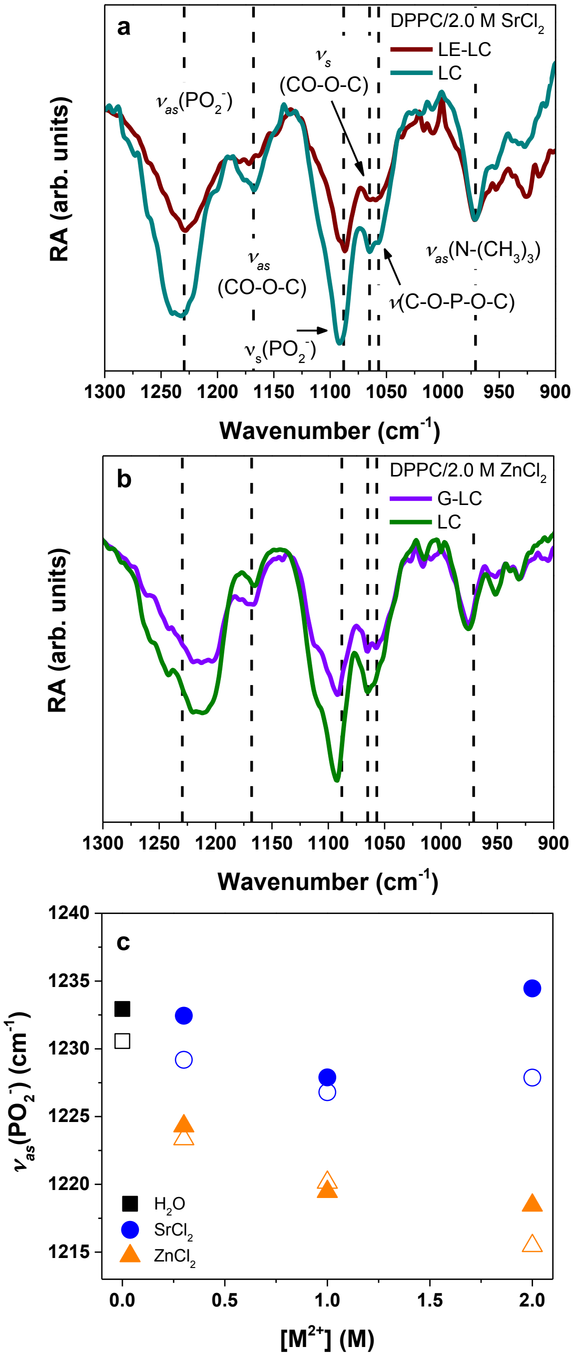

Figure 4.11. (a) IRRAS spectra of DPPC phosphate stretching region on 2.0 M (a) $SrCl_2$ and (b) $ZnCl_2$ solutions. (c) Peak position of the ν_{as}(PO_2^-) vibrational mode as a function of salt concentration. Open symbols represent DPPC monolayers in the coexistence region (LE-LC for $SrCl_2$ and G-LC for $ZnCl_2$ solutions) phase while solid symbols represent the LC phase.

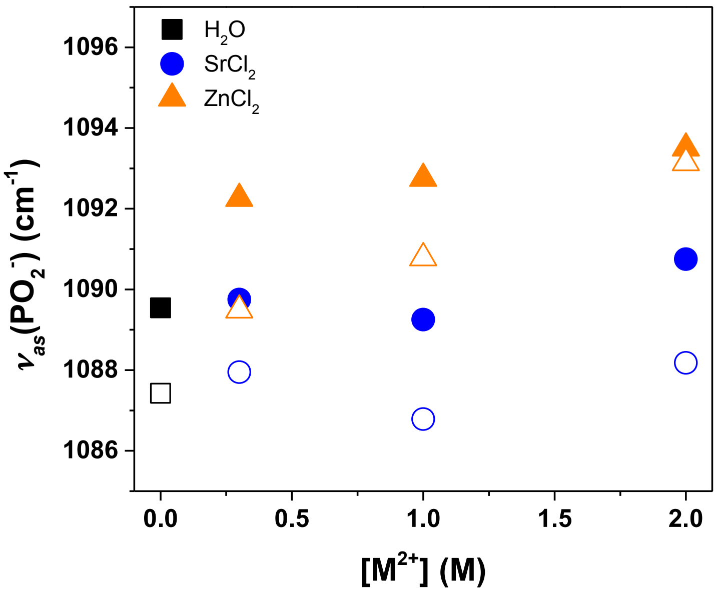

Figure 4.12. Peak position of the $\nu_s(PO_2^-)$ vibrational mode as a function of cation concentration. Open symbols represent DPPC monolayers in the coexistence region (LE-LC for $SrCl_2$ and G-LC for $ZnCl_2$ solutions) phase while solid symbols represent the LC phase.

Table 4.1. Measured Brewster angle ($\theta_{B,\text{meas}}$) and calculated refractive index of aqueous solutions ($n_{s,\text{calc}}$).

Solution	[MCl_2] (M)	$\theta_{B,meas}$ (°)	n_s
H_2O	–	53.1	1.33
$SrCl_2$	0.3	53.1	1.33
	1.0	53.6	1.36
	2.0	54.1	1.38
$ZnCl_2$	0.3	53.4	1.35
	1.0	53.7	1.36
	2.0	54.1	1.38

Table 4.2. Intensity ratio $I(\nu_s(\mathrm{CH_3}))/I(\nu_s(\mathrm{CH_2}))$ obtained from the VSFG spectra in *ssp* polarization and calculated tilt angles of the DPPC terminal methyl group and alkyl chain.

Solution	Π (mN/m)	$I(\nu_s(\mathrm{CH_3}))/I(\nu_s(\mathrm{CH_2}))$	θ_{CH3} (°)	θ_t (°)
H_2O	6	0.50 ± 0.10	23.4 ± 4.4	–
H_2O	40	3.91 ± 0.35	18.8 ± 2.1	22.7
0.3 M $SrCl_2$	6	0.60 ± 0.09	20.2 ± 3.9	–
0.3 M $SrCl_2$	40	3.12 ± 0.14	19.1 ± 2.9	22.4
1.0 M $SrCl_2$	7	0.61 ± 0.05	19.3 ± 4.4	–
1.0 M $SrCl_2$	40	2.99 ± 0.14	17.9 ± 1.9	23.6
2.0 M $SrCl_2$	9	0.60 ± 0.15	19.4 ± 2.7	–
2.0 M $SrCl_2$	40	2.76 ± 0.14	18.9 ± 2.6	22.6
0.3 M $ZnCl_2$	40	2.72 ± 0.08	19.1 ± 3.3	22.4
1.0 M $ZnCl_2$	40	3.10 ± 0.16	20.0 ± 2.4	21.5
2.0 M $ZnCl_2$	0	0.48 ± 0.09	–	–
2.0 M $ZnCl_2$	40	2.82 ± 0.26	19.9 ± 2.4	21.6

Chapter 5: Solvation of PC-Zn^{2+} Complexes Investigated by Vibrational Sum Frequency Generation Spectroscopy

5.1. Introduction.

Transition metals are crucial to biological systems, where they have roles in catalytic reactions, molecular structure stabilization, and DNA transcription.[139] Binding of these metal cations to model biological membranes is of particular interest as complexation to amphiphilic molecules is ion-specific,[30,125,126] the nature of which is hard to predict. Some transition metals, such as Zn^{2+}, promote fusion of lipid vesicles and bilayers,[42] while others, like Fe^{3+}, disrupt packing of molecules at the air-aqueous interface.[43] Furthermore, studies have shown that the interaction of transition metals with lipids depends on the relative amount of water available.[109,130] Probing of interfacial water structure near model membrane surfaces by vibrational sum frequency generation (VSFG) spectroscopy has demonstrated that organization of the hydrogen-bonding network is perturbed by as little as 10 μM of transition metal chloride salts.[140–142] Comparatively, alkaline earth cations also perturb the interfacial water structure, but have the opposite effect (enhancement vs. suppression of hydrogen-bonding continuum), which indicates that ion interaction with the monolayer are different.[140,141,143]

To date, most studies of transition metals and model membrane systems have been restricted to relatively low ion concentrations (≤ 200 mM),[30,109,125,126,130,140–142] as concentrations of transition metals are relatively low (μM or nM) in most biological systems.[139] In the case of the sea surface microlayer (SSML) and sea spray aerosol (SSA), however, transition metals are found to be enriched (relative to sodium) by factors of 10^6.[33,34,122,35] Enrichment of transition metals is thought to stem from complexation with lipid molecules.[35] Studies of phytoplankton blooms have found that transition metals are enriched in particles classified as biological or sea salt organic-carbon (SSOC).[22] Enrichment was not observed for sea salt (SS) particles,[22] which would support this hypothesis. Work presented in Chapter 4 found that Zn^{2+} strongly interacted with a dipalmitoylphosphatidylcholine (DPPC) monolayer, and that highly concentrated $ZnCl_2$ solutions impacted its surface properties and organization. Furthermore, solvation of the PC headgroup was observed to increase with increasing Zn^{2+} concentration, which suggested that the organization of interfacial water molecules is also significantly impacted. As properties of the SSML and aerosols, including evaporation, chemical reactivity,[144] and ice nucleation,[145] are influenced by the hydrogen-bonding environment of the interface, it is important to understand the organization and properties of interfacial water when transition metals are enriched.

In the study presented here, the effect of divalent cations Zn^{2+} and Sr^{2+} on a DPPC monolayer was probed with VSFG spectroscopy. Results reveal that Zn^{2+} perturbs the interfacial water structure to a greater extent than Sr^{2+}. At high concentrations of Zn^{2+}, interfacial water molecules reorganize such that they preferentially solvate the PC-Zn^{2+}

complex, resulting in a hydrogen-bonding continuum that resembles that of the neat-air water interface.

5.2. Experimental.

5.2.1. Materials.

1,2-Dipalmitoyl-*sn*-glycero-3-phosphocholine (DPPC) (> 99%, Avanti Polar Lipids) was used as received, and was dissolved in chloroform (HPLC grade, Fisher Scientific) to make a 1 mM solution. Stock solutions of strontium chloride ($SrCl_2•6H_2O$) (> 99%, ACS certified, MP Biomedical, United States) and zinc chloride ($ZnCl_2$) (> 98%, Acros Organics, United States) were prepared by dissolution in ultrapure water with a resistivity 18.2 MΩcm (Barnstead Nanopure Filtration System, model D4741, Thermolyne Corporation, United States) and a measured pH of 5.6. Trace organic impurities were removed from stock solutions by filtration through activated carbon filter several times.[69] VSFG spectra were collected in the CH region to verify cleanliness of stock solutions. Concentration of stock solutions was established by Mohr titration.[76] Solutions of desired concentration were then prepared by dilution of the stock solutions. In the case of $ZnCl_2$ solutions, a few drops of HCl (trace metal grade, Fisher Scientific) were added to prevent formation of $Zn(OH)_2$, resulting in a measured pH of 4.8. A period of 12 hours was allowed for equilibration of solutions to room temperature (23 ± 1°C) before experiments were performed.

5.2.2. Vibrational Sum Frequency Generation Spectroscopy

VSFG experiments were performed with the visible-infrared broadband sum frequency spectrometer setup (BBSFG-1) that was described in Chapter 2. Due to limitations in the IR bandwidth, the OH continuum region (3000-3600 cm^{-1}) and the free OH region (~3700 cm^{-1}) could not be simultaneously measured in one spectrum, and had to be collected separately. The visible beam had a fixed pulse energy of 70 μJ, while the IR beam had energies of 7 and 4 μJ in the OH continuum and free OH regions, respectively. Spectra were acquired for 5 minutes in *ssp* polarization (*s*-SFG, *s*-visible, *p*-IR). Vertical binning of the CCD chip was done to reduce background noise and cosmic radiation spikes. Spectra were then background-corrected and averaged before being normalized to the reference spectrum of GaAs.

All experiments were performed at the air-aqueous interface of a Langmuir trough (KSV Minitrough, Finland) with a surface area of 144 cm^2. Monolayers of DPPC were prepared by dropwise spreading of the chloroform solution onto a clean aqueous solution surface. Ten minutes was allowed for chloroform evaporation. The monolayer was then compressed to the desired target (mean molecular area (MMA) or surface pressure), where the barriers would oscillate to maintain the target surface pressure. Surface pressure was measured with a paper Wilhelmy plate.

5.3. Results and Discussion.

5.3.1. Effect of $SrCl_2$ and $ZnCl_2$ on the Interfacial Water Structure.

VSFG spectra of the interfacial water structure of $SrCl_2$ and $ZnCl_2$ solutions at the air-aqueous interface are shown in Figure 5.1. The spectrum of the neat air-water interface is shown as a reference for all salt solutions. For neat water, a broad feature is observed in the spectral region spanning 3000-3550 cm^{-1} (Figure 5.1a,c), and is attributed to interfacial water molecules having a continuum of hydrogen-bonding strengths and lengths.[146] A variety of assignments have been suggested for this region,[147–150] but it is generally accepted that as the frequency increases the strength of hydrogen-bonds between water molecules decreases. The narrow band observed at 3700 cm^{-1} (Figure 5.1b,d) is attributed to dangling or free O-H groups of topmost water molecules that point into the vapor phase.[146]

It can be seen in Figure 5.1a,c that the hydrogen-bonding continuum shape and intensity is affected by the presence of ions, depending on the cation identity and concentration. The free OH, unlike the continuum, appears to be unaffected by the presence of $SrCl_2$ or $ZnCl_2$ as the same intensity is observed relative to water. This is consistent with other studies of concentrated chloride solutions.[95,151–153] In the case of 2.0 M $ZnCl_2$, however, a slight decrease is observed relative to water, which could be indicative of ion pairing in the interface region.

In the case of $SrCl_2$, the spectrum closely resembles that of water at low concentration (0.3 M). With increasing concentration the intensity of the continuum decreases, and the band narrows, with the distribution centered at ~3300 cm^{-1}. Narrowing of the band is consistent with previous studies of 2.0 M solutions of $MgCl_2$ and $CaCl_2$, and was previously attributed to a disruption in the hydrogen-bonding network of water molecules.[95,154] Heterodyne-detected VSFG (HD-VSFG), however, revealed that narrowing of the distribution results from spectral convolution of the real and imaginary $\chi^{(2)}$ elements.[154] Unlike $SrCl_2$, an increase in the hydrogen-bonding network intensity was observed relative to water for $MgCl_2$ and $CaCl_2$ solutions. The presence of ions in the interface region causes the formation of an ionic double layer, which induces an interfacial electric field. The region of non-centrosymmetry is extended as a consequence, meaning that an increased population of hydrogen-bonding water molecules are probed due to increased interfacial depth.[155] Changes in the number of contributing water molecules as well as their relative alignment factor into the observed intensity change relative to water.[156] The diminished intensity of the continuum observed for $SrCl_2$ relative to water indicates that the population of hydrogen-bonding water molecules probed in the interfacial region has decreased. This could suggest that the surface propensity of Sr^{2+} ions may be different than Mg^{2+} and Ca^{2+} ions, but HD-VSFG measurements are needed to determine this.

For $ZnCl_2$ solutions, the hydrogen-bonding continuum increases in intensity relative to water for both the low and high frequency regions. The high frequency band at 3400 cm^{-1} is slightly more intense than the low frequency band at 3200 cm^{-1}, which suggests that there is a larger population of weakly hydrogen-bonded water molecules. The intensity change appears to be independent of concentration, which indicates that the alignment or number of contributing water molecules is the same for all concentrations.

Results shown here indicate that $ZnCl_2$ perturbs interfacial water structure more than $SrCl_2$.

5.3.2. Interfacial Water Structure of a DPPC Monolayer on $SrCl_2$ and $ZnCl_2$ Solutions.

Figure 5.2 shows the VSFG spectra of interfacial water molecules next to a DPPC monolayer as a function of surface pressure. The spectrum of the neat air-water interface is shown for reference. For both 6 and 40 mN/m, representative of the liquid expanded-liquid condensed (LE-LC) and LC phases, an enhancement of the SFG signal occurs relative to neat water. For the continuum, the band at 3200 cm^{-1} is more intense than the 3400 cm^{-1} band, consistent with previous studies of PC monolayers.[156] The enhancement results from the induced electric field of the PC headgroup. As surface pressure increases the intensity of both bands increases due to increased number density of lipid molecules. In the free OH spectrum, a feature appears at 3600 cm^{-1}, which is attributed to the solvation shell of the PC headgroup. This feature also increased in intensity when the monolayer is more compressed. It should be noted that the while the free OH peak is not present in the spectrum, previous studies have shown that dangling groups still exists at the surface when a full monolayer is present.[157]

The water VSFG spectra for a DPPC monolayer on $SrCl_2$ and $ZnCl_2$ solutions at a MMA of 70 Å^2/molecule is presented in Figure 5.3. A spectrum of DPPC on water is provided for reference. At this MMA DPPC is in the LE-LC phase on water and $SrCl_2$ solutions, and in the G-LC phase on $ZnCl_2$ solutions. For DPPC/$SrCl_2$, a decrease in continuum intensity is observed relative to DPPC/water. The intensity decreases with increasing concentration, and narrowing of the band is also observed for the 2.0 M solution. No appreciable change in the solvation shell feature is observed at any concentration. In the case of DPPC/$ZnCl_2$ solutions, the spectra collected for 0.3 and 1.0 M solutions has the same shape and intensity as the neat air-aqueous spectra. Furthermore, the free OH band is still observed, which indicates that DPPC monolayers do not impact on the organization of interfacial water at 0 mN/m. For the 2.0 M solution, however, a decrease in intensity is observed relative to the other DPPC/$ZnCl_2$ spectra, and the continuum broadens, with intensity appearing at 3450-3600 cm^{-1}. The free OH spectrum shows a decreased intensity from the 3700 cm^{-1} band, and an increase in intensity centered at 3575 cm^{-1}.

The decrease in intensity for the DPPC/$SrCl_2$ spectra with increasing $SrCl_2$ concentration is likely due to a charge screening effect.[140] The chloride (Cl^-) and Sr^{2+} ions preferentially interact with the positively charge choline and negatively charged phosphate group, respectively. This interaction essentially screens the effective charge of the monolayer, resulting in overall surface charge neutralization. The induced electric field from the PC headgroup is reduced, which decreases the population of water molecules that are probed. Furthermore, the charge screening effect should increase with increasing concentration based on the Debye length (λ_D) of the interface. The Debye length is the screening length of electrostatic forces at the interface, and decreases with increasing electrolyte concentration.[158] In the case of DPPC/2.0 M $ZnCl_2$, the intensity of the spectra are less than that of the neat air-aqueous or air-water interface. This observation cannot be explained by charge screening effects, as 2.0 M $SrCl_2$ and $ZnCl_2$

should have the same Debye length. The significantly decreased intensity may be indicative of strong binding to the PC headgroup, which will be discussed in more detail below.

Figure 5.4 shows the VSFG spectra of interfacial water molecules near a DPPC monolayer in the LC phase (40 mN/m) on $SrCl_2$ and $ZnCl_2$ solutions. A spectrum of DPPC/water is shown for reference. Similar to the LE-LC phase, the intensities of the spectra relative to DPPC/water are decreased for DPPC/$SrCl_2$ solutions, and the intensity decreases with increasing $SrCl_2$ concentration. The charge screening effect is not as strong in the LC phase compared to LE-LC phase, however. The ratio of the DPPC/0.3 M $SrCl_2$ to DPPC/water band intensity at 3200 cm^{-1} in the LC is twice that of the LE-LC phase. This indicates that Sr^{2+} ions interact with the DPPC monolayer more strongly in the LE-LC phase, which is consistent with surface pressure-area isotherms and IRRAS measurements. In the case of DPPC/$ZnCl_2$ interfaces, the signal in the continuum region significantly decreases, such that the signal is similar to the neat air-water interface. Furthermore, an increase in intensity is observed in the high frequency region (~3575 cm^{-1}). This new feature increases in intensity and shifts to lower wavenumbers with increasing $ZnCl_2$ concentration, which can be seen more clearly in the free OH spectra (Figure 5.4d). As stated previously, the suppression of the continuum observed for DPPC/$ZnCl_2$ interfaces cannot be explained fully by charge screening effects. Previous studies of DPPC/$CaCl_2$ similarly saw a significant decrease of the hydrogen-bonding network intensity on concentrated $CaCl_2$ solutions and attributed it to the formation of a PC-Ca^{2+} complex that was asymmetrically solvated.[153] Suppression of the hydrogen-bonding continuum observed here likely stems from the formation of PC-Zn^{2+} complexes, as X-ray reflectivity, IRRAS and FTIR studies have found that Zn^{2+} ions bind strongly to the PC headgroup.[68,109,134] As suppression of the continuum is concurrent with the appearance of a new feature in the region attributed to headgroup solvation, the new band at 3575 cm^{-1} can be attributed to the solvation shell of the PC-Zn^{2+} complex. Solvation shells of carboxylate headgroups complexed with Mg^{2+} and Ca^{2+} ions have similarly been observed in this region.[143] The intensity of the solvation shell increases with increasing Zn^{2+} concentration, which indicates that the number of water molecules contributing to the solvation shell increases. Furthermore, shifting of the center frequency of this mode to lower wavenumber suggests that the hydrogen-bonding strength of the solvation shell increases with increase $ZnCl_2$ concentration. This could indicate that water molecules in the interfacial region preferentially interact with the PC-Zn^{2+} complex more than other water molecules.

5.4. Conclusions.

Here, the impact of $SrCl_2$ and $ZnCl_2$ on the interfacial organization of water molecules near a DPPC monolayer was probed with VSFG. Perturbation of the interfacial water hydrogen-bonding network was observed for both ions, the extent of which depended upon the bulk salt concentration and DPPC lipid phase. Sr^{2+} was found to have a stronger effect in the LE-LC phase relative to the LC phase, indicating Sr^{2+} ions interact more strongly with the monolayer at low lipid coverage. In the LC phase, Zn^{2+} caused a greater perturbation than Sr^{2+}, in accordance with their binding affinities. At high $ZnCl_2$ concentrations, the organization of the hydrogen-bonding continuum resembles that of the neat air-water interface and is accompanied by the appearance of a strong signal attributed to the solvation shell of the PC-Zn^{2+} complex. Results obtained here have implications for the SSML and SSA. Water molecules in the interfacial region preferentially solvate the lipid-ion complex, meaning there are less water molecules available to participate in the uptake of trace gases and the ice nucleation process.

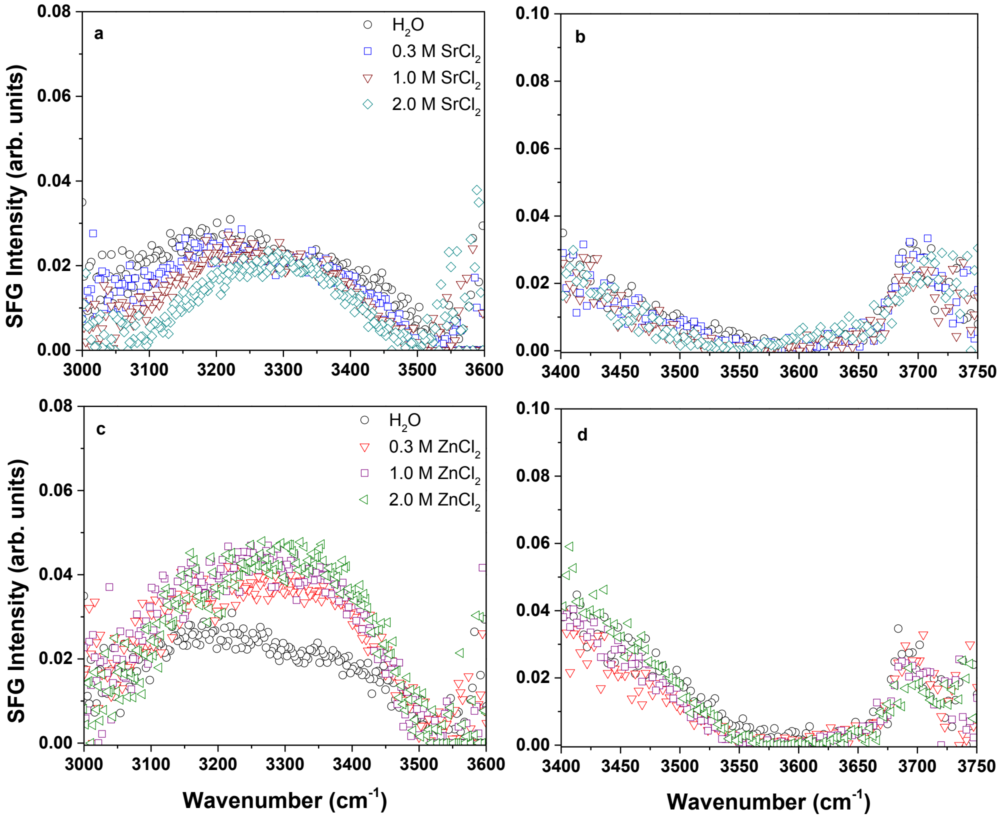

Figure 5.1. VSFG spectra in the OH region of neat aqueous solutions of $SrCl_2$ (a,b) and $ZnCl_2$ (c, d). The spectrum of water is shown for reference. Every fourth data point is plotted for convenience.

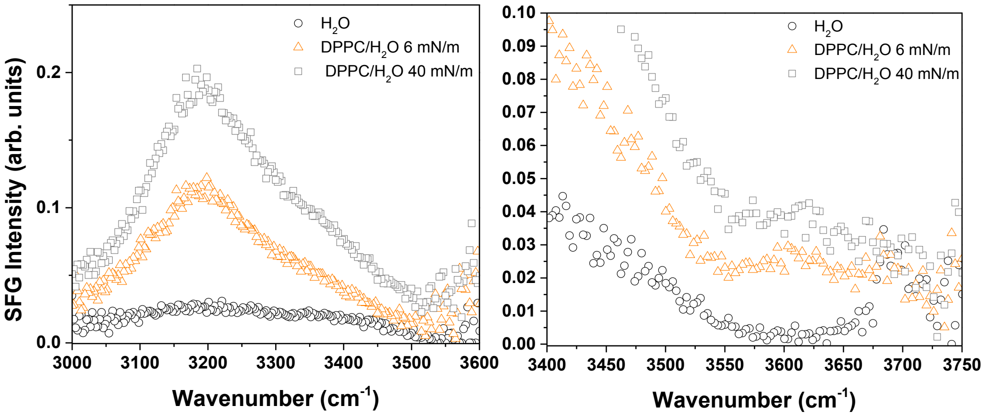

Figure 5.2. VSFG spectra in the OH region of a DPPC monolayer on water in the LE-LC phase (6 mN/m) and the LC phase (40 mN/m). A spectrum of the neat air-water interface is shown for reference. with increasing surface pressure. Every fourth data point is plotted for convenience.

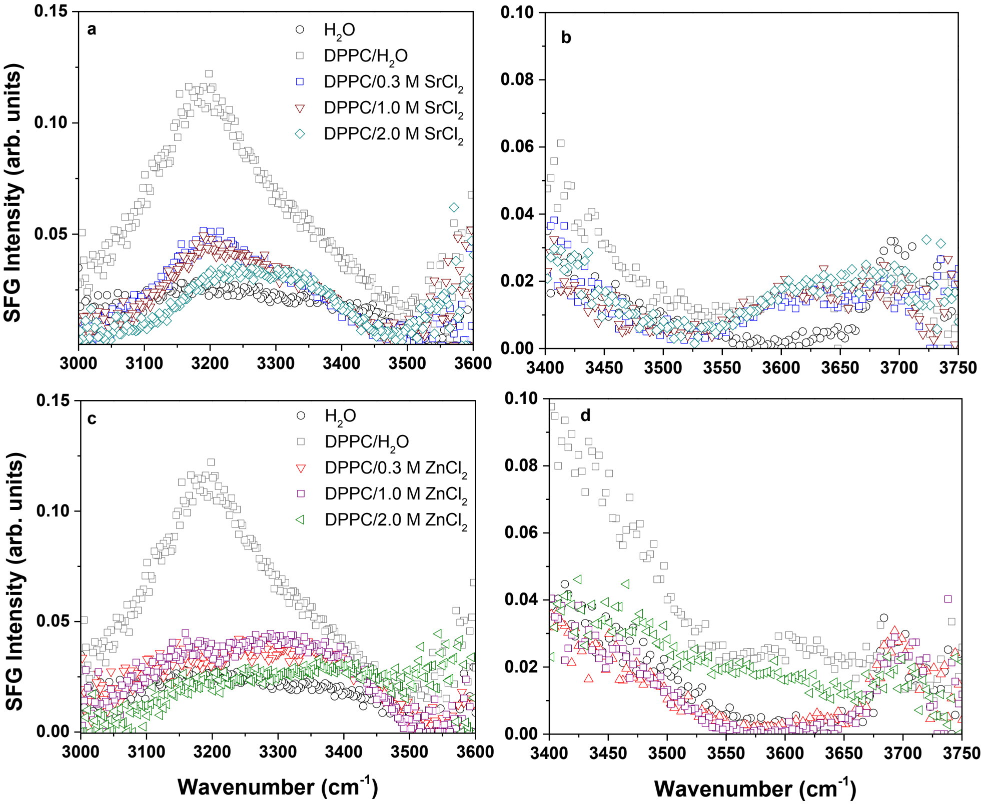

Figure 5.3. VSFG spectra in the OH region of a DPPC monolayer at 70 Å^2/molecule on $SrCl_2$ and $ZnCl_2$ solutions. Spectra of the neat air-water interface and DPPC/water are provided as reference. Every fourth data point is plotted for convenience.

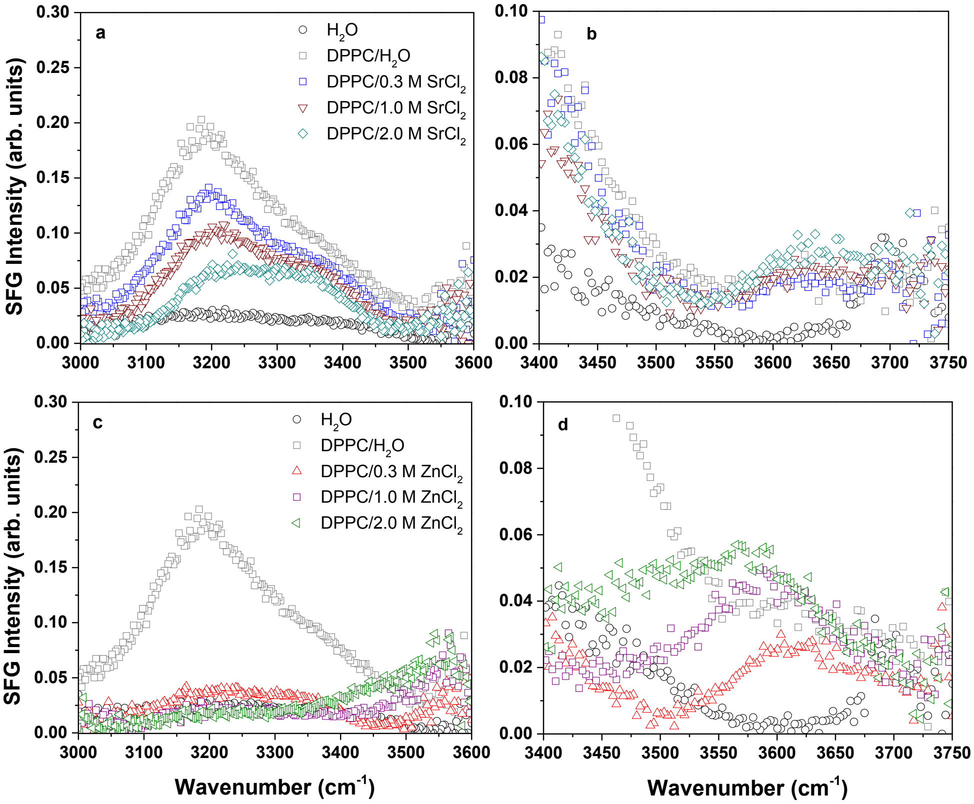

Figure 5.4. VSFG spectra in the OH region of a DPPC monolayer at 40 mN/m on $SrCl_2$ and $ZnCl_2$ solutions. Spectra of the neat air-water interface and DPPC/water are provided as reference. Every fourth data point is plotted for convenience.

Chapter 6: Water Structure at the Air-Aqueous Interface of Soluble and Insoluble Glycolipids

6.1. Introduction.

Carbohydrates constitute the most abundant class of organics in nature, and are important in metabolic and biochemical processes.[40] As such, it should not be surprising that ~80% of dissolved organic carbon (DOC) in the sea surface microlayer (SSML), the organic rich layer at the ocean surface, is composed of carbohydrates.[159] Carbohydrates have similarly been found in sea spray aerosols (SSA),[20,36,160] where they are transferred from the ocean surface to aerosols through bubble bursting.[21] They have been identified in both the water-soluble and water-insoluble fractions of SSA,[18,161] indicating they can exist as free monomers (i.e. glucose) or as part of a more complex molecule (i.e. polysaccharides or glycolipids). Recent studies of the SSML and SSA have found spectral signatures from lipopolysaccharides (LPS),[162–166] a major component of the outer wall of Gram-negative bacteria.

LPS are complex molecules that can be divided into three regions: a hydrophobic lipid portion with an oligosaccharide headgroup, known as lipid A, an oligosaccharide core that can also contain phosphate and amino acids groups, and an O-antigen chain of varying length composed of varying saccharide groups.[40]

Due to the prevalence of LPS molecules on the surface of bacteria, the interaction of LPS with phospholipids and proteins has been investigated by means of Langmuir monolayers.[167,168] Interfacial properties of LPS molecules alone have similarly been characterized with monolayer compression.[169–171] However, the majority of these studies have used a truncated version of LPS, which decreases its solubility and promotes surface activity, and is therefore not truly representative of the interfacial properties of this molecule. Furthermore, the solvation and water structure of LPS, and carbohydrates in general,[172] at the interface is not well understood.

Interfacial properties of carbohydrate-containing molecules is important in SSA, as physical and optical properties of aerosols are dependent on the organization and structure of their surfaces.[8] In this study, the conformational order of LPS and cerebroside, an insoluble glycosphingolipid found in oceanic algae blooms,[173] and the hydrogen-bonding network at the air-aqueous interface was investigated by vibrational sum frequency generation (VSFG) spectroscopy. Glucose and ceramide were also studied, as they are both found at the ocean surface as breakdown products of cerebroside.[20,174] Results indicate that all lipids studied had similar alkyl chain conformation, but impacted the hydrogen-bonding network to different extents. LPS and glucose had similar effects, which may indicate that solvation of the sugar groups differs for soluble and insoluble glycolipids.

6.2. Experimental.

6.2.1. Materials.

D-Glucose (≥ 99.5%) was purchased from Sigma-Aldrich (United States). LPS from *Escherichia coli* L4130 (≤ 2% RNA impurities, 1-10% protein impurities) and L2630 (~60% RNA impurities, ≤ 1% protein impurities) were purchased from Sigma-Aldrich. LPS solutions of 1 mg/mL were prepared by dissolution in ultrapure water. Cerebroside and ceramide were purchased from Avanti Polar Lipids (Alabama, United States) and Alexis Biochemical (United Kingdom) respectively, and used as received. Each lipid was dissolved in a 1:1 chloroform:methanol mixture (both HPLC grade, Fisher Scientific; HPLC grade, Fisher Scientific) to prepare a 1 mM solution. Ultrapure water with a resistivity of 18.3 MΩcm was obtained with a water purification system (Barnstead Nanopure Filtration System, model D4741, Barnstead/Thermolyne Corporation). All experiments were conducted at room temperature (22 ± 1 °C).

6.2.2. Vibrational Sum Frequency Generation Spectroscopy.

Two different BBSFG spectrometer setups were used collect spectra in this chapter. CH spectra of ceramide and cerebroside were collected with BBSFG-2, while all other spectra were collected with BBSFG-1. The BBSFG-1 system was described in Chapter 2. Energy of the VIS was fixed at 70 μJ and IR pulses in the CH, OH continuum, and free OH stretching regions had energies of 14, 7, and 4 μJ, respectively. The full CCD chip was used to collect the SFG signal but a cosmic correct function was selected in the spectrometer software (SpectraSense 5.0) to remove cosmic radiation spikes. Spectra were collected for 2 min in *ssp* (*s*-SFG, *s*-VIS, *p*-IR) and *ppp* polarization combinations. Final spectra shown here were background-subtracted and normalized to the non-resonant SFG profile of a GaAs(110) crystal (II-VI Inc., United States). Peak positions in the VSFG spectra were calibrated by comparison of the non-resonant absorption spectrum from a polystyrene film to those collected with an FTIR spectrometer.

The BBSFG-2 system has been previously described in literature,[153] and is detailed in Chapter 2. Average energies of the IR and visible pulses at the sample were 14 and 180 μJ, respectively. Polarization combinations of *ssp* and *ppp* were utilized to probe different vibrational modes of the monolayer. Spectra were acquired for 1 min with a cosmic–correct function selected in the software (SpectraSense 5.0) in *ssp* and *ppp* polarization combinations. All spectra were background-corrected, and normalized to the non-resonant profile of GaAs(110) (II-VI, Inc). Peak positions in the VSFG spectra were calibrated by comparison of the non-resonant absorption spectrum from a polystyrene film to those collected with an FTIR spectrometer.

Surface pressure of the ceramide and cerebroside monolayers was controlled with a Langmuir trough (KSV Minitrough, Finland). Monolayers of ceramide and cerebroside were prepared by spreading an appropriate amount of lipid solution on pure water (measured pH 5.6). Prior to spreading the presence of organic impurities was monitored by compressing barriers to observe if a significant rise in surface pressure (> 0.2 mN/m) occurred and collecting a VSFG spectrum of the bare water surface. Ten minutes was allowed for solvent evaporation before the monolayer was symmetrically compressed (5 mm/min/barrier) to the target surface pressure. Surface pressure was held constant during the VSFG measurement through oscillation of the barriers (1 mm/min/barrier, forward and backward directions).

6.3. Results and Discussion.

6.3.1. Alkyl Chain Conformation of Glycolipids.

As the purification method of LPS influences the amount and type of impurities (RNA vs. protein) present, LPS purified from two different methods was compared to see if any structural differences could be observed. LPS L4130 had a larger percentage of protein impurities while LPS L2360 had a larger percentage of RNA impurities. For convenience, the two types of LPS will be hereafter referred to as LPS-protein and LPS-RNA to identify the impurity that was most abundant. VSFG spectra in *ssp* and *ppp* polarization combinations of LPS in the CH region are shown in Figure 6.1. Three peaks are observed in the *ssp* spectra and can be attributed to the CH_2 symmetric stretch ($\nu_s(CH_2)$), CH_3 symmetric stretch ($\nu_s(CH_3)$), and the CH_3 Fermi resonance ($\nu_{FR}(CH_3)$) at 2855, 2880, and 2937 cm^{-1}, respectively. In the *ppp* spectra the $\nu_s(CH_2)$ and $\nu_s(CH_3)$ are observed as well, along with the CH_2 and CH_3 asymmetric stretches ($\nu_{as}(CH_2)$ and $\nu_{as}(CH_3)$) at 2915 and 2955 cm^{-1}, respectively.[27,175] The peak positions for the two LPS types are at slightly different wavenumbers (~4 cm^{-1}) difference, and could be due to the interactions of the LPS molecules with the respective impurities. The fitted peak positions of the different LPS types can be found in Table 6.1. It can be seen however, that the two types have the same trend, with peaks from the CH_3 groups being more intense than the CH_2 peaks in both polarization combinations. Based on the electric dipole approximation, SFG is not allowed for molecules with centrosymmetry. When alkyl chains are in a nearly *trans* configuration, the $\nu_s(CH_2)$ in *ssp* polarization should have a minimal SFG response while the $\nu_s(CH_3)$ should have a strong response. As the $\nu_s(CH_3)$ peak is more intense than the one from the $\nu_s(CH_2)$ mode, the alkyl chains of LPS molecules have more *trans* bonds than *gauche* defects. Formation of a disordered monolayer has similarly been observed for other soluble surfactants.[175] Results obtained for LPS show that impurities influence the peak position, but structural properties are overall the same.

Figure 6.2 shows *ssp* and *ppp* VSFG spectra of cerebroside in the CH region. As cerebroside is an insoluble lipid and able to form a Langmuir film, CH spectra were measured at several surface pressures to assess how the chain conformation changes with lipid density. In the *ssp* spectra, the $\nu_s(CH_2)$, $\nu_s(CH_3)$, $\nu_{as}(CH_2)$, and $\nu_{FR}(CH_3)$ modes are observed. The $\nu_s(CH_3)$, $\nu_{as}(CH_2)$, and $\nu_{as}(CH_3)$ modes are observed in the *ppp* spectra. The fitted peak positions of these modes can be found in Table 6.1. In *ssp* polarization, the $\nu_s(CH_3)$ is more intense than the $\nu_s(CH_2)$ mode, which indicates that the alkyl chain is well ordered (more *trans*). As some intensity from the $\nu_{as}(CH_2)$ mode is observed, however, there is likely a small amount of *gauche* defects within the alkyl chains. It can be seen in both polarization combinations that the peak intensities are dependent upon the surface pressure. The intensity is greatest for 10 mN/m, and decreases with increasing surface pressure. The cerebroside monolayer begins to form collapse structures at 55 mN/m, which are bilayer or trilayer structures.[66] The decrease in intensity is consistent with the formation of these structures, as centrosymmetric bilayers will not give rise to SFG.[176]

VSFG spectra of ceramide in the CH region for *ssp* and *ppp* polarization combinations are shown in Figure 6.3. The alkyl chain conformation was also evaluated as a function of surface pressure. Similar to cerebroside, the $\nu_s(CH_2)$, $\nu_s(CH_3)$, $\nu_{as}(CH_2)$, and $\nu_{FR}(CH_3)$ are observed in the *ssp* spectra. The $\nu_{FR}(CH_3)$ is broad and asymmetric though, which may indicate that the $\nu_{as}(CH_3)$ mode may also contributes here. In *ppp* spectra, the $\nu_s(CH_2)$, $\nu_s(CH_3)$, $\nu_{as}(CH_2)$, and $\nu_{as}(CH_3)$ are observed. Fitted peak positions of these modes are presented in Table 6.1. The alkyl chains are well ordered, as the $\nu_s(CH_3)$ intensity is greater than that of the $\nu_s(CH_2)$ mode in the *ssp* spectra. No change in intensity is observed for the different surface pressures, which suggests that ordering of the chains is similar at different packing densities.

Relative ordering of the alkyl chains for LPS, cerebroside, and ceramide can be obtained from the intensity ratio $I(\nu_s(CH_3))/I(\nu_s(CH_2))$. A higher value of the intensity ratio corresponds to a greater number of *tran*s bonds in the alkyl chain. Values of $I(\nu_s(CH_3))/I(\nu_s(CH_2))$ for LPS solutions as well as cerebroside and ceramide monolayers at 30 mN/m are presented in Table 6.2. Comparison of the LPS solutions reveals that there is no significant difference between the two, with the LPS-RNA has a slightly higher value. Of the insoluble lipids, cerebroside has a much higher value than ceramide, indicating the chains are much more ordered for cerebroside. Ceramide has a comparable value to the LPS solutions. These results indicate that cerebroside has the most ordered alkyl chain of the glycolipids investigated here.

6.3.2. Interfacial Water Structure of Glucose Solutions.

Figure 6.4 shows VSFG spectra of glucose solutions in the OH region. A spectrum of water is shown for reference. In the case of the neat air-water interface, a broad feature (Figure 6.4a) is observed from 3000-3600 cm^{-1}, and can be attributed to interfacial water molecules possessing a hydrogen-bonding continuum of varying strengths and lengths. The strength of hydrogen-bonding decreases with increases frequency, with the bands at 3200 and 3400 cm^{-1} representing strongly and weakly hydrogen-bonded water molecules,[146,147,149] respectively. In Figure 6.4b a narrow band observed at 3700 cm^{-1} is attributed to non-hydrogen-bonded O-H groups.[146,157] For the 10 mM glucose solution, the intensity of the hydrogen-bonding network decreases relative to water, with the 3400 cm^{-1} band suppressed to a greater extent than the 3200 cm^{-1} band. Enhancement of both the 3200 and 3400 cm^{-1} bands is observed for the 1 M glucose solution, and is consistent with studies of other carbohydrates.[172] Similar to the 10 mM solution, the 3200 cm^{-1} band is more intense than the 3400 cm^{-1} band. The free OH band intensity (Figure 6.4b) is not impacted by the addition of glucose to the solution.

Surface tension measurements of glucose have shown that the surface tension increases relative to water with increasing glucose concentration,[177,178] similar to the trend observed for salts.[178,179] Historically, an increase in surface tension relative to water has been interpreted as the solute species being depleted in the interfacial region, which would consequentially lead to increased hydrogen-bonding of interfacial water molecules. VSFG and heterodyne-detected VSFG (HD-VSFG) studies of salt solutions have found that this is not necessarily the case, as some salts like NaCl and KCl have no effect on the interfacial water structure,[151,152] while others such as $NaNO_3$ and $NaClO_4$ cause the hydrogen-bonding network to decrease in intensity.[151,180,181] These differences stem from the induced electric field of the respective salt, where charge separation and surface propensities of the cation and anion influence the interfacial depth of the non-centrosymmetric region. Spectra collected here for 10 mM and 1 M glucose solutions have opposite trends, which suggests that the population of water molecules or the depth of the interface is different in these two concentration regimes. In order to de-convolute the contributions of glucose and water molecules in this region, chiral VSFG measurements are needed.[182]

6.3.3. Interfacial Water Structure of Glycolipids.

VSFG spectra in the OH region of LPS-protein and LPS-RNA are shown in Figure 6.5. A spectrum of water is shown for reference. Significant enhancement of the hydrogen-bonding network occurs for both LPS solutions. The observed shape is similar to 1 M glucose, with the 3200 cm^{-1} band being more intense. The high frequency band center has shifted to ~3500 cm^{-1} for the LPS solutions compared to 3400 cm^{-1} for glucose, which indicates that there is a population of water molecules that are more disordered (less hydrogen-bonded) than those observed for glucose. LPS molecules have charged carboxylate and phosphate moieties in the headgroup region, which could contribute to the enhancement observed here. Signal intensity does differ slightly between the LPS solutions and could indicate that the impurities in solution influence water structure.

Figure 6.6 shows VSFG spectra in the OH region for cerebroside and ceramide at various surface pressures. A spectrum of water is shown for reference. As can be seen, the water structure of either lipid monolayer is not impacted by surface pressure once the monolayer is compressed to a surface pressure greater than 0 mN/m. In the case of cerebroside, the intensity of the hydrogen-bonding network increases, and two bands of equal intensity are observed at 3250 and 3450 cm^{-1}. These bands appear to be narrower than those observed for water, which could suggest a reduced distribution of hydrogen-bonding environments. Differential scanning calorimetry measurements have found that cerebroside headgroups interact with 4-9 water molecules.[183] Hydrogen-bonding between adjacent galactose headgroups is also likely to occur. Therefore it may be possible that these narrow bands reflect the hydrogen-bonding environment of water molecules with the galactose headgroup or the galactose headgroup itself. However, as mentioned earlier, chiral VSFG is needed to determine the OH contribution from the galactose moiety.

For ceramide an enhancement relative to water is also observed. Two bands are also observed, where the 3250 cm^{-1} band is more intense than the 3475 cm^{-1} band. Compared to cerebroside, bands are broader, which indicates a larger distribution of hydrogen-bonding environments for the alcohol headgroup. In general, no distinct trend was observed for the interfacial water structure of glycolipids. This suggests that the interfacial water structure is lipid dependent, despite these lipids having similar headgroups.

6.4. Conclusions.

In this study the interfacial structure of the atmospherically-relevant molecules glucose, LPS, cerebroside, and ceramide were investigated by VSFG spectroscopy. *Gauche* defects were observed in the alkyl chains of all lipids investigated, indicating that slightly disordered monolayers form for both soluble and insoluble glycolipids. Probing of the interfacial water molecules revealed that the hydrogen-bonding network was perturbed to different extents, with LPS having the strongest effect. The present study may shed light on the growth, adsorption, and chemical reactivity of aerosols containing saccharides and glycolipids. Exchange of water and uptake of gases are likely impacted by the relative concentration of soluble species, as glucose was found to influence the hydrogen-bonding network differently in the low and high concentration regimes. Solvation of sugar groups likely differs for soluble and insoluble lipids, as narrow hydrogen-bonding bands were observed for cerebroside. Future studies in which chiral VSFG is utilized may help determine the solvation structure of sugar groups.

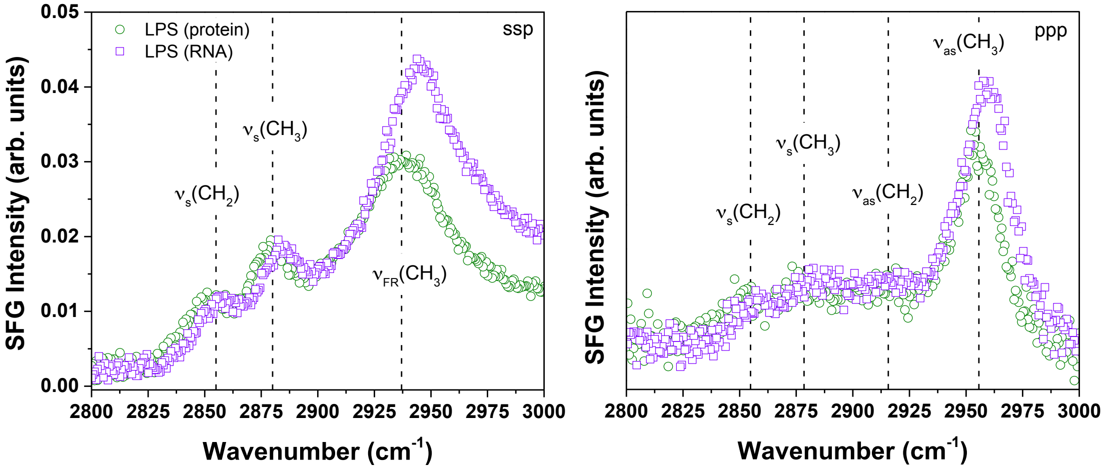

Figure 6.1. VSFG spectra in the CH region of LPS for *ssp* (left) and *ppp* (right) polarization combinations.

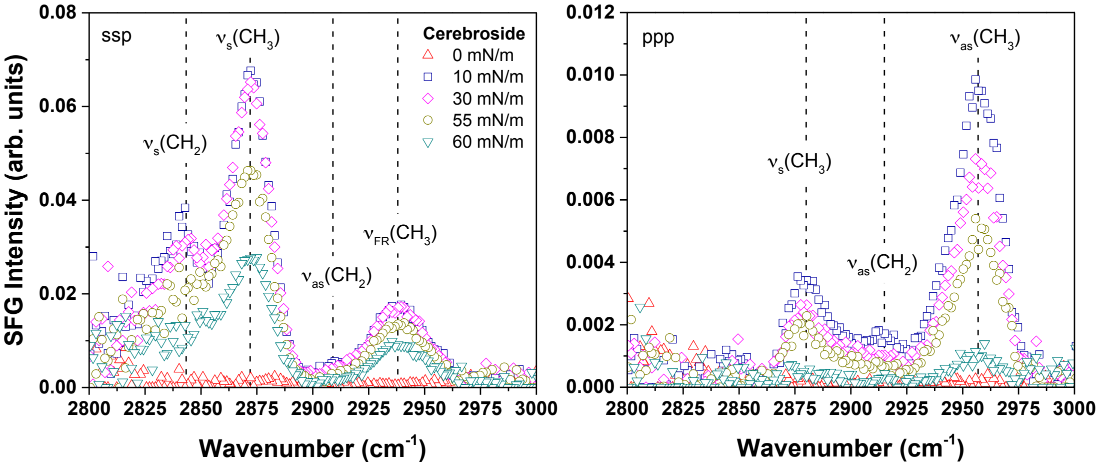

Figure 6.2. VSFG spectra in the CH region of cerebroside at various surface pressures for *ssp* (left) and *ppp* (right) polarization combinations.

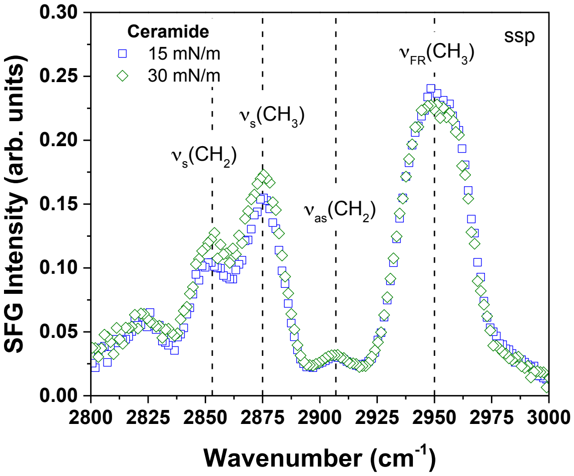

Figure 6.3. VSFG spectra in the CH region of ceramide at various surface pressures for *ssp* (left) and *ppp* (right) polarization combinations.

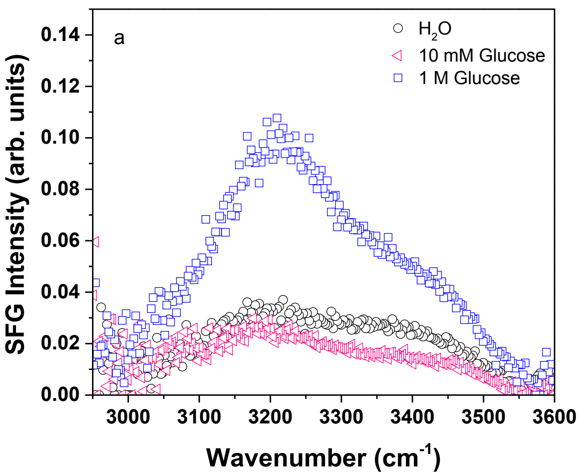

Figure 6.4. VSFG spectra in the (a) OH and (b) free OH regions of glucose solutions. A spectrum of water is shown for reference.

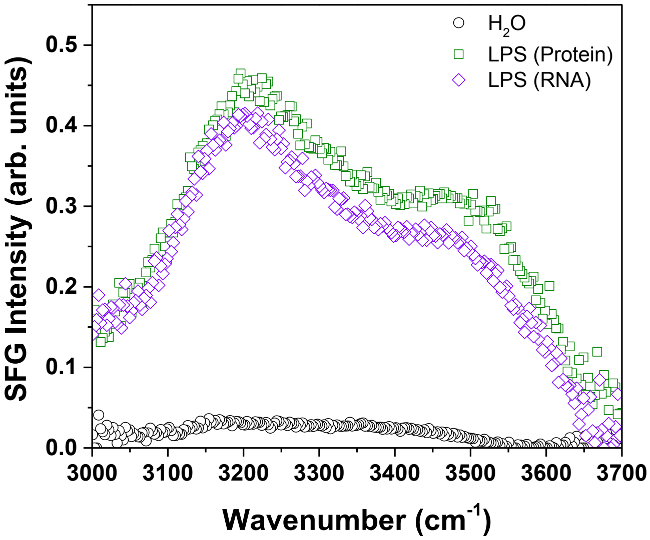

Figure 6.5. VSFG spectra in the OH and regions of LPS-protein and LPS-RNA solutions. A spectrum of water is shown for reference.

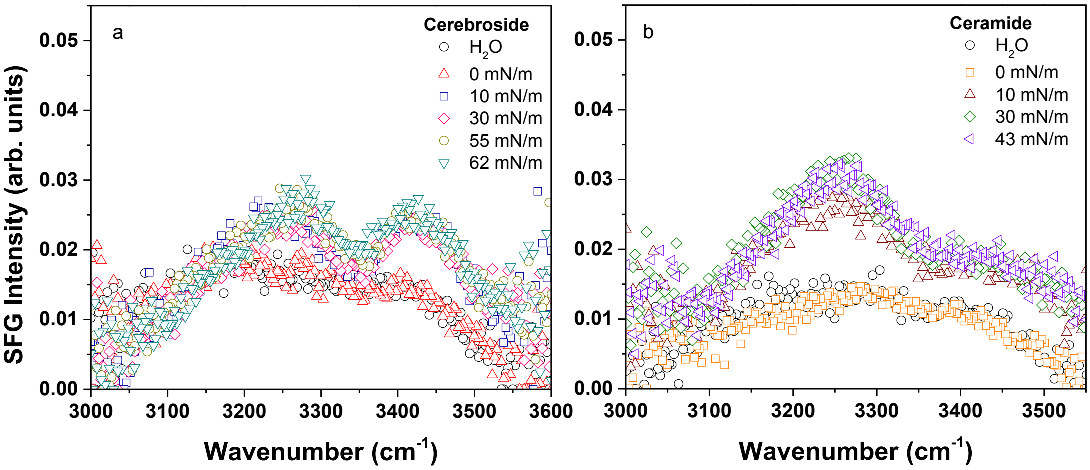

Figure 6.6. VSFG spectra in the OH region of cerebroside (left) and ceramide (right) monolayers at different surface pressures. A spectrum of water is shown for reference

Table 6.1. Fitted peak positions in the CH stretching region for LPS solutions and cerebroside and ceramide monolayers.

	Fitted Peak Frequency (cm^{-1})				
Glycolipid	CH_2-ss	CH_3-ss	CH_2-as	CH_3-as	CH_3-FR
LPS-protein	2851	2879	2915	2955	2937
LPS-RNA	2855	2882	2915	2958	2943
Cerebroside	2840	2872	2909	2938	2955
Ceramide	2853	2875	2906	2902	2951

Table 6.2. Intensity ratio $I(\nu_s(CH_3))/I(\nu_s(CH_2))$ obtained from the VSFG spectra in *ssp* polarization.

Glycolipid	$I(\nu_s(CH_3))/I(\nu_s(CH_2))$
LPS (RNA impurity)	1.67
LPS (protein impurity)	1.56
Cerebroside (30 mN/m)	2.46
Ceramide (30 mN/m)	1.45

Chapter 7: Na$^+$-Induced Stabilization of Palmitic Acid Monolayers: Influence of pH on Interfacial Properties

7.1. Introduction.

Marine aerosols are ubiquitous in the atmosphere and impact the climate directly through solar radiation absorption and scattering, and indirectly, through processes such as cloud formation.[2] Sea spray aerosols (SSA) are generated from breaking waves and wind shearing at the ocean surface, in which film and jet droplets become entrained in the atmosphere.[16] Relative to bulk seawater, SSA are enriched with organic species, which includes lipids, carbohydrates, amino acids, and proteins.[184,8,19] Enrichment of organic species has been shown to be size-dependent,[20] with fine SSA (≤ 1 μm, submicron fraction) dominated by organic species and coarse SSA (≥1 μm, supermicron fraction) mainly composed of a sea salt core coated by a thin organic layer. [7,23,26] Studies have also suggested that pH of marine aerosols depends on their relative size; submicron particles were found to be acidic whereas supermicron particles were more basic in nature.[185,39,38] Whether this pH difference is linked to organic composition remains unclear, but it has been demonstrated that the chemical reactivity of aerosols in these two size regimes with trace gases is linked to the acidity/basicity of organic functional groups.[32,166]

Physical and optical properties of aerosols are impacted by the organization of surface-active molecules, which alter surface tension,[186] hygroscopicity,[9,15,187] and chemical reactivity of particles.[10] Fatty acids constitute an important class of surface-active lipids that are known to be enriched in the sea surface microlayer (SSML) and SSA.[6,25] Interfacial properties of fatty acids have been investigated by a multitude of techniques.[188,65,189,190,127] Surprisingly, studies on the influence of pH on the surface properties of fatty acids are sparse in literature,[191–195] and the majority of these studies focus on fatty acids with 20 carbons chain lengths or greater.[191–193] Solubility of fatty acids increases with decreasing chain length, and as most fatty acids in SSA have chain lengths in the range of C_{14}-C_{18},[6,25] it is likely that stability and surface activity of these shorter chain fatty acids decreases upon dissociation of the carboxylic acid headgroup.

One goal of this study was to determine how pH influences the interfacial properties of a fatty acid-coated SSA. To this end, a fatty acid Langmuir monolayer was utilized as a simplified model of the organic-coated aerosol surface. Palmitic acid (PA) was chosen as the representative fatty acid, as it was found to be the most abundant in both fine and coarse SSA.[25] Because the bulk pH of ocean water is ~8.2 and the interfacial pK_a of PA is known to be ~8.7,[192,196] the bulk pH in studies done here was varied from 6.7-10.7 to represent different degrees of dissociation of the carboxylic headgroup in SSA. This study was conducted with equilibrium spreading pressure (ESP) measurements as well as surface-sensitive spectroscopic techniques IRRAS and VSFG spectroscopy to probe the stability, protonation state, and structural organization of the PA monolayer and interfacial water molecules. Results show that increased dissociation of the PA headgroup leads to increased electrostatic repulsions within the monolayer, resulting in its dissolution into the bulk solution at high pH. Howver, addition of NaCl to the pH-adjusted solution increases the stability of the PA monolayer at high pH.

7.2. Experimental.

7.2.1. Materials.

Palmitic acid (>99%, Sigma Aldrich, United States), and deuterated palmitic acid (d_{31}-PA) (> 98%, Cambridge Isotopes, United States) were used as received, and were dissolved in chloroform to make 2 mM solutions. Sodium palmitate (>99%, Sigma Aldrich) was dissolved in water to make a 2 mM solution. Solutions of pH 6.7, 8.7, or 10.7 were prepared by addition of HCl (trace metal grade, Fisher Scientific, United States) or NaOH (ACS certified, Fisher Scientific) to ultrapure water (resistivity >18.0 MΩcm, Barnstead Nanopure Filtration System, model D4741, Barnstead/Thermolyne Corporation). For pH solutions of constant ionic strength an appropriate amount of a concentrated NaCl solution, which had been purified to remove organic impurities,[69] was added to make a 100 mM solution. Final pH of the solutions was measured (AB 15 pH meter, Fisher Scientific) to be within ± 0.1 pH units of the desired value. All solutions were allowed to equilibrate to room temperature for several hours before measurements were conducted. Experiments were performed at ambient temperature (295 ± 2 K) and pressure.

7.2.2. Methods.

Equilibrium Spreading Pressure Measurements.

ESP measurements were performed in a Langmuir trough (Minitrough, Biolin Scientific, Finland) with an area of 145 cm^2. Prior to experiments the trough was thoroughly cleaned with ethanol and ultrapure water. Surface pressure was measured with a Wilhelmy paper plate (Whatman 41, ashless grade). Approximately 1 mg of PA crystals was sprinkled onto a clean solution surface and the rise in surface pressure was monitored.[197–200] All experiments were conducted for at least 90 minutes until a constant equilibrium surface pressure was reached. Additional crystals were sprinkled on the surface to verify that no significant change in surface pressure (< 0.5 mN/m) was observed.[201] When the change in surface pressure was < 0.1 mN/m over a period of 15 min, the observed surface pressure was taken as ESP value.

Infrared Reflection-Absorption Spectroscopy.

Spectra were collected with an FTIR spectrometer (Perkin Elmer, Spectrum 100). The IRRAS setup was described in Chapter 2. Spectra were generated by the co-addition of 300 scans with 4 cm^{-1} resolution in single beam mode over the full spectral range (450-4000 cm^{-1}). Reflectance-absorbance (*RA*) was determined from the relationship $RA = -log (R_m/R_0)$, where R_m and R_0 are the reflectance of the monolayer-covered and bare surfaces, respectively. All experiments were completed in Petri dishes, where monolayers were prepared by spreading the lipid solution to mean molecular areas (MMA) representative of the tilted condensed (TC, 24 Å^2/molecule) and untilted condensed (UC, 20.5

Å^2/molecule) phases. Ten minutes was allowed for chloroform evaporation before spectra were collected.

Vibrational Sum Frequency Generation Spectroscopy.

Spectra were collected with a visible-infrared broadband sum frequency spectrometer (BBSFG-1) that was detailed in Chapter 2. The visible beam had an energy of 70 μJ/pulse while the IR had an energy of 10, 14, and 4 μJ/pulse in the CD (2000-2300 cm^{-1}), continuum OH (3000-3600 cm^{-1}), and free OH (3600-3800 cm^{-1}) regions, respectively. A co-propagating geometry was utilized in this setup, with the visible and IR beams incident at angles of 53° and 68°, respectively. The full CCD chip was utilized for signal collection, but a cosmic correct function was selected in the software (SpectraSense 5.0) to remove cosmic radiation spikes. Spectra were collected in *ssp* (*s*-SFG, *s*-visible, *p*-infrared) and *ppp* polarization combinations for a period of 2 minutes in the CD region. In the continuum and free OH regions spectra were acquired for 5 minutes in *ssp* polarization only, and vertical binning of the CCD chip was done to reduce cosmic radiation spikes. All spectra were background-subtracted and normalized to the non-resonant profile of GaAs(110). Calibration of the peak position was done by comparing the non-resonant absorption spectrum of polystyrene to one collected by an FTIR spectrometer (Perkin Elmer, Spectrum 100). Experiments were also completed in Petri dishes. Monolayers were spread at an MMA of 20.5 Å^2/molecule to represent the UC phase of PA.

7.3 Results and Discussion.

7.3.1. Equilibrium Spreading Pressure of PA Monolayers.

ESP is defined as the surface pressure at which a monolayer (2D phase) exists in thermodynamic equilibrium with a stable bulk phase (3D phase).[202,203]. ESP values reflect the relative stability of the monolayer and are indicative of the intermolecular forces (e.g. van der Waals, electrostatic repulsions, etc.) within the system. ESP values determined from the time evolution curves of surface pressure for a PA monolayer on pH solutions with and without additional NaCl are provided in Table 7.1. In the absence of NaCl, PA has a similar ESP values (~7.6 mN/m) for the pH 6.7 and 8.7 solutions. This is slightly lower than values (~10 mN/m) previously reported for a fully protonated PA monolayer on 0.01 M HCl solutions.[199,204] As the pH is increased to 10.7, a drastic increase in the ESP value to 42 mN/m is observed, consistent with previous studies of oleic acid, which found an increase in ESP as progressive deprotonation of the monolayer occurred.[205] The increase in ESP was attributed to the presence of negatively charged headgroups, which caused increased electrostatic repulsions within the monolayer, leading to its expansion. While increased electrostatic repulsions likely contribute to the increased ESP value observed here, an additional equilibrium between the monolayer and bulk solutions must be considered.[206] At this pH, PA molecules desorb and solubilize into the bulk solution due to the charged carboxylic headgroup. These molecules remain in the sub-surface region, similar to a soluble surfactant, and contribute to the measured surface pressure. This hypothesis was confirmed by sprinkling PA crystals on the surface of a 0.4 mM sodium palmitate pH 10.7 solution, where a similar ESP value was observed as PA on pH 10.7 solution.

The addition of 100 mM NaCl to the solution results in an increase in the ESP values to ~18 and 21 mN/m for the pH 6.7 and 8.7 solutions, respectively. Similarly, previous studies have found that salts increased ESP in a concentration-dependent manner.[207,208] The increased ESP values are also likely due to increased electrostatic repulsions within the monolayer. VSFG studies of PA monolayers at the air/water interface have found that Na^+ ions have the tendency to deprotonate the COOH headgroup.[27] Complete deprotonation of the monolayer did not occur, but modes resulting from the negatively charged carboxylate (COO^-) were observed, indicating that a fraction of the monolayer was charged. Electrostatic repulsion of charged molecules within the monolayer is therefore likely, which could explain the observed increase in ESP. It should be noted that for the pH 10.7 NaCl solution, the ESP is higher (31 mN/m) than the lower pH solutions, consistent with increased electrostatic repulsion as the fraction of charged molecules increases. However, compared to the pH 10.7 solution with no NaCl present, the value has decreased. The lower value may be explained by charge screening effects; a small portion of Na^+ ions likely form ionic complexes with the COO^- headgroup, resulting in charge neutralization. The presence of NaCl in solution appears to stabilize the monolayer when the majority of molecules are deprotonated.

7.3.2. Lattice Packing Structure of PA Monolayers.

Figure 7.1 shows IRRAS spectra of the CD_2 scissoring region for d_{31}-PA monolayers in the TC and UC phases on various pH solutions. Two peaks are observed at 1089 and

1060 cm^{-1}, which can be attributed to the CD_2 scissoring ($\delta(CD_2)$) mode and the C-C stretch (ν(C-C)) of the alkyl chain backbone,[209,57,193,210] respectively. As a single peak is observed for the $\delta(CD_2)$ mode, it is likely that alkyl chains adopt a hexagonal packing structure in both the TC and UC phases.[57] This is consistent with MD simulations and grazing X-ray diffraction studies, that found hexagonal or distorted hexagonal packing of alkyl chains occurred for a fully protonated monolayer.[211,212] For regular pH solutions, the scissoring mode is intense for pH 6.7 and 8.7 solutions, but is not observed for pH 10.7. This indicates that PA molecules are not at the surface, likely due to dissolution of the monolayer into the bulk solution when PA molecules are mostly ionized. However, this peak is still observed for the pH 10.7 NaCl solution, albeit much less intense than the other pH/NaCl solutions. The presence of the $\delta(CD_2)$ mode indicates that Na^+ ions increase the surface propensity of PA molecules. Similarly, scattering experiments and VSFG measurements of the negatively charged, soluble surfactant sodium dodecyl sulfate (SDS) found that salt addition to the solution drove surfactant molecules to the surface.[144,213] Despite the increased surface propensity of PA in the presence of Na^+ ions, it is likely that the orientation of the alkyl chains is greatly altered or that a fully formed monolayer does not exist, as the intensity of the CD_2 mode is greatly diminished.

7.3.3. Alkyl Chain Orientation of PA Monolayers.

VSFG spectra in the CD region in both *ssp* and *ppp* polarizations of d_{31}-PA monolayers in the UC phase (20.5Å^2/molecule) on different pH solutions are presented in Figure 7.2. In *ssp* polarization three peaks are observed and can be attributed to the CD_3 symmetric stretch ($\nu_s(CD_3)$) at 2068 cm^{-1}, CD_3 Fermi resonance ($\nu_{FR}(CD_3)$) at 2126 cm^{-1}

and CD_3 asymmetric stretch ($\nu_{as}(CD_3)$) at 2223 cm^{-1}. For *ppp* polarized spectra, the ($\nu_{as}(CD_3)$) peak is observed as well as peaks corresponding to the CD_2 symmetric ($\nu_s(CD_2)$), CD_2 Fermi resonance ($\nu_{FR}(CD_2)$), and CD_2 asymmetric stretching ($\nu_{as}(CD_2)$) modes, which occur at 2102, 2145, and 2196 cm^{-1}, respectively. In the case of *ssp* spectra, the absence of CD_2 modes indicates that alkyl chains are well ordered with a *trans* configuration. This is certainly the case for pH 6.7 and 8.7 solutions (with or without NaCl). Furthermore, a *trans* configuration is confirmed in *ppp* spectra, where an intense $\nu_{as}(CD_3)$ mode is observed.

However, no SFG response was detected for pH 10.7 solutions, which suggests that PA molecules are not at the surface. In contrast, IRRAS spectra indicated that at high pH the monolayer was slightly stabilized in the presence of 100 mM NaCl. This discrepancy may be due to the difference in probing depth of the respective techniques; IRRAS probes ~ 1.5-3 μm into the solution, whereas VSFG detects only the first few molecular layers. Furthermore, the number density of PA molecules at the surface may be below the detection limit of the technique, as the SFG response depends on the number of molecular contributors. It is therefore probable that PA molecules are in the sub-surface region, where they can be detected by IRRAS and surface tension measurements, but do not significantly contribute to VSFG spectra.

Besides providing information about the PA alkyl chain ordering, VSFG spectroscopy was also used to determine the orientation of the terminal methyl group, and subsequently, the tilt angle of the alkyl chain from the observed intensities. As established in Eq. (2.14), the SFG intensity is related to the effective second-order nonlinear susceptibility ($\chi_{eff}^{(2)}$). For *ssp* polarization $\chi_{eff,ssp}^{(2)}$ can be expressed as

$$\chi_{eff,ssp}^{(2)} = L_{yy}(\omega_{VSFG})L_{yy}(\omega_{VIS})L_{yy}(\omega_{IR})sin\theta_{IR}\chi_{yyz} \tag{8.1}$$

where *Lii* are the Fresnel coefficients associated with frequency ω_i, and θ_{IR} corresponds to the incident angle of the infrared beam. The component χ_{yyz} is correlated to the orientation of the terminal deuterated methyl group (θ_{CD3}), which possesses C_{3v} symmetry, in the following manner for symmetric (ss) and asymmetric (as) stretching modes

$$\chi_{yyz,ss}^{(2)} = \frac{1}{2} N_s\beta_{ccc}\left[(1+R)\langle cos\theta_{CD_3}\rangle - (1-R)\langle cos^3\theta_{CD_3}\rangle\right] \tag{8.2}$$

$$\chi_{yyz,as}^{(2)} = -N_s\beta_{aca}\left[\langle cos\theta_{CD_3}\rangle - \langle cos^3\theta_{CD_3}\rangle\right] \tag{8.3}$$

where R is the hyperpolarizability ratio defined as $R = \beta_{aac}/\beta_{ccc} = 2.3$.[64] Previous measurements have also determined the ratio $\beta_{aca}/\beta_{aac} = 4.2$.[63] The value of θ_{CD3} can be determined from the ratio $\chi_{ssp\text{-}ss}/\ \chi_{ssp\text{-}as}$, assuming that the orientation distribution is a δ-function.

The calculated values of the methyl group orientation, θ_{CD3}, and the alkyl chain tilt angle, θ_t, are presented in Table 7.2. These values could not be calculated for pH 10.7 solutions due to lack of SFG response. Assuming a nearly trans chain conformation, the C_3 axis is oriented 37° away from the surface normal, leading to the relation $\theta_t = 37 - \theta_{CD3}$.[213] For the pH 6.7 solution, the tilt angle is 28.6°, which is consistent with values found in previous studies of fatty acids.[192] The tilt angle increases to 33.1° in the presence of NaCl, likely due to interaction of Na^+ ions with the headgroup. In the case of pH 8.7

solutions, the tilt angle is not significantly different in the absence or presence of NaCl. As the monolayer is half deprotonated at this point, the charged headgroup most likely determines the organization of the alkyl chains.

7.3.4. Protonation State of COOH Headgroup.

Figure 7.3 shows IRRAS spectra of the C=O and COO^- region of d_{31}-PA monolayers in the UC phase (20.5Å^2/molecule) on various pH solutions. In the absence of additional NaCl (Figure 7.3a), two spectral features are observed: a peak at 1723 cm^{-1} is the stretching mode of the carbonyl group (ν(C=O)) and another peak at 1275 cm^{-1} from the C-OH stretch (ν(C-OH)) of the carboxylic acid.[57,193] Similar spectra are observed for pH 6.7 and 8.7 solutions, consistent with ESP measurements that indicated the monolayer was similarly organized on these two solutions. It can be seen for the pH 10.7 spectrum that a significant shift of the ν(C=O) mode to 1680 cm^{-1} occurs, along with the disappearance of the ν(C-OH) mode. The shift of the ν(C=O) mode to lower wavenumbers indicates increased hydration of the carbonyl group, and can be attributed to the formation of aggregates or micelles in solution.[214,215] As IRRAS and VSFG of CD vibrational modes showed PA molecules are not in the interfacial region for this solution, the signal observed from aggregates here likely comes from carboxylic acid micelles that exist in bulk solution.

In the presence NaCl (Figure 7.3b), additional peaks are observed at 1535 and 1384 cm^{-1} arising from the asymmetric and symmetric stretching modes of the COO^- group ($\nu_{as}(COO^-)$ and $\nu_s(COO^-)$), respectively. The appearance of these modes is pH-dependent, however. For pH 6.7 the ν(C=O) and ν(C-OH) modes are intense and the COO^- modes are not observed, which indicates that the majority of PA molecules in the monolayer exist in the protonated form. As the pH is increased to 8.7, the intensity of the ν(C=O) mode decreases and the $\nu_{as}(COO^-)$ mode appears. The fact that the ν(C-OH) mode is still observed at pH 8.7 confirms that PA molecules exist in both the protonated and deprotonated form. The COO^- features were not observed in the absence of NaCl for pH 8.7. Na^+ ions likely disrupt the hydrogen-bonding network of adjacent PA molecules, which is why the COO^- modes are present. At pH 10.7 the $\nu_s(COO^-)$ appears and the ν(C-OH) mode disappears. The ν(C=O) mode shifts to 1680 cm^{-1}, but is significantly less intense than for the pH 6.7 solution. This shows that molecules at the surface are negatively charged, but a small fraction of the monolayer dissolves into bulk solution as micelle formation is observed. Results obtained here indicate that the surface propensity of ionized PA molecules is increased in the presence of NaCl, and that in the absence of the salt, molecules dissolve into the bulk solution where they form micelles.

7.3.5. Interfacial Water Organization near PA Monolayers.

Figure 7.4 shows VSFG spectra in the OH region for pH 6.7, 8.7, and 10.7 solutions with and without 100 mM NaCl added. A spectrum of water is shown for reference. A broad feature is observed from 3000-3550 cm^{-1} (Figure 7.4a,c) and can be attributed to water molecules with a hydrogen-bonding continuum of varying strengths and lengths. It is generally accepted that hydrogen-bonding strength decreases with increasing frequency. A narrow band occurs at ~3700 cm^{-1} (Figure 7.4b,d) and is attributed to the dangling OH stretching mode.[146] No apparent difference in the hydrogen-bonding network is observed for solutions with different pH's. Furthermore, addition of NaCl does not appear to have any impact either. For all pH solutions, a decrease in the 3400 cm^{-1} band intensity occurs. This observation is consistent with studies of concentrated NaOH solutions.[216,217] The decrease in band intensity was attributed the presence of hydroxide ions (OH^-) in the interfacial region, in which solvation of the OH^- leads to water molecules having a more random orientation, similar to bulk solution. The intensity of the dangling OH band does not change for any pH solution relative to water.

VSFG spectra in the OH region of d_{31}-PA on different pH solutions, with and without NaCl, are presented in Figure 7.5. A spectrum of a PA monolayer on water (pH 5.6) is shown as reference. For the PA/water spectrum, bands can be observed at 3200, 3400, and ~3600 cm^{-1}, consistent with previous studies.[143] The band at 3600 cm^{-1} is attributed to the solvation shell of the carboxylic headgroup. For PA monolayers on pH 6.7 and 8.7 solutions that do not contain NaCl (Figure 7.5a,b), enhancement of the 3200 cm^{-1} band occurs relative to PA/water. The enhancement likely indicates an increase in the induced electric field at the interface due to an increase in the number of deprotonated PA molecules. For the PA monolayer on the pH 10.7 solution a decrease in intensity relative to PA/water is observed. The intensity of the hydrogen-bonding network is comparable to the bare pH 10.7 interface, which suggests that PA molecules are not at the interface. This is confirmed by the appearance of the dangling OH bond, which was not observed for pH 6.7 or 8.7, and is consistent with results from IRRAS measurements.

In the case of PA monolayers on pH solutions containing 100 mM NaCl (Figure 7.5c,d), an enhancement of the 3200 cm^{-1} band relative to PA/water was observed at all pHs. For pH 6.7 and 8.7 solutions the enhancement is greater in the presence of NaCl, which suggests that the background electrolyte increases the induced electric field. This could be achieved through deprotonation of the carboxylic acid headgroup by Na^+ ions, or charge separation of the Na^+ and Cl^- ions. As concentrated NaCl solutions have been shown to have little effect on the interfacial hydrogen-bonding network,[216,152,218,151,69] it is more likely that the enhancement observed here is due to deprotonation of the carboxylic acid. Enhancement of the 3200 cm^{-1} band increases even more at pH 10.7, indicating the presence of PA molecules at the interface. This is further evidence that the addition of NaCl to the solution drives deprotonated PA molecules to the interfacial region.

7.4. Conclusions.

In this study, the effect on pH on the interfacial properties of a PA monolayer was investigated. Results indicate that organization of the monolayer changes as the degree of dissociation of the carboxylic headgroup is altered. Deprotonation of the headgroup increases electrostatic repulsions within the monolayer, leading to decreased stability, and a change in the PA alkyl chain orientation. When the majority of the monolayer is deprotonated PA molecules dissolve into bulk solution, where they form aggregate or micellar structures. Addition of NaCl salt to the bulk solution was found to have little effect on the alkyl chain packing structure or orientation. However, NaCl was found to increase the surface propensity of dissolved species to the interface, as spectroscopic signatures of ionized species were detected in the interfacial region by IRRAS and VSFG.

These results have implications for SSA aerosols. As salts are abundant in oceanic waters, it is likely that deprotonated fatty acids will remain near the surface of the aerosol. However, the organization and structure, particularly the packing density, likely differs between deprotonated and protonated species, as IRRAS and VSFG have shown that ionized molecules did not fully partition to the surface to form a monolayer. Increased salt concentration may increase partitioning of ionized species. A more in depth study of pH and background electrolyte concentration is needed. Furthermore, as a variety of surfactant species are found in aerosols, investigation of mixed monolayers as a function of pH would more accurately reflect the surface properties of SSA.

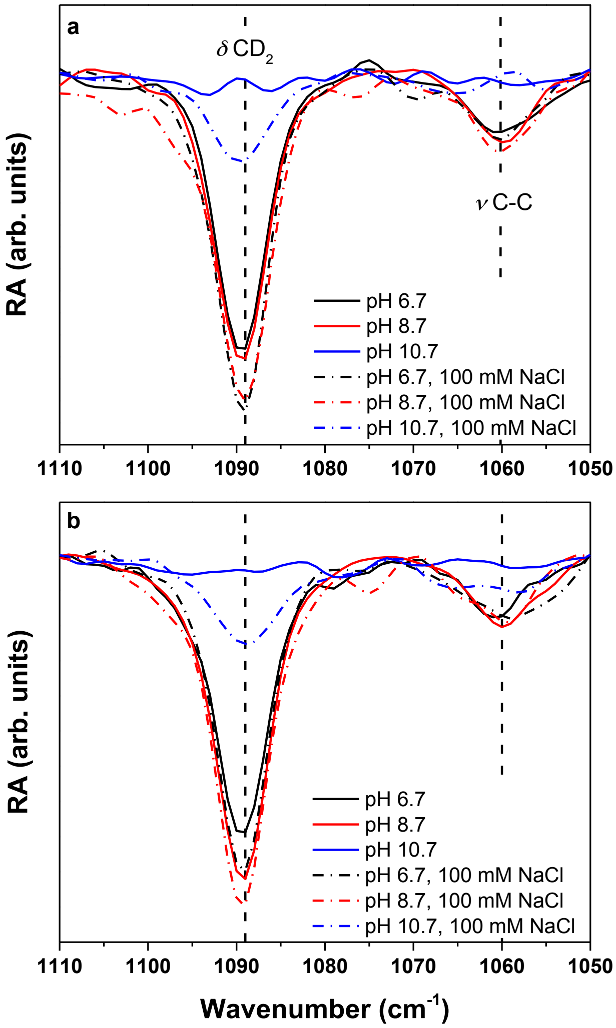

Figure 7.1. IRRAS spectra of the CD_2 scissoring region for d_{31}-PA monolayers on various pH solutions in (a) TC phase (24 Å^2/molecule and (b) UC phase (20.5 Å^2/molecule).

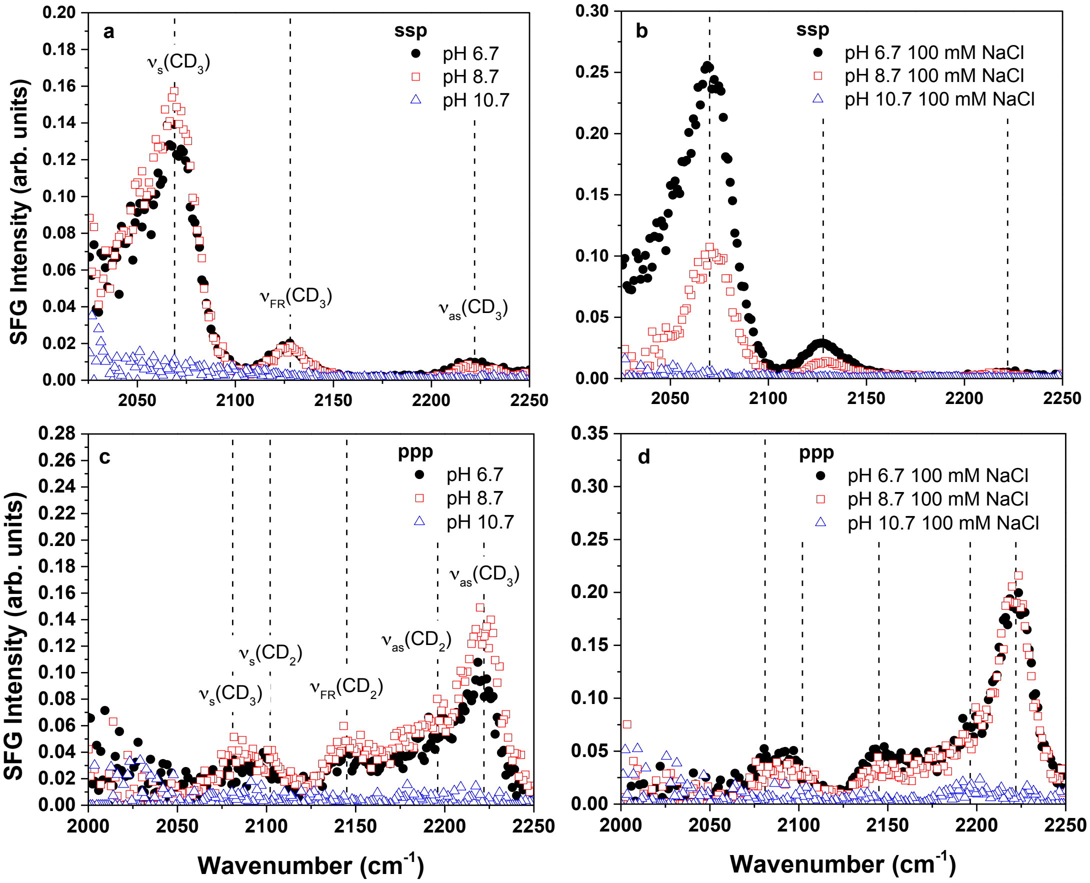

Figure 7.2. VSFG spectra of the CD stretching region for d_{31}-PA monolayers in the UC phase (20.5 Å^2/molecule) on various pH solutions in (a,c) *ssp* and (b,d) *ppp* polarizations.

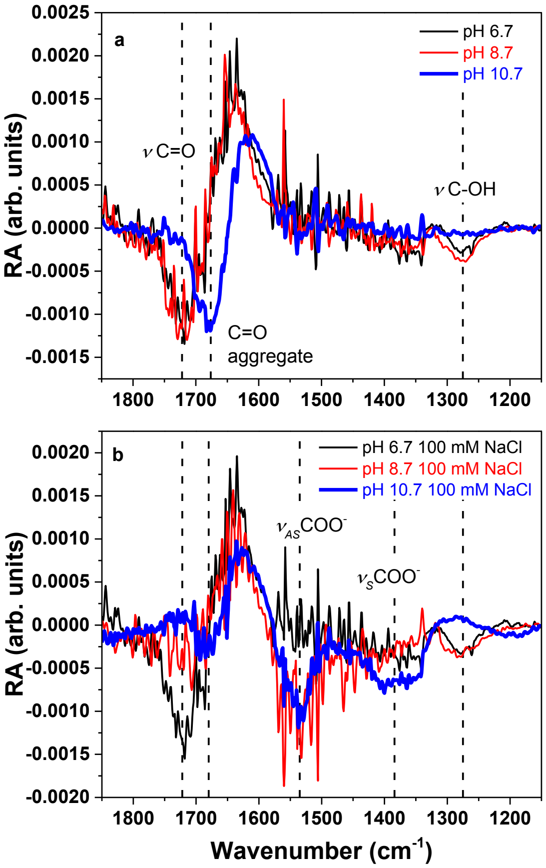

Figure 7.3. IRRAS spectra of the C=O and COO$^-$ region for d_{31}-PA monolayers in the UC phase (20.5 Å^2/molecule) on different pH solutions (a) without and (b) with 100 mM NaCl.

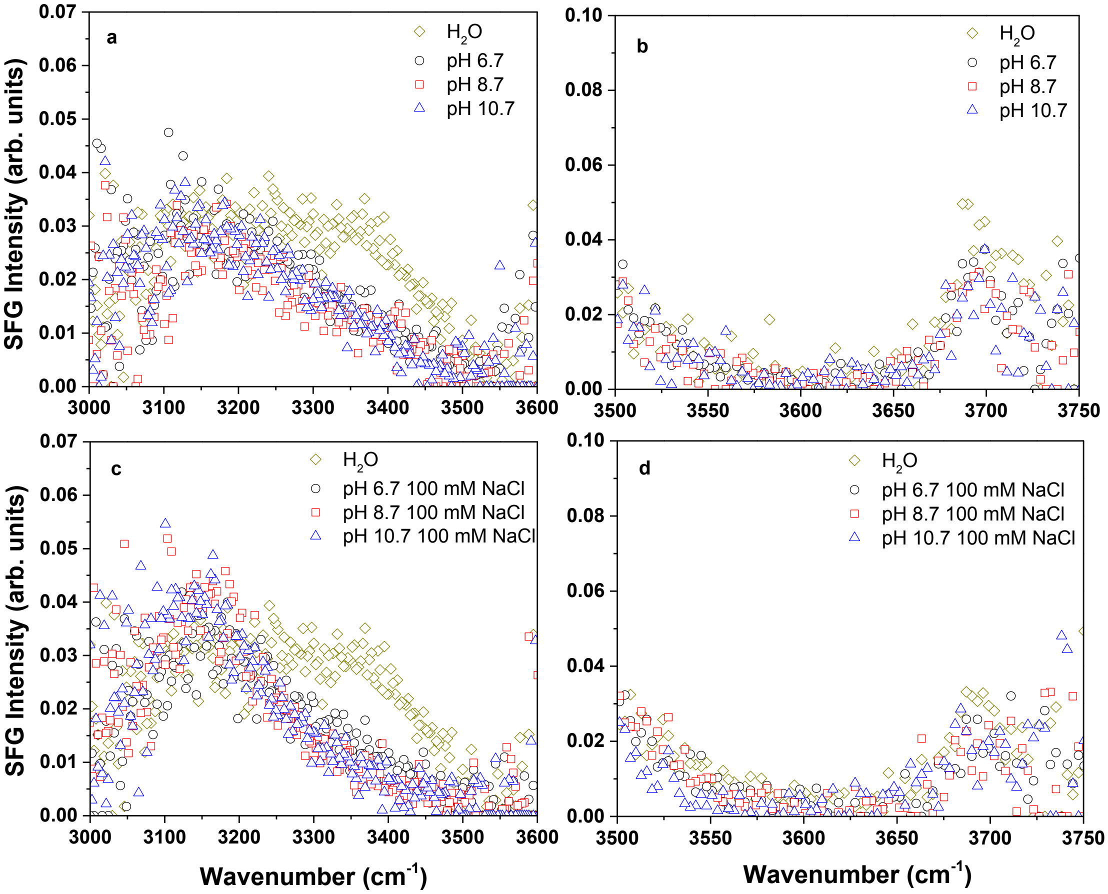

Figure 7.4. VSFG spectra in the OH region of pH solutions in absence (a,b) and presence of 100 mM NaCl (c,d). Every fourth data point is shown for convenience.

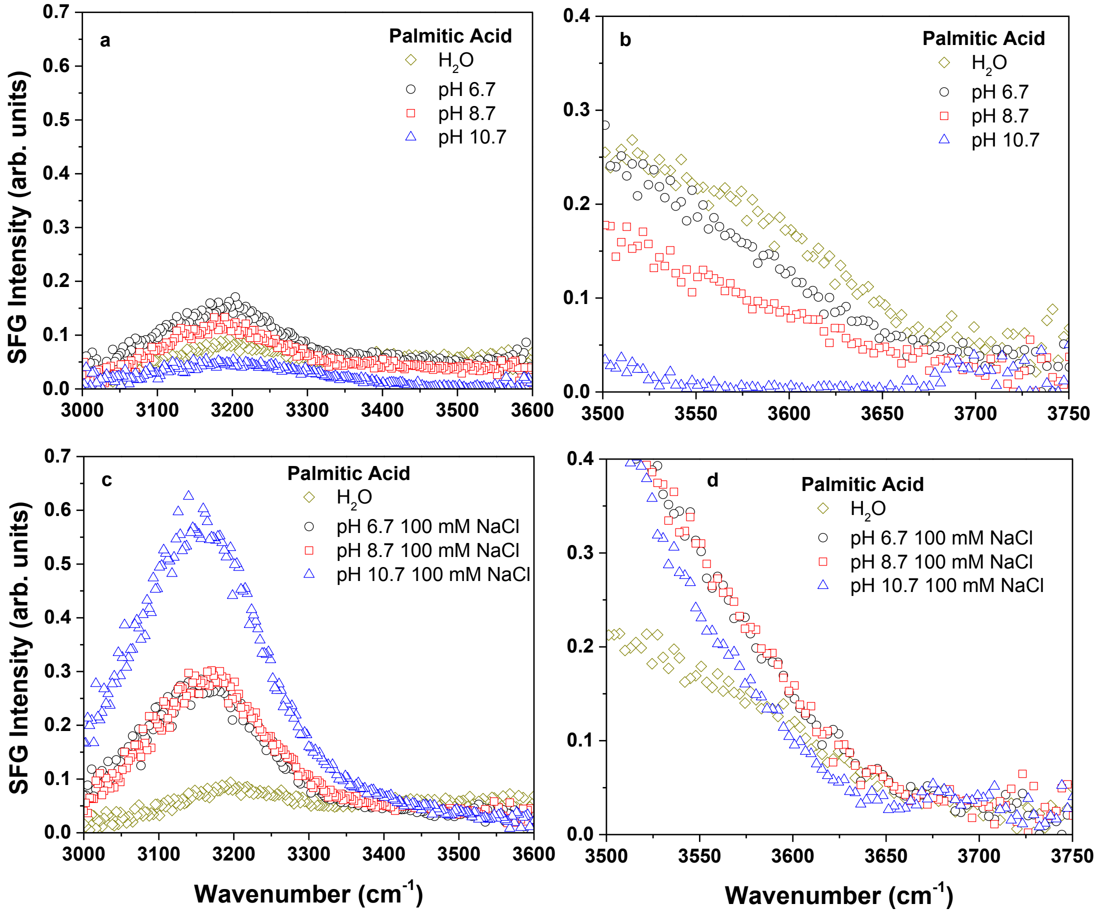

Figure 7.5. VSFG spectra in the OH region of d_{31}-PA monolayers on different pH solutions in the absence (a, b) and presence (c, d) of 100 mM NaCl. Every fourth data point is shown for convenience.

Table 7.1. Equilibrium spreading pressures of PA monolayers on pH-adjusted solutions with and without NaCl.

Solution pH	Π_{ESP} (mN/m)	
	H_2O	100 mM NaCl
6.7	7.57 ± 0.06	17.75 ± 0.94
8.7	7.59 ± 0.22	21.13 ± 0.29
10.7	42.27 ± 5.67	31.08 ± 3.28

Table 7.2. Calculated tilt angles of the terminal methyl group and alkyl chain of d_{31}-PA monolayers on different pH-adjusted solutions with and without 100 mM NaCl.

Solution	θ_{CD3}	θ_t
pH 6.7	8.4	28.6
pH 8.7	6.7	30.3
pH 6.7 100 mM NaCl	3.9	33.1
pH 8.7 100 mM NaCl	6.0	31.0

Chapter 8: Interfacial Properties of Avian Stratum Corneum Monolayers Investigated by Brewster Angle Microscopy and Vibrational Sum Frequency Generation Spectroscopy

8.1. Introduction.

The skin is an organ whose structure and function have been much investigated over the years. In particular, the stratum corneum (SC), the skin's outermost layer, is now well recognized as the physical barrier to the outside environment and is responsible for preventing excessive water loss from the body.[219–222] The SC is composed of dead cells also known as corneocytes embedded in a matrix of intercellular lipids.[44] Intercellular lipids control the diffusion of water vapor to the environment. Experiments have shown that removal of the SC lipids with organic solvents results in a significant increase in the skin total evaporative water loss (TEWL).[223–225] Intercellular lipids organize into layers of lamellae, the structure of these which is proposed to be bi- or trilayers.[226,227] It has been suggested that chemical composition influences the organization and structure of lipids in the SC.[227,228]

Cholesterol, free fatty acids, and ceramides make up the majority of SC lipids in mammals, with ceramides being the most abundant (~50%).[229] In humans, inhibition of the enzyme β-glucocerebrosidase results in the replacement of ceramide with its precursor cerebroside,[230] a ceramide with a glucose headgroup. This alteration results in an inability to maintain water within the skin,[231,232] which suggests that the organization of SC lipids, and the subsequent interaction of water with lipids, is strongly dependent upon lipid composition. Studies of avian SC have supported this notion, where it was found that cutaneous water loss (CWL) rates were linked to the relative proportion of lipid classes in lark species.[47,45,46] Ceramides and cerebrosides are the most abundant lipids in the SC of lark species from desert climates and were found to have a lower CWL rate than species from a mesic environment, which have a higher fraction of free fatty acids and triacylglycerols in their SC.[47,233] Studies of house sparrows revealed that distribution of lipids is not uniform throughout the SC, however. Depth profiling of the SC of house sparrows caught in the winter found that more polar lipids such as ceramide and cerebroside are more abundant in deeper layers of the SC, and are associated with higher water content.[234] Furthermore, CWL rates were observed to be lower in winter birds compared to summer birds.[234,235] These studies suggest that ceramides and cerebrosides play a role in the reduction of CWL rates. The ability of these lipids to form strong hydrogen-bonds with adjacent lipids or adjacent water molecules may inhibit water loss or sequester water within the SC.[66,47] While properties of ceramide and cerebroside have been investigated,[236,41] the intermolecular interactions between lipids in these complex systems and how this regulates CWL is not well understood.

In this study, Langmuir monolayers of SC lipids extracted from four lark species were investigated at the air-water interface. The interfacial properties of two desert lark species, the black-crowned finchlark and hoopoe lark, were compared to that of two mesic species, the horned lark and skylark, in an attempt to understand how the structure and organization of these lipid films correlates to the CWL. The phase behavior and stability of SC lipids were investigated by means of surface pressure-area isotherms. Imaging of monolayer domain morphology was assessed with Brewster angle microscopy. Ordering of SC alkyl chains (*gauche* vs. *trans* conformation) and interfacial water organization near the monolayer was probed with vibrational sum frequency generation (VSFG) spectroscopy. Results found here suggest that mesic lark species have a disordered lipid structure, which could account for their increased CWL. Desert species were observed to have disordered and ordered lipid structures depending on the species. The structure of water molecules near the monolayer was found to be related to the monolayer morphology, which suggests that lipid organization strongly influences the way in which water molecules interact with SC lipids.

8.2. Experimental.

8.2.1. Materials.

SC intercellular lipids from lark species were extracted and quantified by methods that have been previously described.[47,237,238] The relative abundance of each lipid class for the four species is provided in Table 8.1. Extracted lipids were then dissolved in ~100-300 µL of a 2:1 chloroform:methanol solution containing 50 mg/L butylated hydroxytoluene (BHT), an antioxidant. A diluted lipid solution of each lark species was prepared by suspending 10 µL of the stock lipid solution in 2 mL of solvent. Lipids solutions were stored at -20°C. Ultrapure water with a resistivity of ≥ 18.2 MΩ·cm and a measured pH of 5.6 was obtained from a Barnstead Nanopure Filtration system (model D4741, Barnstead/Thermolyne Corporation, United States).

8.2.2. Methods.

Surface Pressure-Area Isotherms

Surface pressure-area (Π-*A*) isotherms were conducted on a Teflon Langmuir minitrough (KSV, Finland) with a total surface area of 144 cm^2. Prior to experiments the trough was thoroughly cleaned with ethanol and ultrapure water. The Delrin-coated barriers were swept across the surface before every compression isotherm to ensure that a surface pressure ≥ 0.2 mN/m was not observed, which would be indicative of organic contaminants. Monolayers of the SC lipid extracts were prepared by drop-wise spreading of an appropriate volume of the lipid solution on the water surface with a glass microsyringe (Hamilton). As the total concentration of lipids was not consistent between bird species, the volume of lipid solution spread for each species varied. Volumes were chosen such that a gaseous (G) phase (surface pressure $\Pi \approx 0$ mN/m) existed after spreading and a minimum surface pressure of 20 mN/m was reached before the compression limit of the trough. The following volumes were spread: black-crowned finchlark, 25 μL; hoopoe lark, 50 μL; horned lark, 14 μL; skylark, 30 μL. After spreading, 20 min were allowed for solvent evaporation prior to film compression. Monolayers were compressed symmetrically at a constant rate of 5 mm/min/barrier until a limiting area of 35 cm^2 was reached. All experiments were conducted at room temperature (295 ± 1 K) and ambient pressure.

Brewster Angle Microscopy

Images of the SC monolayers were collected with a custom-built BAM system that has been previously described.[65] The BAM setup was described in Chapter 2. All experiments were conducted on a water and the Brewster angle was fixed at 53.1°. A movie of the monolayer compression was created by continuously collecting images at a frame rate of 4.85 s. Still frames were then extracted at appropriate surface pressures. Final images were cropped from the full 800 μm × 800 μm size to the most resolved region, which may differ between images. The scale bar is accurate for each individual image.

Vibrational Sum Frequency Generation Spectroscopy

VSFG spectra were collected with the BBSFG-1 system described in Chapter 2. Energy of the visible was fixed at 70 μJ per pulse for all measurements, while the IR beam had energies of 8 and 14 μJ in the OH (3000-3600 cm^{-1}) and CH (2800-3000 cm^{-1}) regions, respectively. Vertical binning of the CCD chip was done for measurements in the OH region to reduce background noise and cosmic radiation spikes. In the CH region, the full CCD chip was used, but a cosmic correct function was selected in the software (SpectraSense 5.0) to remove cosmic radiation spikes. Spectra were acquired for 5 and 2 min in the OH and CH regions, respectively. Both *ssp* (*s*-SFG, *s*-VIS, *p*-IR) and *ppp* polarization combinations were collected in the CH region, while only *ssp* spectra were collected in the OH region. Final spectra shown here are background-subtracted and normalized to the non-resonant profile of GaAs (110) (VI-II Inc.). Peak positions were calibrated by the non-resonant absorption spectrum of polystyrene.

8.3. Results and Discussion.

8.3.1. Phase Behavior of SC Lipids from Lark Species.

Figure 8.1 shows Π-*A* isotherms of SC lipid monolayers from black-crowned finchlark, hoopoe lark, horned lark, and skylark species. As can be seen, the phase behavior differs between the four lark species. All species, however, have a gas-liquid condensed (G-LC) coexistence region at 0 mN/m, as evidenced by BAM. The black-crowned finchlark transitions from the G-LC to the liquid condensed (LC) phase at 80 cm^2. The monolayer undergoes a phase transition at ~25 mN/m, evidenced by the kink in the isotherm, before reaching a maximum surface pressure of 28 mN/m. The hoopoe lark has a sharp transition from the G-LC to LC phase at 58 cm^2. Surface pressure rapidly increases from this point to a maximum value of 44 mN/m. The horned lark lifts off at ~85 cm^2 and reaches a maximum surface pressure of ~25 mN/m. The skylark begins increasing surface pressure at ~125 cm^2 and undergoes a phase transition at ~20 mN/m, and continues to increase to 35 mN/m until the compression limit is reached.

The phase behavior observed here indicates that there is no clear distinction in the monolayer properties between desert and mesic lark SC lipids. The black-crowned finchlark and hoopoe lark are both desert species, but the monolayers do not have similar phase behavior, despite having similar relative abundances of lipid classes (see Table 8.1). The hoopoe lark has a sharp transition to the LC phase and increases surface pressure quickly over a small area change, which would indicate that lipids in this monolayer have alkyl chains untilted with respect to the surface plane.[239] For the black-crowned finchlark the surface pressure increases slowly over a large area, consistent with a monolayer that is more fluid in nature.[30,240] A phase transition was observed in the LC phase, likely arising from a change in the orientation of alkyl chains from a tilted to untilted configuration or squeezing out of lipid components.[188,240] While these two species have similar abundances of lipid classes, it is possible that the degree of unsaturation in lipid chains varies within these classes between species, and could account for the difference in phase behavior observed here. For the mesic species studied here, horned lark and skylark, both monolayers displayed fluid-like behavior.

To further asses the physical state of the SC lipid extracts from the lark species, the isothermal compressibility modulus ($C_s^{-1} = -A_\Pi(\partial\Pi/\partial A_\Pi)_T$, where A_Π is the area at the corresponding Π) was calculated from the slopes of isotherms shown in Figure 8.1. The compressibility modulus is a measure of a monolayer's rigidity, in which a higher value corresponds to a more rigid monolayer. Compressibility modulus curves for the four lark species are presented in Figure 8.2. The black-crowned finchlark and horned lark have similar curves, with the compressibility modulus increasing to a maximum value of 30 mN/m, and then decreasing back towards 0 mN/m. The skylark increases to a maximum value of 50 mN/m at a surface pressure of 15 mN/m. A dip is observed at a surface pressure of 28 mN/m for the skylark curve, indicative of a phase transition. In the case of the hoopoe lark, the compressibility modulus increases with increasing surface pressure until a maximum value of 110 mN/m is reached at the maximum surface pressure of 44 mN/m. The compressibility modulus curves indicate that the hoopoe lark has the most rigid monolayer, followed by the skylark, and lastly the black-crowned finchlark and horned lark. It should be noted that the maximum compressibility modulus values observed for these monolayers are relatively small compared to values obtained for single-component monolayers. For instance, a pure cholesterol monolayer has maximum value of 600 mN/m,[104] while that of a pure tristearin monolayer is 1000 mN/m.[241] This suggests that the monolayers formed from these SC lipid extracts are significantly more fluid than the pure components they consist of.

Stability of the skylark and hoopoe lark monolayers was investigated by compression-expansion cycles, as shown in Figure 8.3. The compression and expansion rates were both set to 5 mm/min/barrier. For both monolayers, it can be seen that the second compression-expansion cycle is nearly identical to the first, indicating that hysteresis of the monolayers did not occur. The second compression is shifted to a smaller area for both species due to loss of film material to the subphase. The change in area is greater for the skylark (30 cm^2) than the hoopoe lark (5 cm^2), which could suggest that the hoopoe lark monolayer is more stable.

8.3.2. Surface Morphology of SC Lipid Monolayers of Lark Species.

BAM images of black-crowned finchlark, hoopoe lark, horned lark, and skylark monolayers during film compression are shown in Figure 8.4. In all images shown, dark blue or black represent water-rich or lipid-poor regions, bright blue represents lipid-rich regions, and white represents the formation of three-dimensional (3D) structures. For the black-crowned finchlark monolayer, small round lipid domains are observed at 0 mN/m, indicative of a G-LC phase. As the monolayer is compressed to higher surface pressures, a porous monolayer forms. At 25 mN/m, the point at which a phase transition was observed in the isotherm, round lipid domains can be observed within the monolayer, revealing that a phase separation of monolayer components has occurred.[188] This suggests that components of the black-crowned finchlark monolayer are not miscible at higher surface pressures.

In the case of the hoopoe lark, large lipid sheets are observed at 0 mN/m. With increasing surface pressure a homogeneous film forms. The intensity of the reflected light increases with surface pressure, which may be due to an increase in the monolayer thickness.[79] The morphology observed for the hoopoe lark is similar to that of pure ceramide and cerebroside monolayers.[66,242] Similar to isotherms, a comparison of hoopoe lark to black-crowned finchlark, shows that morphology of these two desert species is distinctly different despite lipid classes having similar relative abundances. A more detailed analysis on the degree of unsaturation of alkyl chains within each class is needed to determine if this contributes to the differences observed here.

At 0 mN/m, the horned lark SC lipid extract shows round lipid domains co-existing with larger lipid sheets. Upon further compression, an inhomogeneous monolayer forms. At times, inhomogeneous lipid sheets with 3D structures are observed (5 and 20 mN/m), but other structures are observed, which include round lipid domains within a homogeneous film (10 mN/m). Images of the horned lark monolayer indicate that components are not miscible, as several different morphologies are observed throughout compression.

For the skylark monolayer, a porous monolayer is observed at 0 mN/m. The porous morphology is maintained with increasing surface pressure until the monolayer undergoes a phase transition at 22 mN/m. After this point the image becomes intensely bright, and small 3D structures begin to form, which indicates that collapse of the monolayer has begun. This morphology persists until the compression was stopped. The formation of collapse structures could account for the large loss of material observed in compression-expansion cycles.

8.3.3. Alkyl Chain Conformation.

Figure 8.5 shows VSFG spectra of the hoopoe lark SC lipid monolayer at 10 mN/m in *ssp* and *ppp* polarizations in the CH region. In the *ssp* spectra, three peaks are observed, corresponding to the CH_2 symmetric stretch ($\nu_s(CH_2)$), CH_3 symmetric stretch ($\nu_s(CH_3)$), and CH_3 Fermi resonance ($\nu_{FR}(CH_3)$) at 2834, 2860, and 2929 cm^{-1}, respectively. In addition to the $\nu_s(CH_2)$ and $\nu_s(CH_3)$ vibrational modes, the CH_2 asymmetric stretch ($\nu_{as}(CH_2)$) and CH_3 asymmetric stretch ($\nu_{as}(CH_3)$) are observed in the *ppp* spectra at 2882 and 2945 cm^{-1}, respectively. Based on the electric dipole approximation, SFG does not occur for molecules containing centrosymmetry. As methylene groups contain an inversion center, peaks corresponding to these modes should not be observed if the alkyl chain has a nearly *trans* configuration. From Figure 8.5a, it can be seen that in the *ssp* spectra the $\nu_s(CH_3)$ mode is more intense than the $\nu_s(CH_2)$ mode, indicating that the chain is well ordered. This is confirmed in the *ppp* spectra, in which the $\nu_{as}(CH_3)$ mode is significantly more intense than the $\nu_{as}(CH_2)$ mode.

The CH spectra in *ssp* polarization for black-crowned finchlark, hoopoe lark, horned lark, and skylark SC lipid monolayers at various surface pressures are shown in Figure 8.6. It can be seen for the black-crowned finchlark, horned lark, and skylark, that the

$\nu_s(CH_2)$ mode is significantly more intense than the $\nu_s(CH_3)$ for surface pressures lower than 10 mN/m. At 20 mN/m the two peaks are about equal intensities, and at 30 mN/m the $\nu_s(CH_3)$ mode becomes more intense than the $\nu_s(CH_2)$ mode. This indicates that alkyl chains for these three species are disordered until a surface pressure of 20 mN/m is reached. In the case of the hoopoe lark, the $\nu_s(CH_3)$ mode is always more intense than the $\nu_s(CH_2)$ mode, independent of surface pressure, indicating the alkyl chain are well ordered, even at low surface pressures. Relative ordering of the alkyl chains can be determined from the intensity ratio $I(\nu_s(CH_3))/I(\nu_s(CH_2))$, with a higher value corresponding to more *trans* bonds in the alkyl chain. $I(\nu_s(CH_3))/I(\nu_s(CH_2))$ as a function of surface pressure is shown in Figure 8.7 for all four species. The black-crowned finchlark and skylark have similar ratio values at all surface pressures, and the horned lark has slightly higher values relative to these two. The hoopoe lark has a significantly higher value than the other three species. For all species, however, it can be seen that ordering of the chain increases with increasing surface pressure. These results indicate that ordering of the alkyl chains in the SC lipids depends upon the surface pressure, and that significant gauche defects occur in the chains below 20 mN/m, except in the case of the hoopoe lark.

8.3.4. Interfacial Water Organization near SC Lipid Monolayers of Lark Species.

Figure 8.8 shows *ssp* spectra of the interfacial water structure of black-crowned finchlark, hoopoe lark, horned lark, and skylark monolayers at various surface pressures. In the case of pure water, three features are typically observed at 3200, 3400, and 3700 cm^{-1}.[146] The bands at 3200 and 3400 cm^{-1} correspond to the strongly and weakly hydrogen-bonded water molecules in the subsurface region,[147,148] while the narrow band at 3700 cm^{-1} is attributed to free OH groups of topmost water molecules.[146,157] Due to limitations in the spectral bandwidth (~600 cm^{-1}), only the bands at 3200 and 3400 cm^{-1} are observed here.

All lark species, with the exception of the horned lark, show an enhancement in the observed intensity of 3200 and 3400 cm^{-1} bands relative to the neat air-water interface when the monolayer surface pressure is greater than 0 mN/m. Enhancement of the SFG signal can happen from increased alignment of water molecules perpendicular to the interface plane or an increase in the depth probed.[156,243] Studies of model phospholipid membranes have similarly shown enhancement of water structure, which is generally attributed to the electric field generated at the interface by the charged headgroups.[156,244–246] Only a small fraction of the monolayer is likely charged for monolayers studied here; the carboxylic acid headgroup of fatty acids are the only ionizable group at this pH (~6), and studies have shown that the interfacial pKa of fatty acids (~8-10) is much higher than the reported bulk value (~5).[192,196]

Relative enhancement of the 3200 and 3400 cm^{-1} bands appears to depend on the chemical composition of the SC monolayer, as no distinct trend is observed between the four lark species. In the case of black-crowned finchlark and skylark, an enhancement of both the 3200 and 3400 cm^{-1} peaks occurs once the monolayer has a surface pressure greater than 0 mN/m. The intensity of the 3200 cm^{-1} band remains constant, but the 3400 cm^{-1} band enhancement becomes more intense with increasing surface pressure. Furthermore, for skylark, there appears to be a band forming at ~3500-3550 cm^{-1} that is more intense than the 3200 cm^{-1} band when the surface pressure is ≥ 20 mN/m. Increased intensity from weakly hydrogen-bonded (less coordinated) water molecules could reflect increased solvation or hydrogen-bonding of interfacial water to the lipid headgroups, leading to a disruption in the hydrogen-bonding network of water molecules.

Water structure of the hoopoe lark SC monolayers is unaffected by surface pressure (after compressing to a value greater than 0 mN/m). Enhancement of the 3200 and 3400 cm^{-1} bands occurs, with 3200 cm^{-1} band more intense. This indicates that water molecules are more ordered (strongly hydrogen-bonded) near this monolayer.

As mentioned earlier, the horned lark SC monolayer has little enhancement compared to the other lark species. At 10 mN/m a slight enhancement of the 3200 cm^{-1} band occurs, along with suppression of the 3400 cm^{-1} band. An increase in surface pressure results in a slight decrease in intensity of the 3200 cm^{-1} band. These small perturbations suggest that the interfacial water hydrogen-bonding is not significantly impacted by the horned lark monolayer.

8.4. Conclusions.

Here the interfacial properties of SC lipid monolayers from desert and mesic lark species were investigated and compared to understand CWL rates in larks. Results indicate that lipids of mesic species form fluid monolayers in which components are not miscible and had significant *gauche* defects in the alkyl chains. In contrast, desert species did not display similar properties despite having similar lipid composition; the black-crowned finchlark exhibited behavior similar to the mesic species while the hoopoe lark was found to form a rigid, miscible monolayer in which lipid chains had a *trans* configuration. Interfacial water hydrogen-bonding was correlated to monolayer morphology. Species that exhibited porous monolayer structure had an increase in weakly hydrogen-bonded water molecules, while condensed monolayers had a higher intensity of strongly hydrogen-bonded water molecules. In general, SC lipids from mesic species were less ordered, which could explain their increased CWL. A clear trend was not observed for desert species, however. Investigation of more lark species than probed here could shed more light on the relationship of CWL and lipid structure. Furthermore, studies done at physiological temperatures would reflect the lipid structure of living birds more accurately.

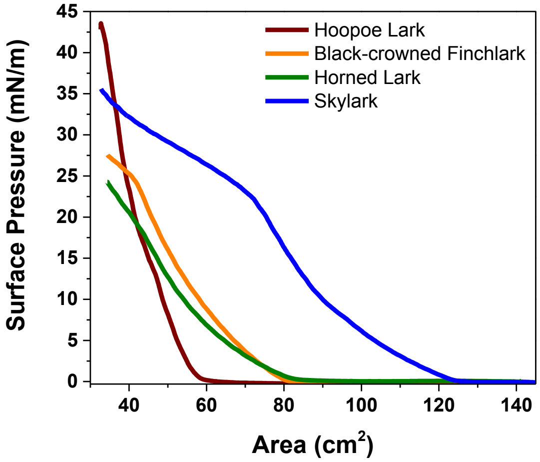

Figure 8.1. Π–*A* isotherms of SC lipid monolayers from black-crowned finchlark, hoopoe lark, horned lark, and skylark species.

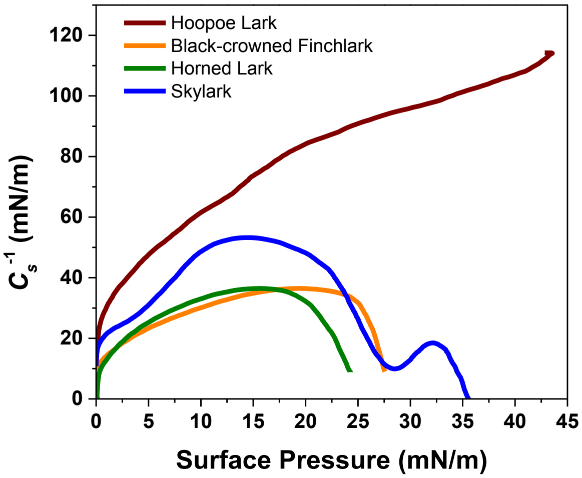

Figure 8.2. Compressibility modulus of SC lipid monolayers of lark species as a function of surface pressure. The hoopoe lark monolayer is the most rigid of the four species.

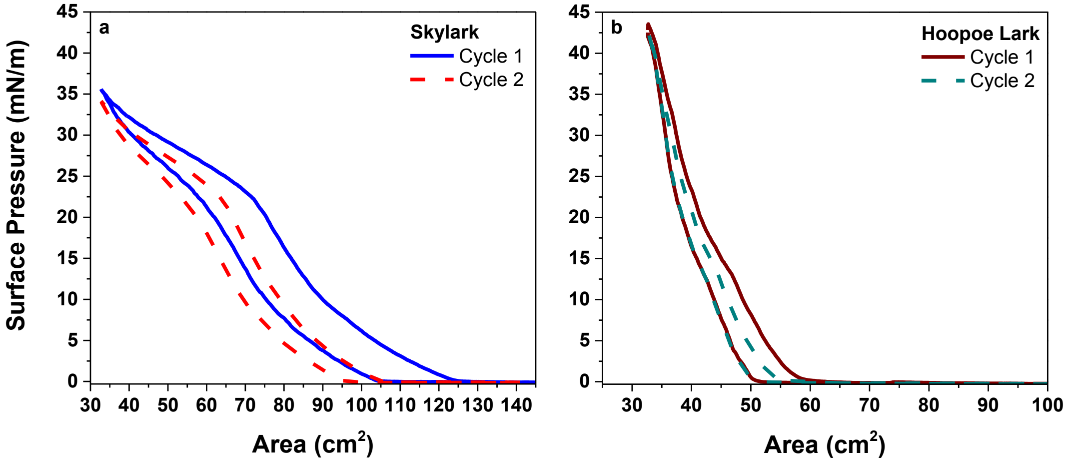

Figure 8.3. Compression-expansion isotherms of SC lipid monolayers of (a) skylark and (b) hoopoe lark. No hysteresis was observed.

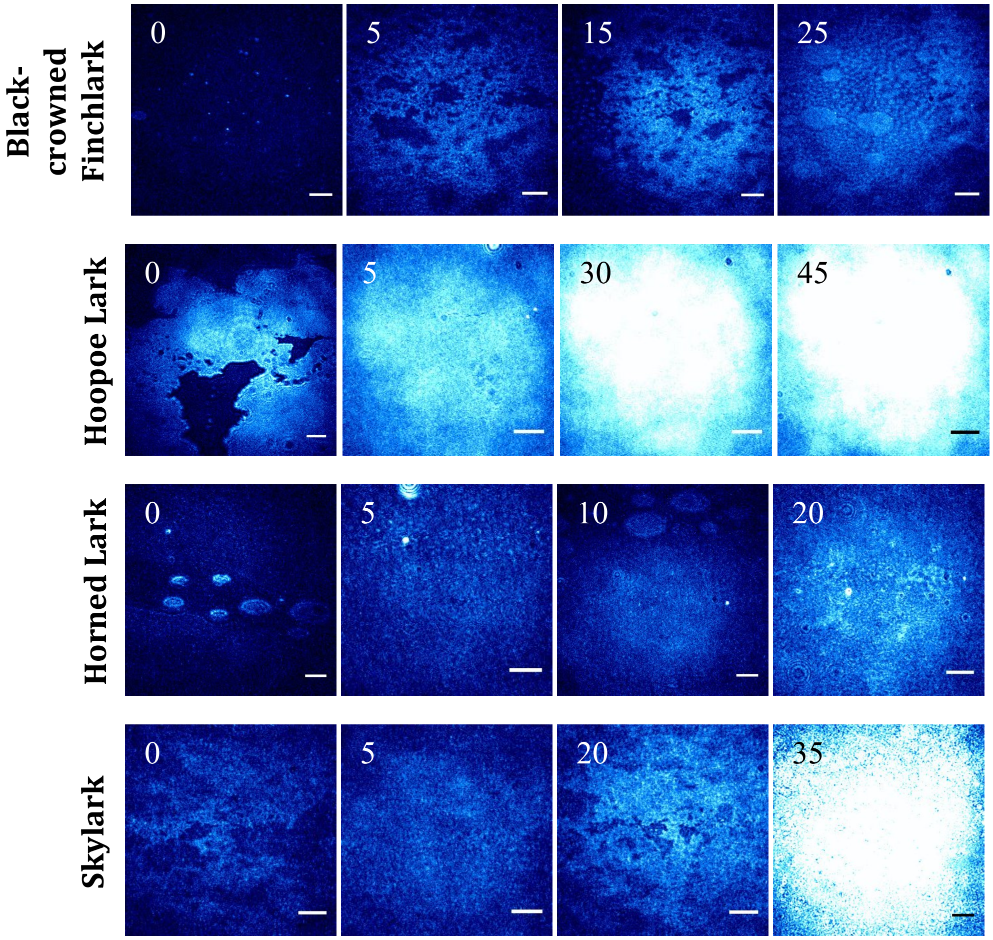

Figure 8.4. BAM images of black-crowned finchlark, hoopoe lark, horned lark, and skylark SC lipid monolayers at various surface pressures during film compression. Scale bars are 50 μm for each image. The surface pressure is indicated in the top left corner of the respective image.

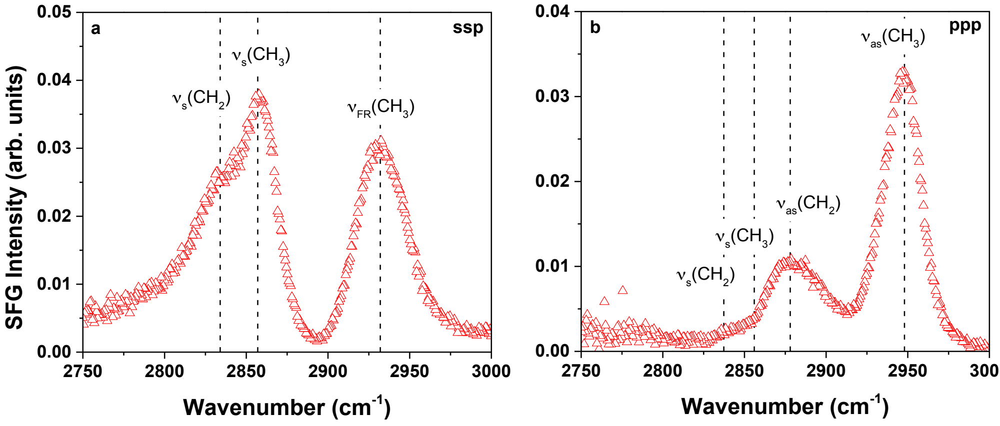

Figure 8.5. VSFG spectra of hoopoe lark SC lipid monolayer at 10 mN/m in the CH region for (a) *ssp* and (b) *ppp* polarization combinations.

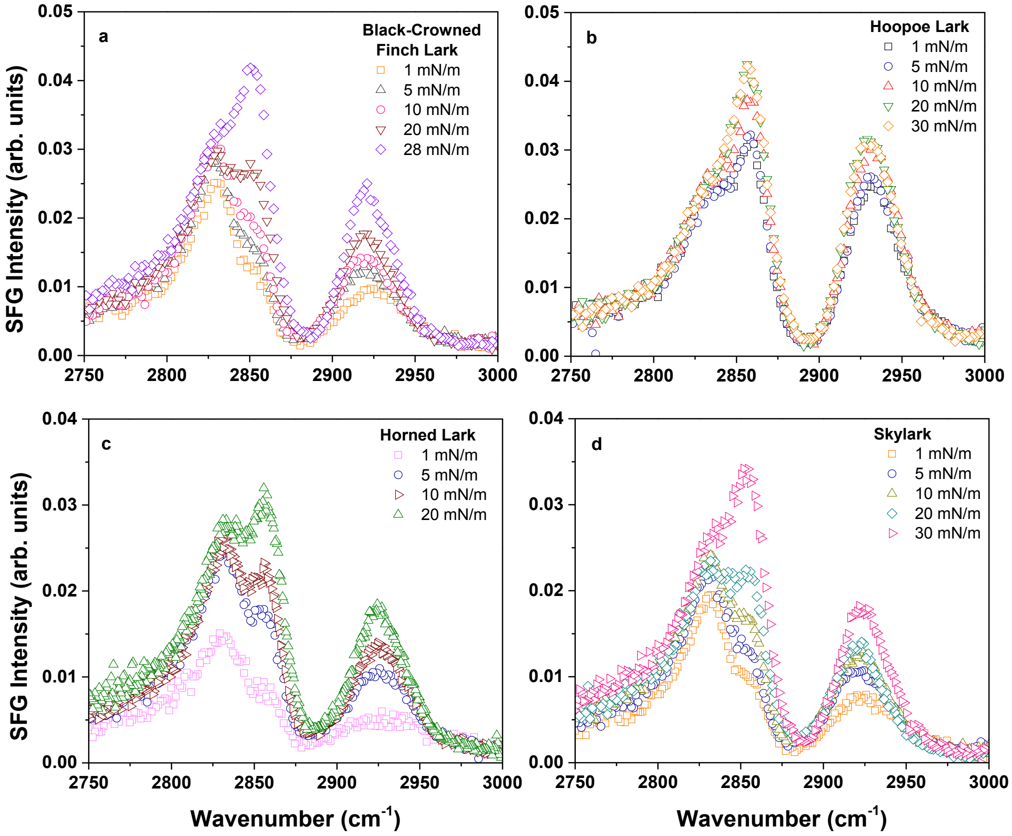

Figure 8.6. VSFG in the CH region with increasing surface pressure for SC lipid monolayers of (a) black-crowned finchlark (b) hoopoe lark (c) horned lark and (d) skylark

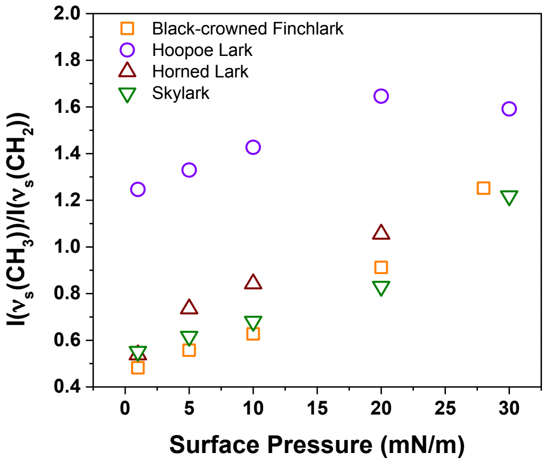

Figure 8.7. Intensity ratio $I(\nu_s(\mathrm{CH_3}))/I(\nu_s(\mathrm{CH_2}))$ as a function of surface pressure for SC lipid monolayers of the four lark species.

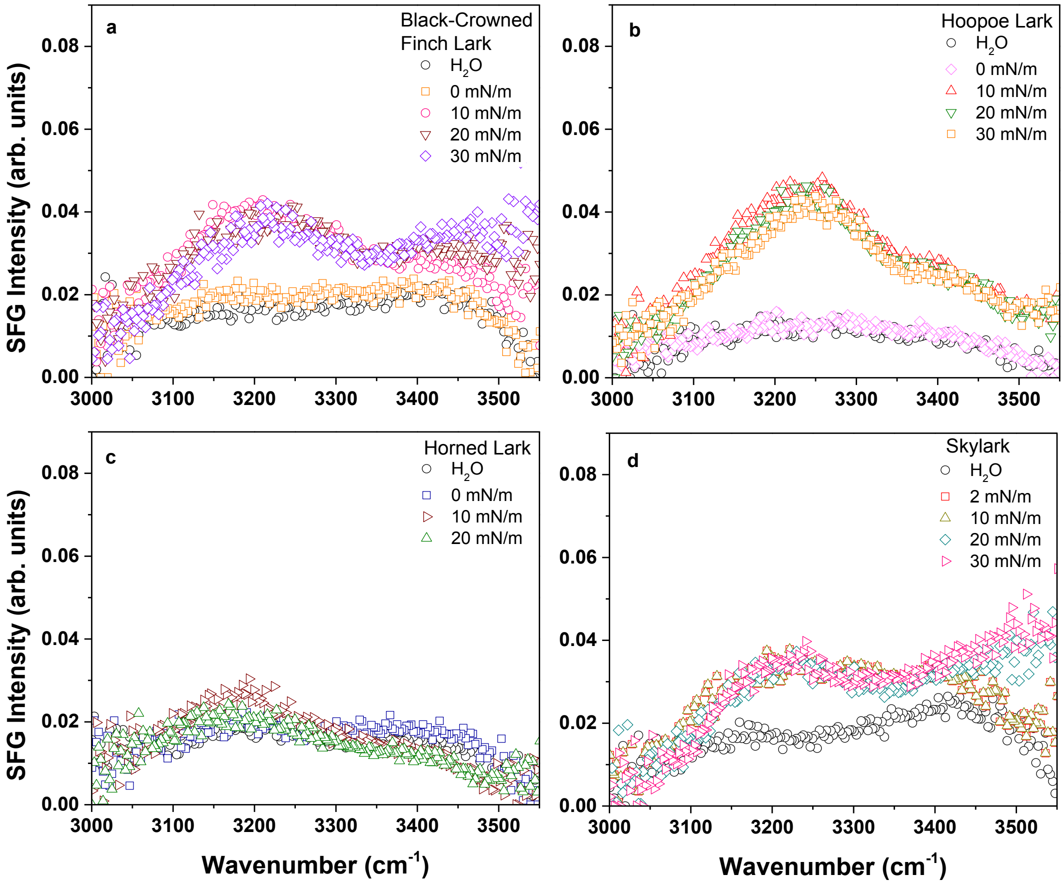

Figure 8.8. VSFG spectra in the OH region with increasing surface pressure for SC lipid monolayers of (a) black-crowned finchlark (b) hoopoe lark (c) horned lark and (d) skylark. Every fourth data point is shown for convenience.

Table 8.1. Relative abundance of lipid classes in the SC of four lark species. Values calculated from data provided in Champagne, et al. *J. Exp. Biol.* **2012**, *215*, 4299–4307.

Lipid	Black-Crowned Finchlark	Hoopoe Lark	Horned Lark	Skylark
Cholesterol Ester	10.86	11.69	2.80	5.98
Fatty Acid Methyl Ester	3.76	5.08	53.71	4.62
Triacylglycerol	11.47	13.53	6.05	31.10
Free Fatty Acid	15.92	14.61	4.39	30.33
Cholesterol	3.81	3.75	2.67	4.12
Ceramide I	2.47	2.10	1.81	2.26
Ceramide II	3.68	4.70	0.86	0.00
Ceramide III	14.11	13.09	14.10	8.96
Total Ceramide	20.25	19.89	16.78	11.23
Cerebroside	33.92	31.45	13.59	12.63

Chapter 9: Atmospheric and Biological Implications

Work presented in this dissertation is motivated by a growing interest in the molecular level organization and structure of atmospheric and biological interfaces. To gain insight into these interfaces the spectroscopic techniques Brewster angle microscopy (BAM), infrared reflection-absorption spectroscopy (IRRAS), and vibrational sum frequency generation (VSFG) spectroscopy were utilized to probe lipid monolayers at air-aqueous interfaces. A variety of lipid-aqueous systems were investigated here and the findings in each study are applicable to both sea spray aerosols (SSA) and biomembranes.

A model phospholipid, dipalmitoylphosphatidylcholine (DPPC), on concentrated salts solutions was investigated as a proxy for organic coated SSA in which ions are enriched. Enrichment of ions is thought to occur due to complexation with lipid molecules. For the six cations studied here, binding affinity with the PC headgroup was found to have the following trend: $Zn^{2+} > Ca^{2+} > Mg^{2+} > Na^{+} \approx K^{+} > Sr^{2+}$. This trend is consistent with calculated enrichment factors, where Zn^{2+} had the highest enrichment and Sr^{2+} was depleted in SSA. This result implies that enrichment (or depletion) of inorganic ions in aerosols is a consequence of their interaction with surface-active organic molecules. Furthermore, surface properties of the DPPC monolayer were altered on the concentrated salt solutions, and have implications for aerosols and biomembranes. Diffusion of water, uptake of gases, and transport of small molecules are all influenced by morphology of organic films. Here, the packing density of DPPC molecules and surface morphology were impacted, the extent of which depended on cation identity and concentration. This indicates that the rate of processes such as diffusion will be altered depending on the relative abundance of different cations. Refractive index of the DPPC monolayer was found to decrease with increasing salt concentration, which implies that optical properties of aerosols (scattering and absorption of light) will change when ions are enriched in SSA. The presence of cations was also found to perturb the hydrogen-bonding network of water near the DPPC monolayer. At high Zn^{2+} concentrations water molecules reorganize to preferentially solvate the PC-Zn^{2+} complex, resulting in a reduced hydrogen-bonding network. Exchange of water with the vapor phase is likely reduced as a result. Similarly, diffusion of water molecules through biomembranes is also likely reduced as a consequence.

Another proxy system of organic coated SSA investigated here includes glycolipids. In this study the hydrogen-bonding network and depth of interface were found to differ for soluble and insoluble glycolipids. This has implications for the growth, adsorption, and chemical reactivity of particles.

The impact of pH on a model free fatty acid, palmitic acid, was also investigated. Here, dissolution of lipid molecules into bulk solution was observed at high pH. Addition of NaCl to solution increased surface propensity of lipids, but did not restore a full monolayer. Uptake of water and other gaseous species, and hence size and optical properties of aerosols, are influenced by organization of organic films. The hygroscopicity and chemical reactivity of acidic and basic particles are likely different as a result.

While seemingly unrelated to aerosols, avian stratum corneum lipid monolayers can also be considered as a proxy for organic coated SSA in which the organic film is chemically diverse. Lipid composition was found to impact surface morphology and interfacial water organization. As SSA are chemically complex entities, these results imply that small changes in relative abundance species has the ability to modify many properties, including evaporation of water, uptake of gases, and albedo. Furthermore, these results have implications for biomembranes, as permeation of water is related to the formation of channels within the membrane.

References

(1) Climate Change the Physical Science Basis. ICCP 2007.

(2) Jacobson, M. Z. Global Direct Radiative Forcing due to Multicomponent Anthropogenic and Natural Aerosols. *J. Geophys. Res.* **2001**, *106* (D2), 1551–1568.

(3) Finlayson-Pitts, B. J.; Pitts, Jr., J. N. *Chemistry of the Upper and Lower Atmosphere*; Academic Press: San Diego, 2000.

(4) Ellison, G. B.; Tuck, A. F.; Vaida, V. Atmospheric Processing of Organic Aerosols. *J. Geophys. Res.* **1999**, *104* (D9), 11633–11641.

(5) Tervahattu, H.; Hartonen, K.; Kerminen, V.; Kupiainen, K.; Aarnio, P.; Koskentalo, T.; Tuck, A. F.; Vaida, V. New Evidence of an Organic Layer on Marine Aerosols. *J. Geophys. Res.* **2002**, *107* (D7), AAC 1-1.

(6) Tervahattu, H.; Juhanoja, J.; Kupiainen, K. Identification of an Organic Coating on Marine Aerosol Particles by TOF-SIMS. *J. Geophys. Res.* **2002**, *107* (D16), ACH 18-1.

(7) Ault, A. P.; Moffet, R. C.; Baltrusaitis, J.; Collins, D. B.; Ruppel, M. J.; Cuadra-Rodriguez, L. A.; Zhao, D.; Guasco, T. L.; Ebben, C. J.; Geiger, F. M.; et al. Size-Dependent Changes in Sea Spray Aerosol Composition and Properties with Different Seawater Conditions. *Environ. Sci. Technol.* **2013**, *47* (11), 5603–5612.

(8) Donaldson, D. J.; Vaida, V. The Influence of Organic Films at the Air-Aqueous Boundary on Atmospheric Processes. *Chem. Rev.* **2006**, *106* (4), 1445–1461.

(9) Garland, R. M.; Wise, M. E.; Beaver, M. R.; Dewitt, H. L.; Aiken, A. C.; Jimenez, J. L.; Tolbert, M. A. Impact of Palmitic Acid Coating on the Water Uptake and Loss of Ammonium Sulfate Particles. *Atmos. Chem. Phys.* **2005**, *5* (7), 1951–1961.

(10) McNeill, V. F.; Yatavelli, R. L. N.; Thornton, J. A.; Stipe, C. B.; Landgrebe, O. Heterogeneous OH Oxidation of Palmitic Acid in Single Component and Internally Mixed Aerosol Particles: Vaporization and the Role of Particle Phase. *Atmos. Chem. Phys.* **2008**, *8* (17), 5465–5476.

(11) Demott, P. J.; Prenni, A. J.; Liu, X.; Kreidenwies, S. M.; Petters, M. D.; Twohy, C. H.; Richardson, M. S.; Eidhammer, T.; Rogers, D. C. Predicting Global Atmospheric Ice Nuclei Distributions and Their Impacts on Climate. *Proc. Natl. Acad. Sci. U. S. A.* **2010**, *107* (25), 11217–11222.

(12) Li, Y.; Ezell, M. J.; Finlayson-Pitts, B. J. The Impact of Organic Coatings on Light Scattering by Sodium Chloride Particles. *Atmos. Environ.* **2011**, *45* (25), 4123–4132.

(13) Dilbeck, C. W.; Finlayson-Pitts, B. J. Hydroxyl Radical Oxidation of Phospholipid-Coated NaCl Particles. *Phys. Chem. Chem. Phys.* **2013**, *15* (24), 9833.

(14) Farmer, D.K.; Cappa, Christopher D.; Kreidenweis, S. M. Atmospheric Processes and Their Controlling Influence on Cloud Condensation Nuclei Activity. *Chem. Rev.* **2015**, *115* (10), 4199–4217.

(15) Forestieri, S. D.; Cornwell, G. C.; Helgestad, T. M.; Moore, K. A.; Lee, C.; Novak, G. A.; Sultana, C. M.; Wang, X.; Bertram, T. H.; Prather, K. A.; et al. Linking Variations in Sea Spray Aerosol Particle Hygroscopicity to Composition during Two Microcosm Experiments. *Atmos. Chem. Phys.* **2016**, *16* (9), 9003–9018.

(16) Cochran, R. E.; Jayarathne, T.; Stone, E. A.; Grassian, V. H. Selectivity Across the Interface: A Test of Surface Activity in Composition of Organic-Enriched Aerosols from Bubble Bursting. *J. Phys. Chem. Lett.* **2016**, *7*, 1692–1696.

(17) O'Dowd, C. D.; Facchini, M. C.; Cavalli, F.; Ceburnis, D.; Mircea, M.; Decesari, S.; Fuzzi, S.; Yoon, Y. J.; Putaud, J.-P. Biogenically Driven Organic Contribution to Marine Aerosol. *Nature* **2004**, *431*, 676–680.

(18) Facchini, M. C.; Rinaldi, M.; Decesari, S.; Carbone, C.; Finessi, E.; Mircea, M.; Fuzzi, S.; Ceburnis, D.; Flanagan, R.; Nilsson, E. D.; et al. Primary Submicron Marine Aerosol Dominated by Insoluble Organic Colloids and Aggregates. *Geophys. Res. Lett.* **2008**, *35* (17), L17814.

(19) Brandsma, J.; Hopmans, E. C.; Brussaard, C. P. D.; Witte, H. J.; Schouten, S.; Sinninghe Damste, J. S. Spatial Distribution of Intact Polar Lipids in North Sea Surface Waters: Relationship with Environmental Conditions and Microbial Community Composition. *Limnol. Oceanogr.* **2012**, *57* (4), 959–973.

(20) Jayarathne, T.; Sultana, C. M.; Lee, C.; Malfatti, F.; Cox, J. L.; Pendergraft, M. A.; Moore, K. A.; Azam, F.; Tivanski, A. V.; Cappa, C. D.; et al. Enrichment of Saccharides and Divlaent Cations in Sea Spray Aerosol During Two Phytoplankton Bloom. *Environ. Sci. Technol.* **2016**, *50* (21), 11511–11520.

(21) Prather, K. A.; Bertram, T. H.; Grassian, V. H.; Deane, G. B.; Stokes, M. D.; Demott, P. J.; Aluwihare, L. I.; Palenik, B. P.; Azam, F.; Seinfeld, J. H.; et al. Bringing the Ocean into the Laboratory to Probe the Chemical Complexity of Sea Spray Aerosol. *Proc. Natl. Acad. Sci. U. S. A.* **2013**, *110* (19), 7550–7555.

(22) Guasco, T. L.; Cuadra-Rodriguez, L. A.; Pedler, B. E.; Ault, A. P.; Collins, D. B.; Zhao, D.; Kim, M. J.; Ruppel, M. J.; Wilson, S. C.; Pomeroy, R. S.; et al. Transition Metal Associations with Primary Biological Particles in Sea Spray Aerosol Generated in Wave Channel. *Environ. Sci. Technol.* **2014**, *48* (2), 1324–1333.

(23) Wang, X.; Sultana, C. M.; Trueblood, J.; Hill, T. C. J.; Malfatti, F.; Lee, C.; Laskina, O.; Moore, K. A.; Beall, C. M.; McCluskey, C. S.; et al. Microbial Control of Sea Spray Aerosol Composition: A Tale of Two Blooms. *ACS Cent. Sci.* **2015**, *1* (3), 124–131.

(24) Quinn, P. K.; Collins, D. B.; Grassian, V. H.; Prather, K. A.; Bates, T. S. Chemistry and Related Properties of Freshly Emitted Sea Spray Aerosol. *Chem. Rev.* **2015**, *115* (10), 4383–4399.

(25) Cochran, R. E.; Laskina, O.; Jayarathne, T.; Laskin, A.; Laskin, J.; Lin, P.; Sultana, C. M.; Lee, C.; Moore, K. A.; Cappa, C. D.; et al. Analysis of Organic Anionic Surfactants in Fine and Coarse Fractions of Freshly Emitted Sea Spray Aerosol. *Environ. Sci. Technol.* **2016**, *50* (5), 2477–2486.

(26) Collins, D. B.; Zhao, D. F.; Ruppel, M. J.; Laskina, O.; Grandquist, J. R.; Modini, R. L.; Stokes, M. D.; Russell, L. M.; Bertram, T. H.; Grassian, V. H.; et al. Direct Aerosol Chemical Composition Measurements to Evaluate the Physicochemical Differences between Controlled Sea Spray Aerosol Generation Schemes. *Atmos. Meas. Tech.* **2014**, *7* (11), 3667–3683.

(27) Tang, C. Y.; Allen, H. C. Ionic Binding of Na^+ versus K^+ to the Carboxylic Acid Headgroup of Palmitic Acid Monolayers Studied by Vibrational Sum Frequency Generation Spectroscopy. *J. Phys. Chem. A* **2009**, *113* (26), 7383–7393.

(28) Tang, C. Y.; Huang, Z.; Allen, H. C. Binding of Mg^{2+} and Ca^{2+} to Palmitic Acid and Deprotonation of the COOH Headgroup Studied by Vibrational Sum Frequency Generation Spectroscopy. *J. Phys. Chem. B* **2010**, *114* (51), 17068–17076.

(29) Casillas-Ituarte, N. N.; Chen, X.; Castada, H.; Allen, H. C. Na^+ and Ca^{2+} Effect on the Hydration and Orientation of the Phosphate Group of DPPC at Air-Water and Air-Hydrated Silica Surface. *J. Phys. Chem. B* **2010**, *114* (29), 9485–9495.

(30) Kewalramani, S.; Hlaing, H.; Ocko, B. M.; Kuzmenko, I.; Fukuto, M. Effects of Divalent Cations on Phase Behavior and Structure of a Zwitterionic Phospholipid (DMPC) Monolayer at the Air-Water Inteface. *J. Phys. Chem. Lett.* **2010**, *1* (2), 489–495.

(31) Millero, F. J. *Chemical Oceanography*, 4th ed.; CRC Press: Boca Raton, FL, 2013.

(32) Ault, A. P.; Guasco, T. L.; Ryder, O. S.; Baltrusaitis, J.; Cuadra-Rodriguez, L. A.; Collins, D. B.; Ruppel, M. J.; Bertram, T. H.; Prather, K. A.; Grassian, V. H. Inside versus Outside: Ion Redistribution in Nitric Acid Reacted Sea Spray Aerosol Particles as Determined by Single Particle Analysis. *J. Am. Chem. Soc.* **2013**, *135* (39), 14528–14531.

(33) Barker, D. R.; Zeitlin, H. Metal-Ion Concentrations in Sea-Surface Microlayer and Size-Separated Atmospheric Samples in Hawaii. *J. Geophys. Res.* **1972**, *77* (27), 5076–5086.

(34) Piotrowicz, S. R.; Duce, R. A.; Fasching, J. L.; Weisel, C. P. Bursting Bubbles and Their Effect on the Sea-to-Air Transport of Fe, Cu, and Zn. *Mar. Chem.* **1979**, *7* (4), 307–324.

(35) Oppo, C.; Bellandi, S.; Degli Innocenti, N.; Stortini, A. M.; Loglio, G.; Schiavuta, E.; Cini, R. Surfactant Components of Marine Organic Matter as Agents for Biogeochemical Fractionation and Pollutant Transport via Marine Aerosols. *Mar. Chem.* **1999**, *63* (3–4), 235–253.

(36) Russell, L. M.; Hawkins, L. N.; Frossard, A. A.; Quinn, P. K.; Bates, T. S. Carbohydrate-like Composition of Submicron Atmosphere Particles and Their Production from Ocean Bubble Bursting. *Proc. Natl. Acad. Sci. U. S. A.* **2010**, *107* (15), 6652–6657.

(37) Schill, S. R.; Collins, D. B.; Lee, C.; Morris, H. S.; Novak, G. A.; Prather, K. A.; Quinn, P. K.; Sultana, C. M.; Tivanski, A. V.; Zimmermann, K. Z.; et al. The Impact of Aerosol Particle Mixing State on the Hygroscopicity of Sea Spray Aerosol. *ACS Cent. Sci.* **2015**, *1* (3), 132–141.

(38) Keene, W. C.; Pszenny, A. A. P.; Maben, J. R.; Sander, R. Variation of Marine Aerosol Acidity with Particle Size. *Geophys. Res. Lett.* **2002**, *29* (7), 1101.

(39) Frindlind, A. M.; Jacobson, M. Z. A Study of Gas-Aerosol Equilibrium and Aerosol pH in the Remote Marine Boundary Layer during the First Aerosol Characterization Experiment (ACE 1). *J. Geophys. Res.* **2000**, *105* (D13), 17325–17340.

(40) Garret, R. H.; Grisham, C. M. *Biochemistry*, 4th ed.; Brooks/Cole: Boston, MA, 2010.

(41) Maggio, B. The Surface Behavior of Glycosphingolipids in Biomembranes: A New Frontier of Molecular Ecology. *Prog. Biophys. Mol. Biol.* **1994**, *62* (1), 55–117.

(42) Barfield, K. D.; Bevan, D. R. Fusion of Phospholipid Vesicles Induced by Zn^{2+}, Cd^{2+}, and Hg^{2+}. *Biochem. Biophys. Res. Commun.* **1985**, *128* (1), 389–395.

(43) Wang, W.; Zhang, H.; Feng, S.; Emeterio, J. S.; Mallapragada, S.; Vaknin, D. Iron Ion and Iron Hydroxide Adsorption to Charge-Neutral Phosphatidylcholine Templates. *Langmuir* **2016**, *32* (30), 7664–7670.

(44) Wickett, R. R.; Visscher, M. O. Structure and Function of the Epidermal Barrier. *Am. J. Infect. Control* **2006**, *34* (10), S98–S110.

(45) Haugen, M.; Williams, J. B.; Wertz, P. W.; Tieleman, B. I. Lipids of the Stratum Corneum Vary with Cutaneous Water Loss among Larks along a Temperature-Moisture Gradient. *Physiol. Biochem. Zool.* **2003**, *76* (6), 907–917.

(46) Muñoz-Garcia, A.; Williams, J. B. Cutaneous Water Loss and Lipids of the Stratum Corneum in House Sparrows *Passer Domesticus* from Arid and Mesic Environments. *J. Exp. Biol.* **2005**, *208*, 3689–3700.

(47) Champagne, A. M.; Munoz-Garcia, A.; Shtayyeh, T.; Tieleman, B. I.; Hegemann, A.; Clement, M. E.; Williams, J. B. Lipid Composition of the Stratum Corneum and Cutaneous Water Loss in Bird along an Aridity Gradient. *J. Exp. Biol.* **2012**, *215* (24), 4299–4307.

(48) Hénon, S.; Meunier, J. Microscope at the Brewster Angle: Direct Observation of First Order Phase Transitions in Monolayers. *Rev. Sci. Instrum.* **1991**, *62* (4), 936.

(49) Hönig, D.; Möbius, D. Direct Visualization at the Air-Water Interface by Brewster Angle Microscopy. *J. Phys. Chem.* **1991**, *95* (12), 4590–4592.

(50) Lheveder, C.; Hénon, S.; Meunier, J. Brewster Angle Microscopy. In *Physical Chemistry of Biological Interfaces*; Baszkin, A., Norde, W., Eds.; Marcel Dekker: New York, NY, 2000.

(51) Fowles, G. R. *Introduction to Modern Optics*, 2nd ed.; Dover Publicatons, Inc.: New York, 1975.

(52) Hecht, E. *Optics*, 4th ed.; Addison Wesley, 2002.

(53) Lheveder, C.; Henon, S.; Mercier, R.; Tissot, G.; Fournet, P. A New Brewster Angle Microscope. *Rev. Sci. Instrum.* **1998**, *69* (3), 1446.

(54) Ducharme, D.; Max, J.-J.; Salesse, C.; Leblanc, R. M. Ellipsometric Study of the Physical States of Phosphatidylcholines at the Air-Water Interface. *J. Phys. Chem.* **1990**, *94* (5), 1925–1932.

(55) Arwin, H. Ellipsometry. In *Physical Chemistry of Biological Interfaces*; Baszkin, A., Norde, W., Eds.; Marcel Dekker: New York, NY, 2000.

(56) Gericke, A.; Michailov, A. V.; Hühnerfuss, H. Polarized External Infrared Reflection-Absorption Spectrometry at the Air/Water Interface: Comparison of Experimental and Theoretical Results for Different Angles of Incidence. *Vib. Spectrosc.* **1993**, *4*, 335–348.

(57) Mendelsohn, R.; Brauner, J. W.; Gericke, A. External Infrared Reflection Absorption Spectrometry of Monolayer Films at the Air-Water Interface. *Annu. Rev. Phys. Chem.* **1995**, *46*, 305–334.

(58) Flach, C. R.; Gericke, A.; Mendelsohn, R. Quantitative Determination of Molecular Chain Tilt Angles in Monolayer Films at the Air/Water Interface: Infrared Reflection/Absorption Spectroscopy of Behenic Acid Methyl Ester. *J. Phys. Chem. B* **1997**, *101* (1), 58–65.

(59) Boyd, R. W. *Nonlinear Optics*, 3rd ed.; Academic Press: San Diego, CA, 2008.

(60) Hirose, C.; Akamatsu, N.; Domen, K. Formulas for the Analysis of the Surface SFG Spectrum and Transformation Coefficients of Cartesian SFG Tensor Components. *Appl. Spectrosc.* **1992**, *46* (6), 1051–1072.

(61) Lambert, A. G.; Davies, P. B.; Neivandt, D. J. Implementing the Theory of Sum Frequency Generation Vibrational Spectroscopy - A Tutorial Review. *Appl. Spectrosc.* **2005**, *40* (2), 103.

(62) Wang, H.-F.; Gan, W.; Lu, R.; Rao, Y.; Wu, B.-H. Quantitative Spectral and Orientational Analysis in Surface Sum Frequency Generation Vibrational Spectroscopy (SFG-VS). *Int. Rev. Phys. Chem.* **2005**, *24* (2), 191–256.

(63) Watanabe, N.; Yamamoto, H.; Wada, A.; Domen, K.; Hirose, C. Vibrational Sum-Frequency Generation (VSFG) Spectra of N-Alkyltrichlorosilanes Chemisorbed on Quartz Plate. *Spectrochim. Acta* **1994**, *50A* (8/9), 1529–1537.

(64) Zhang, D.; Gutow, J.; Eisenthal, K. B. Vibrational Spectra, Orientations, and Phase Transitions in Long-Chain Amphiphiles at the Air/Water Interface: Probing the Head and Tail Groups by Sum Frequency Generation. *J. Phys. Chem.* **1994**, *98* (51), 13729–13734.

(65) Griffith, E. C.; Adams, E. M.; Allen, H. C.; Vaida, V. Hydrophobic Collapse of a Stearic Acid Film by Adsorbed L-Phenylalanine at the Air-Water Interface. *J. Phys. Chem. B* **2012**, *116* (27), 7849–7857.

(66) Adams, E. M.; Allen, H. C. Palmitic Acid on Salt Subphases and in Mixed Monolayers of Cerebrosides: Application to Atmospheric Aerosol Chemistry. *Atmosphere* **2013**, *4* (4), 315–336.

(67) Casper, C. B.; Verreault, D.; Adams, E. M.; Hua, W.; Allen, H. C. Surface Potential of DPPC Monolayers on Concentrated Aqueous Salt Solutions. *J. Phys. Chem. B* **2016**, *120* (8), 2043–2052.

(68) Adams, E. M.; Casper, C. B.; Allen, H. C. Effect of Cation Enrichment on Dipalmitoylphosphatidylcholine (DPPC) Monolayers at the Air-Water Interface. *J. Colloid Interface Sci.* **2016**, *478*, 353–364.

(69) Hua, W.; Verreault, D.; Adams, E. M.; Huang, Z.; Allen, H. C. Impact of Salt Purity on Interfacial Water Organization Revealed by Conventional and Heterodyne-Detected Vibrational Sum Frequency Generation Spectroscopy. *J. Phys. Chem. C* **2013**, *117* (38), 19577–19585.

(70) Yoon, Y. J.; Ceburnis, D.; Cavalli, F.; Jourdan, O.; Putaud, J.-P.; Facchini, M. C.; Decesari, S.; Fuzzi, S.; Sellegri, K.; Jennings, S. G.; et al. Seasonal Characteristics of the Physiochemical Properties of North Atlantic Marine Atmospheric Aerosols. *J. Geophys. Res.* **2007**, *112* (D4), D04206.

(71) Fu, H.; Ciuraru, R.; Dupart, Y.; Passananti, M.; Tinel, L.; Rossignol, S.; Perrier, S.; Donaldson, D. J.; Chen, J.; George, C. Photosensitized Production of Atmospherically Reactive Organic Compounds at the Air/Aqueous Interface. *J. Am. Chem. Soc.* **2015**, *137* (26), 8348–8351.

(72) Nakahara, H.; Nakamura, S.; Nakamura, K.; Inagaki, M.; Aso, M.; Higuchi, R.; Shibata, O. Cerebroside Langmuir Monolayers Originated from Echinoderms I.

Binary Systems of Cerebrosides and Phospholipids. *Colloids Surf. B Biointerfaces* **2005**, *42* (2), 157–174.

(73) Ma, G.; Allen, H. C. DPPC Langmuir Monolayer at the Air-Water Interface: Probing the Tail and Head Groups by Vibrational Sum Frequency Generation Spectroscopy. *Langmuir* **2006**, *22* (12), 5341–5349.

(74) Lee, K. Y. C. Collapse Mechanisms of Langmuir Monolayers. *Annu. Rev. Phys. Chem.* **2008**, *59*, 771–791.

(75) Espinosa, L. F.; Pantoja, S.; Pinto, L. A.; Rullkötter, J. Water Column Distribution of Phospholipid-Derived Fatty Acids of Marine Microorganisms in the Humboldt Current System off Northern Chile. *Deep-Sea Res. II* **2009**, *56* (16), 1063–1072.

(76) Finlayson, A. C. The pH Range of the Mohr Titration for Chloride Ion Can Be Usefully Extended to 4-10.5. *J. Chem. Educ.* **1992**, *69* (7), 559.

(77) Prokop, R. M.; Neumann, A. W. Measurements of the Interfacial Properties of Lung Surfactant. *Curr. Opin. Colloid Interface Sci.* **1996**, *1* (5), 677–681.

(78) Haynes, W. M. *CRC Handbook of Chemistry and Physics*, 96th ed.; CRC Press: Boca Raton, FL, 2015.

(79) Rodríguez Patino, J. M.; Carrara Sánchez, C.; Rodríguez Niño, M. R. Morphological and Structural Characteristics of Monoglyceride Monolayers at the Air-Water Interface Observed by Brewster Angle Microscopy. *Langmuir* **1999**, *15* (7), 2484–2492.

(80) Miñones, Jr., J.; Pais, S.; Miñones, J.; Conde, O.; Dynarowics-Latka, P. Interactions between Membrane Sterols and Phospholipids in Model Mammalian and Fungi Cellular Membranes - A Langmuir Monolayer Study. *Biophys. Chem.* **2009**, *140* (1–3), 69–77.

(81) Phillips, M. C.; Chapman, D. Monolayer Characteristics of Saturated 1,2-Diacyl Phosphatidylcholines (Lecithins) and Phosphatidylethanolamines at the Air-Water Interface. *Biochim. Biophys. Acta* **1968**, *163* (3), 301–313.

(82) Shapovalov, V. L. Interaction of DPPC Monolayer at Air-Water Interface with Hydrophobic Ions. *Thin Solid Films* **1998**, *327–329*, 599–602.

(83) Aroti, A.; Leontidis, E.; Maltseva, E.; Brezesinski, G. Effects of Hofmeister Anions on DPPC Langmuir Monolayers at Air-Water Interface. *J. Phys. Chem. B* **2004**, *108* (39), 15238–15245.

(84) Sovago, M.; Wurpel, G. W. H.; Smits, M.; Müller, M.; Bonn, M. Calcium-Induced Phospholipid Ordering Depends on Surface Pressure. *J. Am. Chem. Soc.* **2007**, *129* (36), 11079–11084.

(85) Leontidis, E.; Aroti, A.; Belloni, L. Liquid-Expanded Monolayers of Lipids As Model Systems to Understand the Anionic Hofmeister Series: 1. A Tale of Models. *J. Phys. Chem. B* **2009**, *113* (5), 1447–1459.

(86) Eftaiha, A. F.; Paige, M. F. The Influence of Salinity on Surfactant Miscibility in Mixed Dipalmitoylphosphatidylcholine - Perfluorooctadecanoic Acid Monolayer Films. *J. Colloid Interface Sci.* **2011**, *353* (1), 210–219.

(87) Christoforou, M.; Leontidis, E.; Brezesinski, G. Effects of Sodium Salts of Lyotropic Anions on Low-Temperature, Ordered Lipid Monolayers. *J. Phys. Chem. B* **2012**, *116* (50), 14602–14612.

(88) Petelska, A. D.; Figazewski, Z. A. The Equilibria of Lipid-K^+ Ions in Monolayer at the Air/Water Interface. *J. Membr. Biol.* **2011**, *244* (2), 61–66.

(89) Arczewska, M.; Gagos, M. Molecular Organization of Antibiotic Amphotericin B in Dipalmitoylphosphatidylcholine Monolayers Induced by K^+ and Na^+ Ions: The Langmuir Technique Study. *Biochim. Biophys. Acta* **2011**, *1808* (11), 2706–2713.

(90) Cordomí, A.; Edholm, O.; Perez, J. J. Effects of Ions on a Dipalmitoyl Phosphatidylcholine Bilayer: A Molecular Dynamics Simulation Study. *J. Phys. Chem. B* **2008**, *112* (5), 1397–1408.

(91) Gurtovenko, A. A.; Vattulainen, I. Effect of NaCl and KCl on Phosphatidylcholine and Phosphatidylethanolamine Lipid Membranes: Insight from Atomic-Simulations for Understanding Salt-Induced Effects in the Plasma Membrane. *J. Phys. Chem. B* **2008**, *112* (7), 1953–1962.

(92) Petelska, A. D.; Figazewski, Z. A. The Equilibria Between Monovalent Ions and Phosphatidylcholine Monolayers at the Air/Water Interface. *J. Membr. Biol.* **2013**, *246* (6), 467–471.

(93) Ou-Yang, W.; Yamamoto, T.; Manaka, T.; Iwamoto, M. Effect of External Electrostatic Charge on Condensed Phase Domains at the Air-Water Interface: Experiment and Shape Equation Analysis. *J. Chem. Phys.* **2009**, *130* (10), 104706.

(94) Petelska, A. D.; Figazewski, Z. A. Phosphatidylcholine - Mg^{2+} Equilibria in a Monolayer at the Air/Water Interface. *Cent. Eur. J. Chem.* **2013**, *11* (3), 424–429.

(95) Casillas-Ituarte, N. N.; Callahan, K. M.; Tang, C. Y.; Chen, X.; Roeselova, M.; Tobias, D. J.; Allen, H. C. Surface Organization of Aqueous MgCl2 and Application to Atmospheric Marine Aerosol Chemistry. *Proc. Natl. Acad. Sci. U. S. A.* **2010**, *107* (15), 6616–6621.

(96) Pavlov, M.; Siegbahn, P. E. M.; Sandstrom, M. Hydration of Beryllium, Magnesium, Calcium, and Zinc Ions Using Density Functional Theory. *J. Phys. Chem. A* **1998**, *102* (1), 219–228.

(97) Ross, M.; Steinem, C.; Galla, H.-J.; Janshoff, A. Visualization of Chemical and Physical Properties of Calcium-Induced Domains in DPPC/DPPS Langmuir-Blodgett Layers. *Langmuir* **2001**, *17* (8), 2437–2445.

(98) Lee, Y.-L.; Lin, J.-L.; Chang, C.-H. Thermodynamic Characteristics and Langmuir-Blodgett Deposition Behavior of Mixed DPPA/DPPC Monolayers at Air/Liquid Interfaces. *J. Colloid Interface Sci.* **2006**, *296* (2), 647–654.

(99) Petelska, A. D.; Niemcunowicz-Janica, A.; Szeremeta, M.; Figazewski, Z. A. Equilibria of Phosphatidylcholine - Ca^{2+} Ions in Monolayer at the Air/Water Interface. *Langmuir* **2010**, *26* (16), 13359–13363.

(100) Kundu, S.; Matsuoka, H.; Seto, H. Zwitterionic Lipid (DPPC)-Protein (BSA) Complexes at the Air-Water Interface. *Colloids Surf. B Biointerfaces* **2012**, *93* (1–2), 215–2218.

(101) Huang, Z.; Hua, W.; Verreault, D.; Allen, H. C. Impact of Salt Purity on Na^+ and Palmitic Acid Interactions. *J. Phys. Chem. A* **2013**, *117* (50), 13412–13418.

(102) Davies, J. T.; Rideal, E. K. *Interfacial Phenomena*, 2nd ed.; New York, NY, 1963.

(103) Duncan, S. L.; Larson, R. G. Comparing Experimental and Simulated Pressure-Area Isotherms for DPPC. *Biophys. J.* **2008**, *94* (8), 2965–2986.

(104) Telesford, D.-M.; Verreault, D.; Reick-Mitrisin, V.; Allen, H. C. Reduced Condensing and Ordering Effects by 7-Ketocholesterol and 5β,6β-Epoxycholesterol on DPPC Monolayers. *Langmuir* **2015**, *31* (36), 9859–9869.

(105) Chen, X.; Huang, Z.; Hua, W.; Castada, H.; Allen, H. C. Reorganization and Caging of DPPC, DPPE, DPPG, and DPPS Monolayers Caused by Dimethylsulfoxide Observed Using Brewster Angle Microscopy. *Langmuir* **2010**, *26* (24), 18902–18908.

(106) Adamson, A. W.; Gast, A. P. *Physical Chemistry of Surfaces*, 6th ed.; Wiley: New York, NY, 1997.

(107) Arnold, A.; Cloutier, I.; Ritcey, A. M.; Auger, M. Temperature and Pressure Dependent Growth and Morphology of DMPC/DSPC Domains Studies by Brewster Angle Microscopy. *Chem. Phys. Lipids* **2005**, *133* (2), 165–179.

(108) Dhar, P.; Eck, E.; Israelachvili, J. N.; Lee, D. W.; Min, Y.; Ramachandran, A.; Waring, A. J.; Zasadzinski, J. A. Lipid-Protein Interactions Alter Line Tensions and Domain Size Distributions in Lung Surfactant Monolayers. *Biophys. J.* **2012**, *102* (1), 56–65.

(109) Binder, H.; Zschörnig, O. The Effect of Metal Cations on the Phase Behavior and Hydration Characteristics of Phospholipid Membranes. *Chem. Phys. Lipids* **2002**, *115* (1–2), 39–61.

(110) Pandit, S. A.; Bostick, D.; Berkowitz, M. L. Molecular Dynamic Simulation of a Dipalmitoylphosphatidylcholine Bilayer with NaCl. *Biophys. J.* **2003**, *84* (6), 3743–3750.

(111) Casal, H. L.; Mantsch, H. H. Polymorphic Phase Behavior of Phospholipid Membranes Studied by Infrared Spectroscopy. *Biochim. Biophys. Acta* **1984**, *779* (4), 381–401.

(112) Maltseva, E.; Shapovalov, V. L.; Möhwald, H.; Brezesinski, G. Ionization State and Structure of L-1,2-Dipalmitoylphosphatidylglycerol Monolayers at the Liquid/Air Interface. *J. Phys. Chem. B* **2006**, *110* (2), 919–926.

(113) Callahan, K. M.; Casillas-Ituarte, N. N.; Roeselova, M.; Allen, H. C.; Tobias, D. J. Solvation of Magnesium Dication: Molecular Dynamics Simulation and Vibrational Spectroscopic Study of Magnesium Chloride in Aqueous Solutions. *J. Phys. Chem. A* **2010**, *114* (15), 5141–5148.

(114) van der Post, S. T.; Hunger, J.; Bonn, M.; Bakker, H.J. Observation of Water Separated Ion-Pairs between Cations and Phospholipid Headgroups. *J. Phys. Chem. B* **2014**, *118* (16), 4397–4403.

(115) Burrows, S. M.; Ogunro, O.; Frossard, A. A.; Russell, L. M.; Rasch, P. J.; Elliott, S. M. A Physically Based Framework for Modeling the Organic Fractionation of Sea Spray Aerosol from Bubble Film Langmuir Equilibria. *Atmospheric Chem. Phys.* **2014**, *14* (24), 13601–13629.

(116) Gogou, A.; Stratigakis, N.; Kanakidou, M.; Stephanou, E. G. Organic Aerosols in Eastern Mediterranean: Components Source Reconciliation by Using Molecular Markers and Atmospheric Back Trajectories. *Org. Geochem.* **1996**, *25* (1/2), 79–96.

(117) McInnes, L. M.; Covert, D. S.; Quinn, P. K.; Germani, M. S. Measurements of Chloride Depletion and Sulfur Enrichment in Individual Sea-Seal Particles Collected from the Remote Boundary Layer. *J. Geophys. Res.* **1994**, *99* (D4), 8257–8268.

(118) Guzman, M. I.; Athalye, R. R.; Rodriguez, J. M. Concentration Effects and Ion Properties Controlling the Fractionation of Halides during Aerosol Formation. *J. Phys. Chem. A* **2012**, *116* (22), 5428–5435.

(119) Burrows, S. M.; Gobrogge, E.; Fu, L.; Link, K.; Elliott, S. M.; Wang, H.-F.; Walker, R. OCEANFILMS-2: Representing Coadsorption of Saccharides in Marine Films and Potential Impacts on Modeled Marine Aerosol Chemistry. *Geophys. Res. Lett.* **2016**, *43* (15), 8306–8313.

(120) Komabayasi, M. Primary Fractionation of Chemical Components in the Formation of Submicron Spray Drops from Seasalt Solution. *J. Meteorol. Soc. Jpn.* **1964**, *42* (5), 309–316.

(121) Hoffman, E. J.; Duce, R. A. Alkali and Alkanline Earth Metal Chemistry of Marine Aerosols Generated in the Laboratory with Natural Seawaters. *Atmos. Environ.* **1977**, *11* (4), 367–372.

(122) Weisel, C. P.; Duce, R. A.; Fasching, J. L.; Heaton, R. W. Estimates of the Transport of Trace Metals From the Ocean to the Atmosphere. *J. Geophys. Res.* **1984**, *89* (D7), 11607–11618.

(123) Salter, M. E.; Hamacher-Barth, E.; Leck, C.; Werner, J.; Johnson, C. M.; Riipinen, I.; Nilsson, E. D.; Zieger, P. Calcium Enrichment in Sea Spray Aerosol Particles. *Geophys. Res. Lett.* **2016**, *43* (15), 8277–8285.

(124) Sigiyama, N.; Shimizu, A.; Nakamura, M.; Nakagawa, Y.; Nagasawa, Y.; Ishida, H. Molecular-Scale Structures of Langmuir-Blodgett Films of Fatty Acids Observed by Atomic Force Microscopy (II) - Cation Dependence. *Thin Solid Films* **1998**, *331* (1–2), 170–175.

(125) Kmetko, J.; Datta, A.; Evmeneko, G.; Dutta, P. The Effects of Divalent Ions on Langmuir Monolayer and Subphase Structure: A Grazing-Incidence Diffraction and Bragg Rod Study. *J. Phys. Chem. B* **2001**, *105* (44), 10818–10825.

(126) Wang, W.; Park, R. Y.; Meyer, D. H.; Travesset, A.; Vaknin, D. Ionic Specificity in pH Regulated Charged Interfaces: Fe^{3+} versus La^{3+}. *Langmuir* **2011**, *27* (19), 11917–11924.

(127) Bergamino, M.; Relini, A.; Rispoli, P.; Giachini, L.; d'Acapito, F.; Rolandi, R. An EXAFS Study of the Binding of Cd and Pb Ions to Lipid Films. *Eur. Phys. J. E* **2013**, *36* (102), 1–7.

(128) Garidel, P.; Blume, A. 1,2-Dimyristoyl-*sn*-Glycero-3-Phosphoglycerol (DMPG) Monolayers: Influence of Temperatue, pH, Ionic Strength and Binding of Alkaline Earth Cations. *Chem. Phys. Lipids* **2005**, *138* (1–2), 50–59.

(129) Lucero, A.; Nino, M. R. R.; Gunning, A. P.; Morris, V. J.; Wilde, P. J.; Patino, J. M. R. Effect of Hydrocarbon Chain and pH on Structural and Topographical Characteristics of Phospholipid Monolayers. *J. Phys. Chem. B* **2008**, *112*, 7651–7661.

(130) Binder, H.; Arnold, K.; Ulrich, A. S.; Zschörnig, O. Interaction of Zn^{2+} with Phospholipid Membranes. *Biophys. Chem.* **2001**, *90* (1), 57–74.

(131) Miñones, Jr., J.; Rodríguez Patino, J. M.; Conde, O.; Carrera, C.; Seoane, R. The Effect of Polar Groups on Structural Characteristics of Phospholipid Monolayers Spread at the Air-Water Interface. *Colloids Surf. Physiochemical Eng. Asp.* **2002**, *203* (1–3), 273–286.

(132) Toimil, P.; Prieto, G.; Miñones, Jr., J.; Trillo, J. M.; Sarmiento, F. Monolayer and Brewster Angle Microscopy Study of Human Serum Albumin-Dipalmitoyl Phosphatidyl Choline Mixtures at the Air-Water Interface. *Colloids Surf. B Biointerfaces* **2012**, *92*, 64–73.

(133) Vaknin, D.; Kjaer, K.; Als-Nielsen, J.; Lösche, M. Structural Properties of Phosphatidylcholine in a Monolayer at the Air/Water Interface. *Biophys. J.* **1991**, *59* (6), 1325–1332.

(134) d'Acapito, F.; Emelianov, I.; Relini, A.; Cavatora, P.; Gliozzi, A.; Minicozzi, V.; Morante, S.; Solari, P. L.; Rolandi, R. Total External Reflection X-Ray Absorption Spectroscopy Reveals a Zinc Coordination Shell in Phospholipid Langmuir-Blodgett Films. *Langmuir* **2002**, *18* (13), 5277–5282.

(135) Siegman, A. E. *Lasers*; University Science Books: Sausalito, CA, 1986.

(136) Gericke, A.; Hühnerfuss, H. Investigation of Z- and E-Unsaturated Fatty Acids, Fatty Acid Esters, and Fatty Alcohols at the Air/Water Interface by Infrared Spectroscopy. *Langmuir* **1995**, *11* (1), 225–230.

(137) Marcus, Y. *Ions in Solution and Their Solvation*, 1st ed.; John Wiley & Sons: Hoboken, NJ, 2015.

(138) Tackett, J. E. FT-IR Characterization of Metal Acetates in Aqueous Solution. *Appl. Spectrosc.* **1989**, *43* (3), 483–489.

(139) Atkins, P.; Overton, T.; Rourke, J.; Weller, M.; Armstrong, F. *Inorganic Chemistry*, 4th ed.; New York, NY, 2006.

(140) Gurau, M. C.; Kim, G.; Lim, S.-M.; Albertorio, F.; Fleischer, H. C.; Cremer, P. S. Organization of Water Layers at Hydrophilic Interfaces. *ChemPhysChem* **2003**, *4* (11), 1231–1233.

(141) Kherb, J.; Flores, S. C.; Cremer, P. S. Role of Carboxylate Side Chains in the Cation Hofmeister Series. *J. Phys. Chem. B* **2012**, *116* (25), 7389–7397.

(142) Cong, X.; Poyton, M. F.; Baxter, A. J.; Pullanchery, S.; Cremer, P. S. Unquenchable Surface Potential Dramatically Enhances Cu^{2+} Binding to Phosphatidylserine Lipids. *J. Am. Chem. Soc.* **2015**, *137* (24), 7785–7792.

(143) Tang, C. Y.; Huang, Z.; Allen, H. C. Interfacial Water Structure and Effects of Mg^{2+} and Ca^{2+} Binding to the COOH Headgroup of a Palmitic Acid Monolayer Studied by Sum Frequency Spectroscopy. *J. Phys. Chem. B* **2011**, *115* (1), 34–40.

(144) Shaloski, M. A.; Sobyra, T. B.; Nathanson, G. M. DCl Transport through Dodecyl Sulfate Films on Salty Glycerol: Effects of Seawater Ions on Gas Entry. *J. Phys. Chem. A* **2015**, *119* (50), 12357–12366.

(145) Hudait, A.; Molinero, V. What Determines the Ice Polymorph in Clouds? *J. Am. Chem. Soc.* **2016**, *138* (28), 8958–8967.

(146) Du, Q.; Superfine, R.; Freysz, E.; Shen, Y. R. Vibrational Spectroscopy of Water at the Vapor/Water Interface. *Phys. Rev. Lett.* **1993**, *70* (15), 2313–2316.

(147) Shen, Y. R.; Ostroverkhov, V. Sum-Frequency Vibrational Spectroscopy on Water Interfaces: Polar Orientation of Water Molecules at Interfaces. *Chem. Rev.* **2006**, *106* (4), 1140–1154.

(148) Raymond, E. A.; Tarbuck, T. L.; Richmond, G. L. Isotopic Dilution Studies of the Vapor/Water Interface as Investigated by Vibrational Sum-Frequency Spectroscopy. *J. Phys. Chem. B* **2002**, *106* (11), 2817–2820.

(149) Walker, D. S.; Hore, D. K.; Richmond, G. L. Understanding the Population, Coordination, and Orientation of Water Species Contributing to the Nonlinear Optical Spectroscopy of the Vapor-Water Interface through Molecular Dynamics Simulations. *J. Phys. Chem. B* **2006**, *110* (41), 20451–20459.
(150) Sovago, M.; Campen, R. K.; Bakker, H. J.; Bonn, M. Hydrogen Bonding Strength of Interfacial Water Determined with Surface Sum-Frequency Generation. *Chem. Phys. Lett.* **2009**, *470* (1–3), 7–12.
(151) Tian, C.; Byrnes, S. J.; Han, H.-L.; Shen, Y. R. Surface Propensities of Atmospherically Relevant Ions in Salt Solutions Revealed by Phase-Sensitive Sum Frequency Vibrational Spectroscopy. *J. Phys. Chem. Lett.* **2011**, *2* (15), 1946–1949.
(152) Hua, W.; Verreault, D.; Huang, Z.; Adams, E. M.; Allen, H. C. Cation Effects on Interfacial Water Organization of Aqueous Chloride Solutions. I. Monovalents Cations: Li^+, Na^+, K^+, and NH_4^+. *J. Phys. Chem. B* **2014**, *118* (28), 8433–8440.
(153) Hua, W.; Verreault, D.; Allen, H. C. Solvation of Calcium-Phosphate Headgroup Complexes at the DPPC/Aqueous Interface. *ChemPhysChem* **2015**, *16* (18), 3910–3915.
(154) Hua, W.; Jubb, A. M.; Allen, H. C. Electric Field Reversal of Na_2SO_4, $(NH_4)_2SO_4$, and Na_2CO_3 Relative to $CaCl_2$ and NaCl at the Air/Aqueous Interface Revealed by Heterodyne Detected Phase-Sensitive Sum Frequency. *J. Phys. Chem. Lett.* **2011**, *2* (20), 2515–2520.
(155) Gopalakrishnan, S.; Jungwirth, P.; Tobias, D. J.; Allen, H. C. Air-Liquid Interfaces of Aqueous Solutions Containing Ammonium and Sulfate: Spectroscopic and Molecular Dynamics Studies. *J. Phys. Chem. B* **2005**, *109* (18), 8861–8872.
(156) Watry, M. R.; Tarbuck, T. L.; Richmond, G. L. Vibrational Sum-Frequency Studies of a Series of Phospholipid Monolayers and Associated Water Structure at the Vapor/Water Interface. *J. Phys. Chem. B* **2003**, *107* (2), 512–518.
(157) Ma, G.; Chen, X.; Allen, H. C. Dangling OD Confined in a Langmuir Monolayer. *J. Am. Chem. Soc.* **2007**, *129* (45), 14053–14057.
(158) Israelachvili, J. *Intermolecular and Surface Forces*, 3rd ed.; Academic Press: New York, 2011.
(159) Aluwihare, L. I.; Repeta, D. J.; Chen, R. F. A Major Biopolymeric Component to Dissolved Organic Carbon in Surface Sea Water. *Nature* **1997**, *387* (6629), 166–169.
(160) Hawkins, L. N.; Russell, L. M. Polysaccharides, Proteins, and Phytoplankton Fragments: Four Chemically Distinct Types of Marine Primary Organic Aerosol Classified by Single Particle Spectromicroscopy. *Adv. Meterology* **2010**.

(161) Rinaldi, M.; Decesari, S.; Finessi, E.; Giulianelli, L.; Carbone, C.; Fuzzi, S.; O'Dowd, C. D.; Ceburnis, D.; Facchini, M. C. Primary and Secondary Organic Marine Aerosol and Oceanic Biological Activity: Recent Results and New Perspectives for Future Studies. *Adv. Meterology* **2010**.

(162) Lass, K.; Kleber, J.; Friedrichs, G. Vibrational Sum-Frequency Generation as a Probe for Composition, Chemical Reactivity, and Film Formation Dynamics of the Sea Surface Nanolayer. *Limnol. Oceanogr.* **2010**, *8*, 216–228.

(163) Lass, K.; Friedrichs, G. Revealing Structural Properties of the Marine Nanolayer from Vibrational Sum Frequency Generation Spectra. *J. Geophys. Res.* **2011**, *116*, C08042.

(164) Ault, A. P.; Zhao, D.; Ebben, C. J.; Tauber, M. J.; Geiger, F. M.; Prather, K. A.; Grassian, V. H. Raman Microspectroscopy and Vibrational Sum Frequency Generation Spectroscopy as Probes of Bulk an Surface Compositions of Size-Resolved Sea Spray Aerosol Particles. *Phys. Chem. Chem. Phys.* **2013**, *15*, 6206–6214.

(165) Ebben, C. J.; Ault, A. P.; Ruppel, M. J.; Ryder, O. S.; Bertram, T. H.; Grassian, V. H.; Prather, K. A.; Geiger, F. M. Size-Resolved Sea Spray Aerosol Particles Studied by Vibrational Sum Frequency Generation. *J. Phys. Chem. A* **2013**, *117* (30), 6589–6601.

(166) Trueblood, J.; Estillore, A. D.; Lee, C.; Dowling, J. A.; Prather, K. A.; Grassian, V. H. Heterogeneous Chemistry of Lipopolysaccharides with Gas-Phase Nitric Acid: Reactive Sites and Reaction Pathways. *J. Phys. Chem. A* **2016**, *120* (32), 6444–6450.

(167) García-Verdugo, I.; Cañadas, O.; Taneva, S. G.; Keough, K. M. W.; Casals, C. Surfactant Protein A Forms Extensive Lattice-Like Structures on 1,2-Dipalmitoylphosphatidylcholine/Rough-Lipopolysaccharide-Mixed Monolayers. *Biophys. J.* **2007**, *93* (10), 3529–3540.

(168) Cañadas, O.; Keough, K. M. W.; Casals, C. Bacterial Lipopolysaccharide Promotes Destabilization of Lung Surfactant-Like Films. *Biophys. J.* **2011**, *100* (1), 108–116.

(169) Abraham, T.; Schooling, S. R.; Beveridge, T. J.; Katsaras, J. Monolayer Film Behavior of Lipopolysaccharide from *Pseudomonas Aeruginosa* at the Air-Water Interface. *Biomacromolecules* **2008**, *9* (10), 2799–2804.

(170) Jeworrek, C.; Evers, F.; Howe, J.; Brandenburg, K.; Tolan, M.; Winter, R. Effects of Specific versus Nonspecific Ionic Interactions of the Structure and Lateral Organization of Lipopolsaccharides. *Biophys. J.* **2011**, *100* (9), 2169–2177.

(171) Le Brun, A. P.; Clifton, L. A.; Halbert, C. E.; Lin, B.; Meron, M.; Holden, P. J.; Lakey, J. H.; Holt, S. A. Structural Characterization of Model Gram-Negative

Bacterial Surface Using Lipopolysaccharides from Rough Strains of *Escherichia Coli*. *Biomacromolecules* **2013**, *14* (6), 2014–2022.

(172) Tyrode, E.; Johnson, C. M.; Kumpulainen, A.; Rutland, M. W.; Claesson, P. M. Hydration State of Nonionic Surfactant Monolayers at the Liquid/Vapor Interface: Structure Determination by Vibrational Sum Frequency Spectroscopy. *J. Am. Chem. Soc.* **2005**, *127* (48), 16848–16859.

(173) Michaelson, L. V.; Dunn, T. M.; Napier, J. A. Viral Trans-Dominant Manipulation of Algal Sphingolipids. *Trends Plant Sci.* **2010**, *15* (12), 651–655.

(174) Muralidhar, P.; Radhika, P.; Krishna, N.; Rao, D. V.; Rao, C. B. Sphingolipids from Marine Organisms: A Review. *Nat. Prod. Sci.* **2003**, *9* (3), 117–142.

(175) Conboy, J. C.; Messmer, M. C.; Richmond, G. L. Dependence of Alkyl Chain Conformation of Simple Ionic Surfactants on Head Group Functionality as Studied by Vibrational Sum-Frequency Spectroscopy. *J. Phys. Chem. B* **1997**, *101* (34), 6724–6733.

(176) Allhusen, J. S.; Kimball, D. R.; Conboy, J. C. Structural Origins of Cholesterol Accelerated Lipid Flip-Flop Studied by Sum-Frequency Vibrational Spectroscopy. *J. Phys. Chem. B* **2016**, *120* (12), 3157–3168.

(177) *International Critical Tables*, 1st ed.; Washburn, E. W., Ed.; McGraw-Hill Book Company: New York, NY, 1928; Vol. 4.

(178) Aumann, E.; Hildenmann, L. M.; Tabazadeh, A. Measuring and Modeling the Composition and Temperature-Dependence of Surface Tension for Organic Solutions. *Atmos. Environ.* **2010**, *44* (3), 329–337.

(179) Harkins, W. D.; McLaughlin, H. M. The Structure of Films of Water on Salt Solutions I. Surface Tension and Adsorption for Aqueous Solutions of Sodium Chloride. *J. Am. Chem. Soc.* **1925**, *47* (8), 2083–2089.

(180) Hua, W.; Verreault, D.; Allen, H. C. Surface Prevalence of Perchlorate Anions at the Air/Aqueous Interface. *J. Phys. Chem. Lett.* **2013**, *4* (24), 4231–4236.

(181) Hua, W.; Verreault, D.; Allen, H. C. Surface Electric Fields of Aqueous Solutions of NH_4NO_3, $Mg(NO_3)_2$, $NaNO_3$, and $LiNO_3$: Implications for Atmospheric Aerosol Chemistry. *J. Phys. Chem. C* **2014**, *118* (43), 24941–24949.

(182) Fu, L.; Liu, J.; Yan, E. C. Y. Chiral Sum Frequency Generation Spectroscopy for Characterizing Protein Secondary Structures at Interfaces. *J. Am. Chem. Soc.* **2011**, *133* (21), 8094–8097.

(183) Bach, D.; Sela, B.; Miller, I. R. Compositional Aspects of Lipid Hydration. *Chem. Phys. Lipids* **1982**, *31* (4), 381–394.

(184) Matsumoto, K.; Uematsu, M. Free Amino Acids in Marine Aerosols over the Western North Pacific. *Atmos. Environ.* **2005**, *39* (11), 2163–2170.

(185) Keene, W. C.; Sander, R.; Pszenny, A. A. P.; Vogt, R.; Crutzen, P. J.; Galloway, J. N. Aerosol pH in the Marine Boundary Layer: A Review and Model Evaluation. *J. Aerosol Sci.* **1998**, *29* (3), 339–356.

(186) Morris, H. S.; Grassian, V. H.; Tivanski, A. V. Humidity-Dependent Surface Tension Measurements of Individual Inorganic and Organic Submicrometre Liquid Particles. *Chem. Sci.* **2015**, *6* (5), 3242.

(187) Morris, H. S.; Estillore, A. D.; Laskina, O.; Grassian, V. H.; Tivanski, A. V. Quantifying the Hygroscopic Growth of Individual Submicrometer Particles with Atomic Force Microscopy. *Anal. Chem.* **2016**, *88* (7), 3647–3654.

(188) Seoane, R.; Miñones, J.; Conde, O.; Miñones, Jr., J.; Casas, M.; Iribarnegaray, E. Thermodynamic and Brewster Angle Microscopy Studies of Fatty Acid/Cholesterol Mixtures at the Air-Water Interface. *J. Phys. Chem. B* **2000**, *104* (32), 7735–7744.

(189) Sierra-Hernandez, M. R.; Allen, H. C. Incorporation and Exclusion of Long Chain Alkyl Halides in Fatty Acid Monolayers at the Air-Water Interface. *Langmuir* **2010**, *26* (24), 18806–18816.

(190) Prisle, N. L.; Ottosson, N.; Öhrwell, G.; Söderström, J.; Dal Masso, M.; Björneholm, O. Surface/Bulk Partitioning and Acid/Base Speciation of Aqueous Decanoate: Direct Observations and Atmospheric Implications. *Atmos. Chem. Phys.* **2012**, *12* (24), 12227–12242.

(191) Shih, M. C.; Bohanon, T. M.; Mikrut, J. M.; Zschack, P.; Dutta, P. Pressure and pH Dependence of the Structure of a Fatty Acid Monolayer with Calcium Ions in the Subphase. *J. Chem. Phys.* **1992**, *96* (2), 1556.

(192) Miranda, P. B.; Du, Q.; Shen, Y. R. Interaction of Water with a Fatty Acid Langmuir Film. *Chem. Phys. Lett.* **1998**, *286* (1–2), 1–8.

(193) Le Calvez, E.; Blaudez, D.; Buffeteau, T.; Desbat, B. Effect of Cations on the Dissociation of Arachidic Acid Monolayers on Water Studied by Polarization-Modulated Infrared Reflection-Absorption Spectroscopy. *Langmuir* **2001**, *17* (3), 670–674.

(194) Gilman, J. B.; Eliason, T. L.; Fast, A.; Vaida, V. Selectivity and Stability of Organic Films at the Air-Aqueous Interface. *J. Colloid Interface Sci.* **2004**, *280* (1), 234–243.

(195) Kundu, S.; Langevin, D. Fatty Acid Monolayer Dissociation and Collapse: Effect of pH and Cations. *Colloids Surf. Physiochemical Eng. Asp.* **2008**, *325*, 81–85.

(196) Kanicky, J. R.; Shah, D. O. Effect of Degree, Type, and Position of Unsaturation on the pKa of Long-Chain Fatty Acid. *J. Colloid Interface Sci.* **2002**, *256* (1), 201–207.

(197) Deo, A. V.; Kulkarni, S. B.; Gharpurey, M. K.; Biswas, A. B. Rate of Spreading and Equilibrium Spreading Pressure of the Monolayers of N-Fatty Alcohols and N-Alkoxy Ethanols. *J. Phys. Chem.* **1962**, *66* (7), 1361–1362.

(198) Phillips, M. C.; Hauser, H. Spreading of Solid Glycerides and Phospholipids at the Air-Water Interface. *J. Colloid Interface Sci.* **1974**, *49* (1), 31–39.

(199) Iwahashi, M.; Maehara, N.; Kaneko, Y.; Seimiya, T. Spreading Pressures for Fatty-Acid Crystals at the Air/Water Interface. *J. Chem. Soc. Faraday Trans.* **1985**, *81*, 973–981.

(200) Tsuji, M.; Nakahara, H.; Moroi, Y.; Shibata, O. Water Evaporation Rates across Hydrophobic Acid Monolayers at Equilibrium Spreading Pressure. *J. Colloid Interface Sci.* **2008**, *318* (2), 322–330.

(201) Gershfeld, N. L.; Tajima, K. Energetics of the Transition between Lecithin Monolayers and Bilayers. *J. Colloid Interface Sci.* **1977**, *59* (3), 597–604.

(202) Gaines, G. L., Jr. *Insoluble Monolayers at Liquid-Gas Interfaces*; Interscience Publishers: United States, 1966.

(203) Broniatowski, M.; Dynarowicz-Łątka, P.; Camacho, L.; Martin Romero, M. T.; Muñoz, E. Semifluorinated Thiols in Langmuir Monolayers. *J. Colloid Interface Sci.* **2010**, *346* (1), 153–162.

(204) Sims, B.; Zografi, G. Time-Dependent Behavior of Insoluble Monomolecular Films: Fatty Acids and Some Derivatives. *J. Colloid Interface Sci.* **1972**, *41* (1), 35–46.

(205) Cheek, B. J.; Steel, A. B.; Miller, C. J. Langmuir Monolayer Flow across Hydrophobic Surfaces. 2. Sensor Development Using Langmuir Monolayer Flow. *Langmuir* **2000**, *16* (26), 10334–10339.

(206) Snow, A. W.; Jernigan, G. G.; Ancona, M. G. Equilibrium Spreading Pressure and Langmuir-Blodgett Film Formation of Omega-Substituted Palmitic Acids. *Thin Solid Films* **2014**, *556*, 475–484.

(207) Donnison, J. A.; Heymann, E. The Equilibrium Spreading Pressure of Oleic Acid and of Ethyl Sebacate on Concentrated Salt Solutions. *Trans. Faraday Soc.* **1946**, *42* (1–2), 1–5.

(208) Knopf, D. A.; Forrester, S. M. Freezing of Water and Aqueous NaCl Droplets Coated by Organic Monolayers as a Function of Surfactant Properties and Water Activity. *J. Phys. Chem. A* **2011**, *115* (22), 5579–5591.

(209) Bunow, M. R.; Levin, I. W. Molecular Conformations of Cerebrosides in Bilayers Determined by Raman Spectroscopy. *Biophys. J.* **1980**, *32* (3), 1007–1022.

(210) Rybachuk, M.; Hu, A.; Bell, J.M. Resonant Raman Scattering from Polyacetylene and Poly(p -Phenylene Vinylene) Chains Induced into Hydrogenated Amorphous Carbon. *Appl. Phys. Lett.* **2008**, *93* (5), 51904.

(211) Lee, K. Y. C.; Majewski, J.; Kuhl, T. L.; Howes, P. B.; Kjaer, K.; Lipp, M. M.; Waring, A. J.; Zasadzinski, J. A.; Smith, G. S. Synchrotron X-Ray Study of Lung Surfactant-Specific Protein SP-B in Lipid Monolayers. *Biophys. J.* **2001**, *81* (1), 572–585.
(212) Lin, W.; Clark, A. J.; Paesani, F. Effects of Surface Pressure on the Properties of Langmuir Monolayers and Interfacial Water at the Air-Water Interface. *Langmuir* **2015**, *31* (7), 2147–2156.
(213) Nguyen, K. T.; Nguyen, A. V. In Situ Investigation of Halide Co-Ion Effects on SDS Adsorption at Air-Water Interfaces. *Soft Matter* **2014**, *10* (34), 6556.
(214) Davey, R. J.; Dent, G.; Mughal, R. K.; Parveen, S. Concerning the Relationship between Structural and Growth Synthons in Crystal Nucleation: Solution and Crystal Chemistry of Carboxylic Acids As Revealed through IR Spectroscopy. *Cryst. Growth Des.* **2006**, *6* (8), 1788–1796.
(215) Eichi Goto, T.; Caseli, L. Understanding the Collapse Mechanism in Langmuir Monolayers through Polarization Modulation-Infrared Reflection Absorption Spectroscopy. *Langmuir* **2013**, *29* (29), 9063–9071.
(216) Tarbuck, T. L.; Ota, S. T.; Richmond, G. L. Spectroscopic Studies of Solvated Hydrogen and Hydroxide Ions at Aqueous Surfaces. *J. Am. Chem. Soc.* **2006**, *128* (45), 14519–14527.
(217) Tian, C.; Ji, N.; Waychunas, G. A.; Shen, Y. R. Interfacial Structures of Acidic and Basic Aqueous Solutions. *J. Am. Chem. Soc.* **2008**, *130* (39), 13033–13039.
(218) Gopalakrishnan, S.; Liu, D.; Allen, H. C. Vibrational Spectroscopic Studies of Aqueous Interfaces: Salts, Acid, Bases, and Nanodrops. *Chem. Rev.* **2006**, *106* (4), 1155–1175.
(219) Wertz, P. W. Lipids and Barrier Function of the Skin. *Acta Derm. Venereol.* **2000**, *208*, 7–11.
(220) Madison, K. C. Barrier Function of the Skin: “La Raison d’Etre” of the Epidermis. *J. Invest. Dermatol.* **2003**, *121* (2), 231–241.
(221) Proksch, E.; Brandner, J. M.; Jensen, J. The Skin; an Indispensable Barrier. *Exp. Dermatol.* **2008**, *17* (12), 1063–1072.
(222) Menon, G. K.; Cleary, G. W.; Lane, M. E. The Structure and Function of the Stratum Corneum. *Int. J. Pharm.* **2012**, *435* (1), 3–9.
(223) Matoltsy, A. G.; Downes, A. M.; Sweeney, T. M. Studies of the Epidermal Water Barrier. Part II. Investigation of the Chemical Nature of the Water Barrier. *J. Invest. Dermatol.* **1968**, *50* (1), 19–26.
(224) Sweeney, T. M.; Downing, D. T. The Role of Lipids in the Epidermal Barrier to Water Diffusion. *J. Invest. Dermatol.* **1970**, *55* (2), 135–140.

(225) Wertz, P. W.; van den Bergh, B. The Physical, Chemical, and Functional Properties of Lipids in the Skin and Other Biological Barriers. *Chem. Phys. Lipids* **1998**, *91* (2), 85–96.

(226) Forslind, B. A Domain Mosaic Model of the Skin Barrier. *Acta Derm. Venereol.* **1994**, *74* (1), 1–6.

(227) Bouwstra, J. A.; Dubbelaar, F. E. R.; Gooris, G. S.; Ponec, M. The Lipid Organisation in the Skin Barrier. *Acta Derm. Venereol.* **2000**, *208*, 23–30.

(228) Elias, P. M.; Cooper, E. R.; Korc, A.; Brown, B. E. Percutaneous Transport in Relation to Stratum Corneum Structure and Lipid Composition. *J. Invest. Dermatol.* **1981**, *76* (4), 297–301.

(229) Gray, G. M.; Yardley, H. J. Lipid Composition of Cells Isolated from Pig, Human, and Rat Epidermis. *J. Lipid Res.* **1975**, *16* (6), 434–440.

(230) Holleran, W. M.; Takagi, Y.; Menon, G.K.; Legler, G.; Feingold, K.R.; Elias, P.M. Processing of Epidermal Glucosylceramides Is Required for Optimal Mammalian Cutaneous Permeability Barrier Function. *J. Clin. Invest.* **1993**, *91* (4), 1656–1664.

(231) Holleran, W. M.; Ginns, E. I.; Menon, G. K.; Grundmann, J.; Fartasch, M.; McKinney, C. E.; Elias, P. M.; Sidransky, E. Consequences of Beta-Glucocerebrosidase Deficiency in Epidermis. *J. Clin. Invest.* **1994**, *93* (4), 1756–1764.

(232) Fujimoto, A.; Tayebi, N.; Sidransky, E. Congenital Ichthyosis Preceding Neurologic Symptoms in Two Sibs With Type 2 Gaucher Disease. *Am. J. Med. Genet.* **1995**, *59* (3), 356–358.

(233) Tieleman, B. I.; Williams, J. B. Cutaneous and Respiratory Water Loss in Larks from Arid and Mesic Environments. *Physiol. Biochem. Zool.* **2002**, *75* (6), 67–75.

(234) Champagne, A. M.; Allen, H. C.; Williams, J. B. Lipid Composition and Molecular Interactions Change with Depth in the Avian Stratum Corneum to Regulate Cutaneous Water Loss. *J. Exp. Biol.* **2015**, *218* (19), 3032–3041.

(235) Champagne, A. M.; Allen, H. C.; Bautista-Jimenez, R. C.; Williams, J. B. Organization of Lipids in Avian Stratum Corneum: Changes with Temperature and Hydration. *Chem. Phys. Lipids* **2016**, *195*, 47–57.

(236) Maggio, B.; Cumar, F. A.; Caputto, R. Surface Behavior of Gangliosides and Related Glycosphingolipids. *Biochem. J.* **1978**, *171* (3), 559–565.

(237) Muñoz-Garcia, A.; Ro, J.; Brown, J. C.; Williams, J. B. Identification of Complex Mixtures of Sphingolipids in the Stratum Corneum by Reversed-Phase High-Performance Liquid Chromatography and Atmospheric Pressure Photospray Ionization Mass Spectrometry. *J. Chromatogr. A* **2006**, *1133* (1–2), 58–68.

(238) Ro, J.; Williams, J. B. Respiratory and Cutaneous Water Loss of Temperate-Zone Passerine Birds. *Comp. Biochem. Physiol. Part A* **2010**, *156* (2), 237–246.

(239) Cadena-Nava, R. D.; Martin-Mirones, J. M.; Vazquez-Martinez, E. A.; Roca, J. A.; Ruiz-Garcia, J. Direct Observations of Phase Changes in Langmuir Films of Cholesterol. *Rev. Mex. Física* **2006**, *52* (5), 32–40.

(240) Kaganer, V. M.; Möhwald, H.; Dutta, P. Structure and Phase Transitions in Langmuir Monolayers. *Rev. Mod. Phys.* **1999**, *71* (3), 779–819.

(241) Teixeira, A. C.; Brogueira, P.; Fernandes, A. C.; Gonçalves da Silva, A. M. P. S. Phase Behavior of Binary Mixtures Involving Tristearin, Stearyl Stearate and Stearic Acid: Thermodynamic Study and BAM Observation at the Air-Water Interface and AFM Analysis of LB Films. *Chem. Phys. Lipids* **2008**, *153* (2), 98–108.

(242) Rosetti, C. M.; Oliveira, R. G.; Maggio, B. Reflectance and Topography of Glycosphingolipid Monolayers at the Air-Water Interface. *Langmuir* **2003**, *19* (2), 377–384.

(243) Liu, D.; Ma, G.; Levering, L. M.; Allen, H. C. Vibrational Spectroscopy of Aqueous Sodium Halide Solutions and Air-Liquid Interfaces: Observation of Increased Interfacial Depth. *J. Phys. Chem. B* **2004**, *108* (7), 2252–2260.

(244) Chen, X.; Hua, W.; Huang, Z.; Allen, H. C. Interfacial Water Structure Associated with Phospholipid Membranes Studied by Phase-Sensitive Vibrational Sum Frequency Generation Spectroscopy. *J. Am. Chem. Soc.* **2010**, *132* (32), 11336–11342.

(245) Sung, W.; Seok, S.; Kim, D.; Shen, Y. R. Sum-Frequency Spectroscopic Study of Langmuir Monolayers of Lipids Having Oppositely Charged Headgroups. *Langmuir* **2010**, *26* (23), 18266–18272.

(246) Johnson, C. M.; Baldelli, S. Vibrational Sum Frequency Spectroscopy Studies of the Influence of Solutes and Phospholipids at Vapor/Water Interfaces Relevant to Biological and Environmental Systems. *Chem. Rev.* **2014**, *114* (17), 8416–8446.

Appendix A: BAM Data Processing

A.1. Camera Calibration

In order to obtain quantitative monolayer thickness or monolayer refractive index values, the CCD camera must be calibrated to relate the measured gray level to the intensity of the reflectance, $I = |R_p|^2$. To calibrate camera, collect an image of the bare aqueous surface at incident angles ± 0.5° from the Brewster angle in integrals of 0.1°. Record the gray level in the center of the image. The gray level can be taken as the counts displayed in the Andor Solis software, or determined from the BAM image in ImageJ software (as discussed below). When the gray level is plotted against the incident angle a parabolic shape should be observed, as shown in Figure A.1.

The gray level can be related to I, calculated from Eq. 2.3, by plotting the I vs. gray level for each individual incident angle, as shown in Figure A.2. A linear trend should be observed. After fitting the data with a linear function ($y = mx + b$), the measured grey level in BAM images can be converted to a reflectance value for that particular subphase. This process should be repeated for each subphase.

A.2. Grey Level Determination in ImageJ

Grey level on bare and monolayer-covered surfaces in this dissertation was determined with the software ImageJ. ImageJ is a free software program (https://imagej.nih.gov/ij/). In ImageJ, open a BAM image. The scale for the image should be set before any further processing is done. To set the scale go to the *Analyze* menu, and select *Set Scale* from the dropdown menu. Enter the distance in pixels, known distance, and unit of length. If several images are to be analyzed, click the global box, and the scale will be applied to all subsequent images opened. For the BAM setup described in this dissertation, the distance in pixels is 63, the known distance is 100, and units are µm. Images should be cropped to the most resolved region, and can be done by selecting *Crop* under the *Image* menu. If a scale bar is desired, add one by going to the *Analyze* menu, selecting *Tools*, and then selecting *Scale Bar*. Enter details of desired scale, etc. To obtain grey level, first draw a line across the whole image using the select tool, as shown in Figure A.3. Under *Analyze* menu select *Plot Profile*; the grey level for the pixels over which the line was drawn on the image will appear as a new window, as shown in Figure A.4. This new window may be saved as a text file. In studies done here, the gray level was obtained for three separate y-pixels, and then averaged. An overall grey level was determined for each image by averaging over all x-pixels to obtain a single value. This grey level value can then be converted to a reflectance value, as determined by the camera calibration.

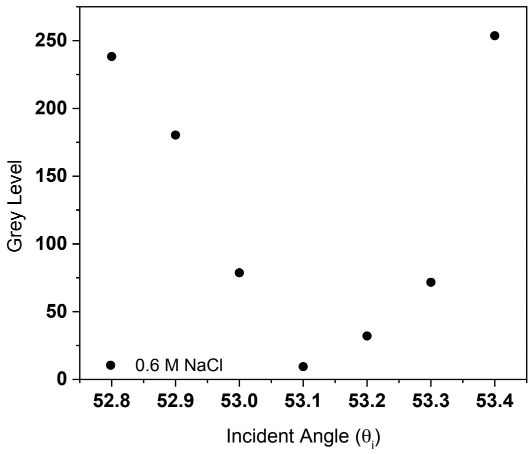

Figure A.1. Grey level of BAM image as a function of incident angle for a 0.6 M NaCl solution.

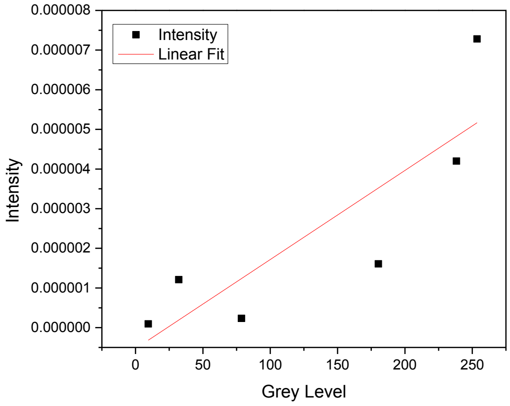

Figure A.2. Intensity of reflected *p*-polarized light calculated from Fresnel coefficients as a function of measured grey level for a 0.6 M NaCl solution.

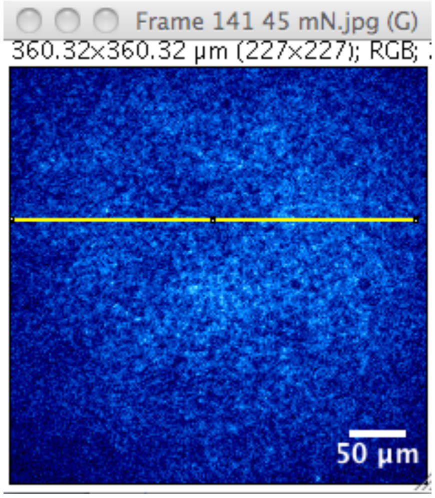

Figure A.3. Cropped BAM image, where a line has been drawn horizontally using the select tool.

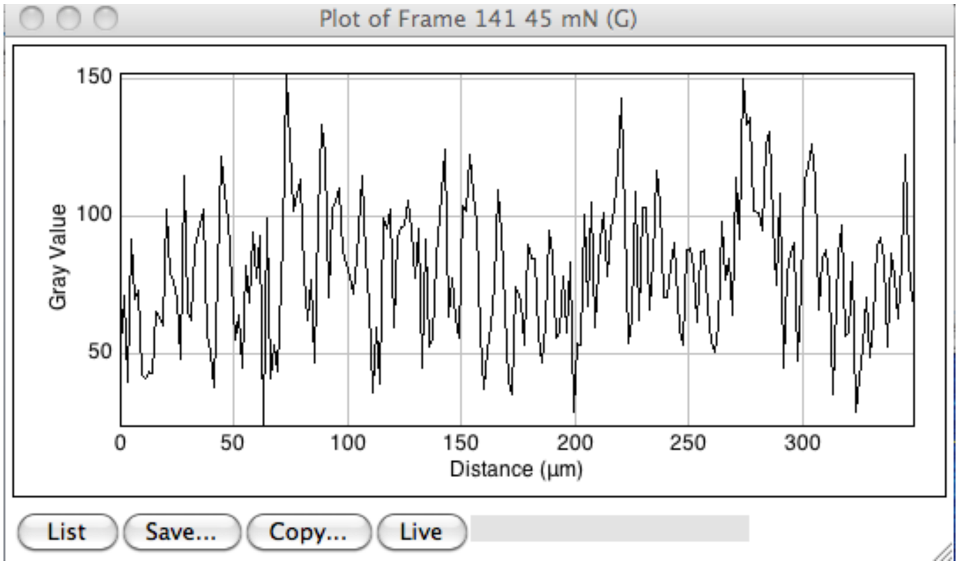

Figure A.4. Grey level of each x-pixel (in distance µm) over which the horizontal line was drawn in BAM image shown in Fig. A.3.

Appendix B: IRRAS Data Processing

Baseline correction of IRRAS spectra was done in OriginPro 9.0 (OriginLab). The spectrum was plotted in the region of interest and then processing was done. In the phosphate region, as shown in Figure B.1, the region of interest was restricted to 1300-900 cm^{-1}. In other regions the spectrum was limited to: for CH region, 3000-2800 cm^{-1}; for C=O, 1800-1550 cm^{-1}; for $\delta(CH_2)$, 1500-1400 cm^{-1}; and for $\delta(CH_2)$, 1100-1000 cm^{-1}. To do the baseline correction, the absorbance peaks in the original spectrum were deleted from the spectrum, as shown in Figure B.2. The remaining points in the spectrum were fit with a third order polynomial, as shown in Figure B.3. The fitted polynomial is considered the baseline, and was subtracted from the original spectrum to obtain the baseline corrected spectrum, as shown in Figure B.4. Several baseline-corrected spectra (a minimum of two) were averaged to obtain a final spectrum.

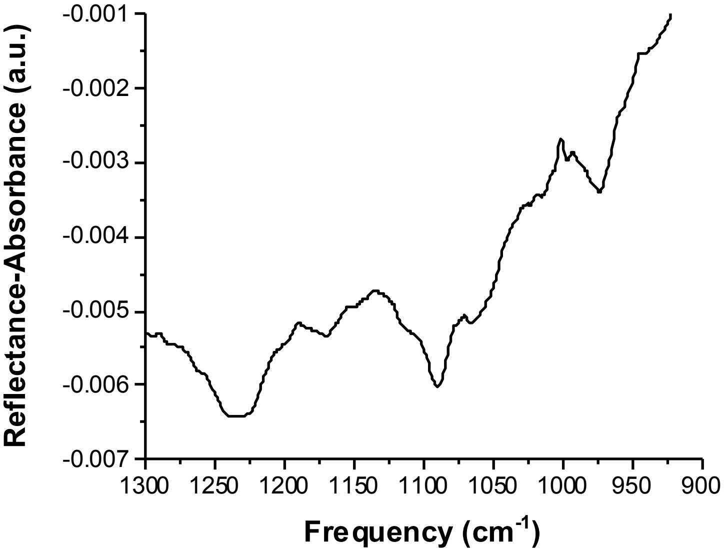

Figure B.1. Original IRRAS spectrum of DPPC on water in the phosphate region (1300-900 cm^{-1}) prior to any processing.

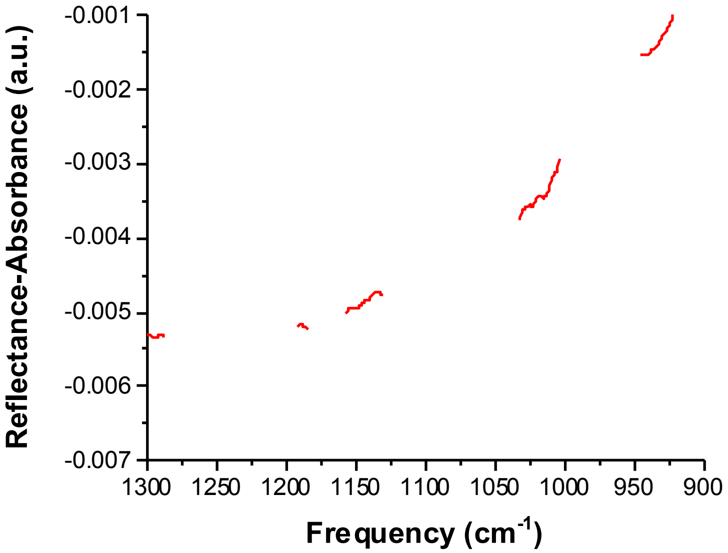

Figure B.2. Spectrum from Fig. B.1 after absorbance peaks are deleted from the spectrum.

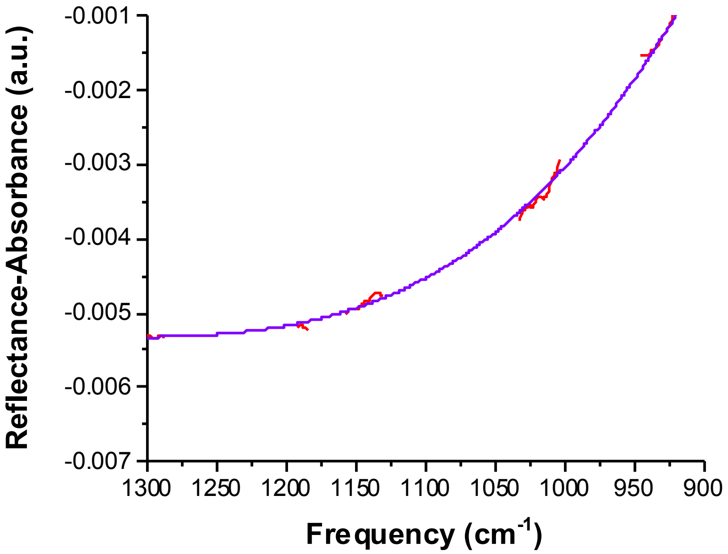

Figure B.3. Third-order polynomial fit of spectrum shown in Fig. B.2.

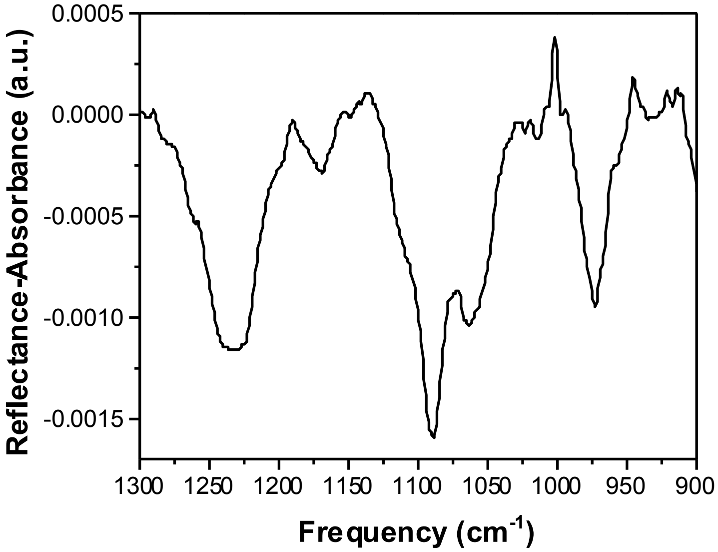

Figure B.4. Baseline-corrected IRRAS spectrum after third-order polynomial fitted function is subtracted from the original spectrum in Fig. B.1.

Appendix C: VSFG Data Collection and Processing

C.1. Data Collection

The time of acquisition depends on the region of interest. In regions of interest in which an intense signal could be obtained in a short acquisition time, the cosmic correction function was selected in the SpectraSense (Version 5.0) software. The selection of this function doubles the integration time. For example, when 60 seconds is input as the integration time, the total spectrum actually takes 120 seconds. For long acquisition times, the spectrum was cosmic corrected after collection, which is discussed in more detail below. The following integration times were used in various regions: OH & free OH region (3000-3700 cm^{-1}), 5 min; CH region (2800-3000 cm^{-1}), 60 s with cosmic correct function (120 s total); CD region (2000-2300 cm^{-1}), 60 s with cosmic correct function (120 s total), C=O region (1750-1600 cm^{-1}), 5 min; COO^{-} region (1500-1350 cm^{-1}), 5 min; phosphate region (1150-1000 cm^{-1}), 5 min.

When long acquisition times were used (i.e. 5 min without cosmic correct function), vertical binning of pixels was done to reduce cosmic radiation spikes. Horizontal binning cannot be done in the SpectraSense software. Prior to collection of the spectrum, an image of the SFG signal on the CCD chip was taken for a period of 60 seconds (lipid-covered surfaces) or 120 seconds (bare surfaces) to determine its vertical position. A binning region of 20-30 pixels on either side of the center of the SFG signal was then selected, as is shown in Figure C.1.

C.2. Data Processing

As discussed in Chapter 2, VSFG spectra were processed by filtration of cosmic radiation. Removal of cosmic radiation spikes was typically only done for spectra with long integration times, as the cosmic correct function sufficiently removes spikes for short integration times. Cosmic spikes are removed from spectra by doing a 3-point smooth around the spike (Note: a 3-point smooth is not applied to whole spectrum, just the x-axis value(s) at which the cosmic radiation spike occurs). Removal of cosmic radiation should not significantly impact shape of spectrum, as shown in Figure C.2.

After removal of cosmic radiation from the spectra, two VSFG spectra were averaged. The background spectrum is then subtracted from the averaged spectrum. A background spectrum is collected for the same period of time, and is achieved by moving the visible beam delay stage such that both the visible and IR impinge the surface, but SFG is not produced due to lack of temporal overlap. Negative values resulting from the background subtraction should be corrected to 0. After background subtraction, the spectrum is normalized to the non-resonant spectrum of GaAs (in the same polarization combination). A GaAs spectrum is collected for 1 s, independent of the spectral region. The normalized spectrum is the final spectrum

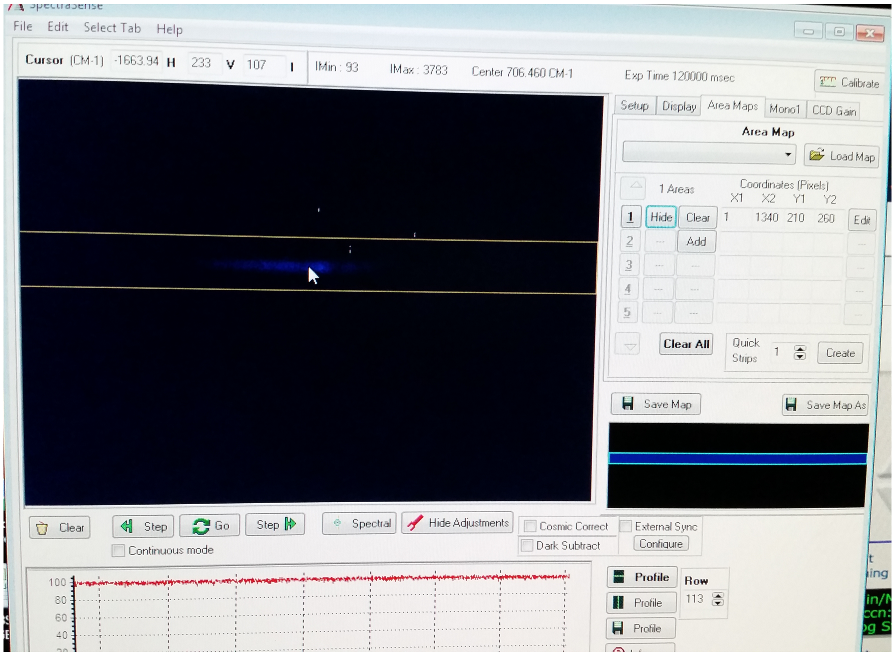

Cursor (CM-1) -1663.94 H 233 V 107 I

IMin : 93 IMax : 3783 Center 706.460 CM-1

Exp Time 120000 msec

1 Areas	X1	X2	Y1	Y2
1	1	1340	210	260

Quick Strips 1

Row 113

Figure C.1. Image of SFG signal (in blue, left image) on the CCD chip. The binned region is designated by the yellow lines.

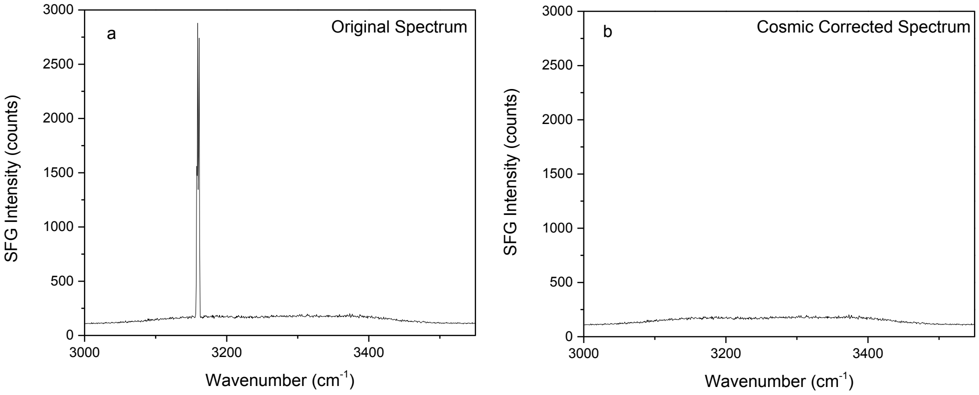

Figure C.2. (a) Raw, original VSFG spectrum of air-water interface in the OH region (3000-3600 cm^{-1}) and (b) same spectrum after cosmic radiation is removed.

Appendix D: Permissions

Chapter 3: Reproduced in part with permission from Adams, E.M.; Casper, C.B.; Allen, H.C. "Effect of Cation Enrichment on Dipalmitoylphosphatidylcholine (DPPC) Monolayers at the Air-Water Interface" *J. Colloid Interface Sci.*, **2016**, 478, 353-364. Copyright Elsevier

- Rightslink user agreement license is provided below

ELSEVIER LICENSE
TERMS AND CONDITIONS

Oct 17, 2016

This Agreement between Ellen M Adams ("You") and Elsevier ("Elsevier") consists of your license details and the terms and conditions provided by Elsevier and Copyright Clearance Center.

License Number	3971630109083
License date	Oct 17, 2016
Licensed Content Publisher	Elsevier
Licensed Content Publication	Journal of Colloid and Interface Science
Licensed Content Title	Effect of cation enrichment on dipalmitoylphosphatidylcholine (DPPC) monolayers at the air-water interface
Licensed Content Author	Ellen M. Adams,Clayton B. Casper,Heather C. Allen
Licensed Content Date	15 September 2016
Licensed Content Volume Number	478
Licensed Content Issue Number	n/a
Licensed Content Pages	12
Start Page	353
End Page	364
Type of Use	reuse in a thesis/dissertation
Portion	full article
Format	both print and electronic
Are you the author of this Elsevier article?	Yes
Will you be translating?	No
Order reference number	
Title of your thesis/dissertation	Spectroscopic Studies of Atmospheric and Biological Relevant Interfaces: Lipids, Ions, and Interfacial Water Structure
Expected completion date	Nov 2016

Chapter 4: Reproduced in part with permission from Adams, E.M.; Verreault, D.; Jayarathne, T.; Cocharn, R.E.; Stone, E.A.; Allen, H.C. “Surface Organization of a DPPC Monolayer on Concentrated $SrCl_2$ and $ZnCl_2$ Solutions” *Phys. Chem. Chem. Phys*., **2016**, 18, 32345-32357. Copyright PCCP Owner Societies